DOCTORAL DISSERTATION

Ionization mechanism and ISM properties of the NLR in low-z and high-z AGNs

KOKI TERAO

GRADUATE SCHOOL OF SCIENCE AND ENGINEERING
EHIME UNIVERSITY

2018

ABSTRACT

Galaxy evolution is one of the most discussed topics in contemporary astronomy. The process, however, is yet to be fully understood due to the complex mechanisms involved. Physical and chemical properties of the interstellar medium (ISM) in galaxies and their redshift evolution are important to understand the formation and evolution of galaxies. The emission-line diagnostics is a powerful tool to investigate these properties. Active galactic nuclei (AGNs) are one of the most luminous populations in the Universe. Their host galaxies are mainly massive galaxies and have an active supermassive black hole (SMBH) powered by mass accretion at the center. In particular, spectroscopic properties of narrow-line regions (NLRs) in AGNs have been often investigated because NLR gas clouds distribute at $\sim$ kpc scale that is comparable to the spatial scale of host galaxies. Since NLR clouds are mostly ionized through the photoionization process, ISM properties of host galaxies can be studied through detailed comparisons between photoionization models and emission-line spectra of NLRs.

AGNs are also known to play an important role in the evolution of their host galaxies, which is so-called "AGN feedback". The AGN feedback is a negative/positive feedback effect on the star-formation activity in AGN host galaxies. Understanding the feedback process caused by AGNs is one of the most key issues to reveal the co-evolution of galaxies and SMBHs in addition to formation of massive galaxies.

Though the importance of the AGN feedback in the evolution of AGN host galaxies is widely recognized, its physical mechanism (i.e., how the AGN activity transmits its energy to the ISM) is still unclear. Clarifying the physical mechanism of its energy transmission (from the AGN to its surrounding ISM) is central to understand the feedback process. In Chapter 2, we here aim to disentangle the ionization mechanisms by the AGN – photoionization versus shock ionization, and to investigate the origin of the shock. It is widely believed that the dominant ionization mechanism of NLRs in AGNs is the photoionization by ionizing photons from the central engine. Recent careful observational and theoretical researches, however, gradually revealed the contribution of the fast shock as well as the photoionization, both as an ionization source of gas in NLRs. Such fast shocks in NLRs are possibly related to the AGN feedback and therefore it is interesting to explore whether and how the fast shock contributes the NLR ionization in AGNs. To observationally discriminate the ionization mechanism of gas clouds in NLRs, the flux ratio of two forbidden emission lines seen in J-band, [Fe II]1.257μm/[P II]1.188μm, is useful. The flux ratio of [Fe II]/[P II] in shock-excited regions is expected to be high (> 20), while that in purely photoionized clouds should be low

(<2). We report our near-infrared spectroscopic observations of 26 nearby Seyfert galaxies with a near-infrared spectrograph (ISLE) boarded on the 188 cm telescope at Okayama Astrophysical Observatory. As a result, we measured the [Fe II]/[P II] flux ratio or its lower limit for 19 objects and also collected the flux ratio for 22 Seyfert galaxies from the literature. Based on the collected data, we found that the NLRs are photoionized in most cases, but the fast shock contributes significantly in some Seyfert galaxies. The measured [Fe II]/[P II] flux ratio shows no correlation with the radio loudness of the Seyfert galaxies in our sample, indicating that the radio jet is not the main origin of fast shocks in NLRs of Seyfert galaxies. A possible candidate of the origin of fast shocks in NLRs is an AGN-driven outflow that is recognized as blueshifted and/or broad (FWHM > 1000 km s^{-1}) forbidden emission lines observed in low/high z AGNs. This outflow likely spreads out to $\sim$1 kpc from the central AGN, given that the shocks in NLRs originates from such outflow. This work has been published in Terao et al. (2016).

The ISM properties of massive galaxies at $z > 2$ are particularly interesting, because it is sometimes claimed that the evolution of massive galaxies had already been completed at such high redshift. From statistical studies, metallicity of these galaxies are close to the values of local galaxies (thus close to the solar metallicity), and no redshift evolution is seen from $z \sim 2$ to present. This means that massive galaxies had been mainly formed at $z > 2$. However, normal massive galaxies at $z > 2$ are too faint to be examined in detail. On the other hand, emission-line spectra of NLRs in AGNs offer an alternative approach to investigate the ISM properties of high-z massive galaxies. In Chapter 3, we present the rest-UV spectra of three radio galaxies at $z \sim 3$ observed with VLT/FORS2 to measure the flux of several emission lines including relatively faint ones such as N IV]λ1486, O III]λ1663, and [Ne IV]λ2424. In addition, we collect UV-emission line fluxes of 12 high-z radio galaxies (HzRGs) from the literature. We diagnose the physical and chemical properties of the ISM for each object through the comparison between the measured emission-line fluxes and detailed photoionization models. We confirm that the metallicity of NLRs in AGNs at $z \sim 3$ is close to or higher than the solar metallicity, without assuming the gas density and ionization parameter thanks to the newly detected faint emission lines. This result suggests that HzRGs have already chemically matured by $z \sim 3$, that corresponds to the cosmic age of only ~ 2 Gyr.

In this thesis, we investigate the formation and evolution of galaxies by focusing on emission lines from NLRs in AGNs. From Chapter 2, we find that more than half of Seyfert galaxies in our sample show consistent [Fe II]/[P II] flux ratio with the prediction by the photoionization model ($\sim$2). Three Seyfert galaxies, NGC 2782, NGC 5005, and Mrk 463, however, show very large [Fe II]/[P II] flux ratios ($\gtrsim$10), suggesting a significant contribution of the fast shock in the NLR excitation. The [Fe II]/[P II] flux ratio in our sample shows no clear correlation with the radio loudness or the strength of the starburst, suggesting that the radio jet and starburst are not the primary origins of the fast shocks in the NLR. These results infer that the shock heating associated with the AGN outflow can be an important mechanism to affect the surrounding ISM during the AGN feedback. From Chapter 3, we confirmed that HzRGs had been chemically matured by $z \sim 3$, by using the photoionization models with much smaller assumption comparing for previous works thanks to many emission lines. This result indicates that the

epoch of formation such massive galaxies are mainly at $z \geq 4$. The inferred gas density and ionization parameter of NLRs tend to be higher than those seen in NLRs of low-z type 2 AGNs. This suggests that the properties of the ISM in NLRs possibly evolve with redshift.

CONTENTS

CHAPTER 1

INTRODUCTION

1.1 The formation and evolution of galaxies

Formation and evolution of galaxies are key to understand the total evolutionary picture of the Universe to date. However, the exact physical process of the formation and evolution of galaxies is not fully understood, due to their complex mechanisms. The gravitational framework of the Universe is often theoretically described with the Λ cold dark matter (CDM) model, followed by many observational and theoretical researches. Recent studies using modern advanced facilities gradually reveal the formation and evolution of galaxies from the very early epoch of the Universe to present. Observationally, various wide-field surveys on the celestial sphere with a high sensitivity have been carried out using state-of-the-art instruments on many telescopes at multi-wavelength. Many faint galaxies at high-z Universe and highest-z objects were discovered and investigated (e.g., Bouwens et al., 2015; Oesch et al., 2016, 2018; Bañados et al., 2018; Matsuoka et al., 2018b; Ishigaki et al., 2018). Theoretically, large-volume simulations for cosmology and N-body simulations with a huge number of particles for zoomed in galaxy formation had been done thanks to the improvement of model methodologies and the computing speed (e.g., Somerville & Davé, 2015; Naab & Ostriker, 2017). These studies altogether revealed the galaxy evolutionary process from the viewpoint of star formation (Section 1.1.1), chemical evolution (Section 1.1.2) and the coevolution of galaxies and supermassive black holes (SMBHs; Section 1.1.3). Here is a summary of a known scenario of the galaxy evolution together with the SMBH growth.

1.1.1 Star formation in galaxies

Observations of galaxies toward higher redshift have shed some light into the galaxy evolutionary process in terms of fundamental galaxy properties. The galaxy star formation rate density (SFRD) history in the Universe (e.g., Madau & Dickinson, 2014; Bouwens et al., 2015; Robertson et al., 2015), one of the main realizations in these few decades, is shown in Figure 1.1. Accordingly, it is now recognized that the peak of the star formation activity in the Universe is $z \sim$

2–3. In this "cosmic noon", the SFRD is ~ 10 times higher than at present. The star-formation sequence of galaxies can be analyzed with the relation between stellar mass M_* and star formation rate (SFR; Figure 1.2). The SFR of normal star-forming galaxies shows a tight linear relation with stellar mass M_*. This relation is so-called "star formation main sequence", which is confirmed to exist for galaxies within a wide redshift range of $0 < z < 4$ (e.g., Brinchmann et al., 2004; Daddi et al., 2007; Elbaz et al., 2007; Noeske et al., 2007; Pannella et al., 2009; Karim et al., 2011; Steinhardt et al., 2014; Tomczak et al., 2016). Galaxies scattered upwards with respect to the main sequence are called starbursts, and they show enhanced SFRs possibly due to galaxy mergers. The main sequence is known to evolve with time (e.g., Daddi et al., 2007; Speagle et al., 2014; Tomczak et al., 2016), suggesting a time evolution of SFR in each galaxy. Quiescent (non star-forming) galaxies occupy a region well below from that sequence (e.g., Leslie et al., 2016).

While the SFR evolves with time, other physical parameters of galaxies seem to develop together. The SMBH accretion-rate density, for example, shows a similar time evolution as the SFRD (Figure 1.3; Heckman & Best 2014). Here, the SMBH accretion-rate density is estimated by integrating a SMBH mass growth rate as shown by Equation (4) in Shankar et al. (2009), towards the faint-end cut of the 2–10 keV AGN luminosity function as given by their Equation (5). This indicates a synchronized growth of SMBHs and galaxies, that supports an idea of the so-called "coevolution of galaxies and SMBHs" (see Section 1.1.3 for details).

1.1.2 Chemical evolution of galaxies

Physical and chemical properties of the interstellar medium (ISM) such as gas density, ionization parameter, and gas metallicity are fundamental parameters for characterizing galaxies. These properties have been investigated by emission-line diagnostics (Osterbrock & Ferland, 2006). Flux ratios of different emission lines showing different ionization potentials and critical densities allow one to investigate the ISM properties and types of the incident continuum (e.g., Baldwin et al., 1981; Kewley et al., 2006; Osterbrock & Ferland, 2006).

Gas-phase metallicity of the ISM is known to be a good indicator of the galaxy evolutionary phase. Metal[1] is produced by nucleosynthesis in stars and provided into the ISM of galaxies by supernovae. The ISM metallicity hence represents the star formation history of each galaxy. The gas-phase metallicity in star-forming galaxies is commonly measured by using optical emission-line ratios (e.g., Alloin et al., 1979; Pagel et al., 1979; Kewley & Dopita, 2002; Nagao et al., 2006a; Maiolino et al., 2008; Curti et al., 2017). For example, the R_{23} parameter, defined as $R_{23} = [([\mathrm{O\ II}]\lambda 3727 + [\mathrm{O\ III}]\lambda\lambda 4959,5007)/\mathrm{H}\beta]$, has been widely used in the literature. However, there is a drawback in this indicator, in the sense that this ratio shows the same value at low and high metallicity. Some other emission-line ratios, such as $[\mathrm{N\ II}]\lambda 6584/\mathrm{H}\alpha$, $[\mathrm{O\ III}]\lambda 5007/[\mathrm{N\ II}]\lambda 6584$, and $[\mathrm{Ne\ III}]\lambda 3870/[\mathrm{O\ II}]\lambda 3727$, have been thus used for resolving that degeneracy and to determine the reliable metallicity of the ISM.

[1] In astronomy, the elements heavier than hydrogen and helium are classified as metals.

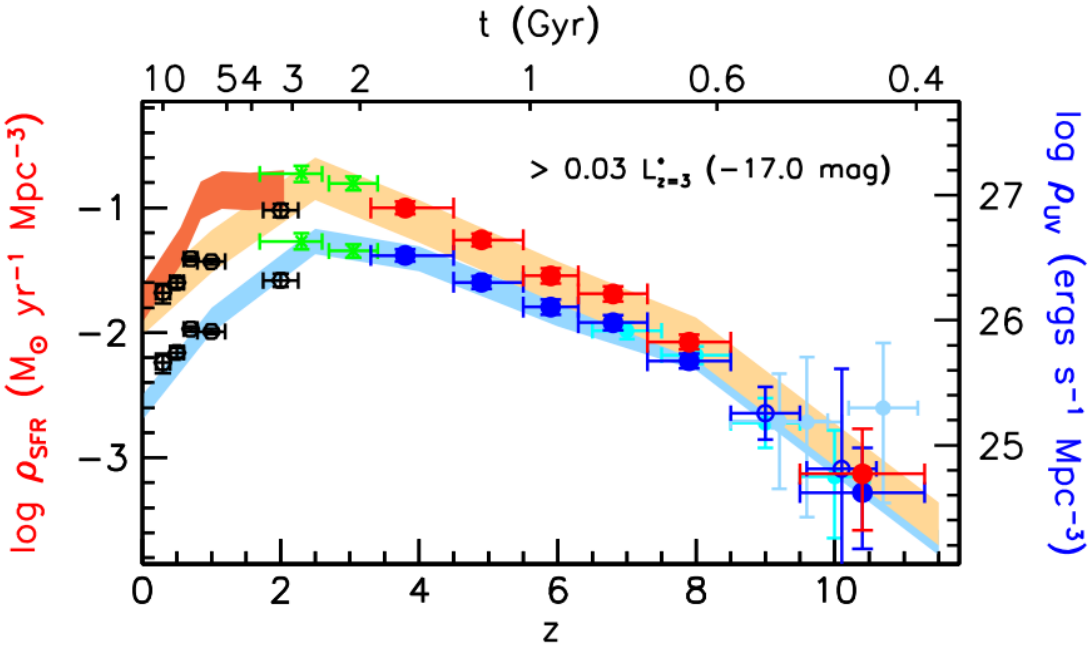

Fig. 1.1: The SFR (left axis) and UV luminosity densities (right axis) versus redshift (Bouwens et al., 2015). The SFR densities are inferred from the measured luminosity densities, assuming the Madau et al. (1998) conversion factor relevant for star-forming galaxies with ages of $\gtrsim 10^8$ yr (see also Kennicutt 1998). The right axis gives the UV luminosity density that is inferred by integrating the galaxy luminosity function to a faint-end limit of -17 mag ($0.03\ L^*_{z=3}$). The points and shaded regions show the SFR and UV luminosity densities corrected (upper set; includes red circles) and uncorrected (lower set; includes blue circles) for the effects of dust extinction. Other SFR densities are taken from Schiminovich et al. (2005, black hexagons), Reddy & Steidel (2009, green crosses), (Ellis et al., 2013; McLure et al., 2013, cyan circles), (Zheng et al., 2012; Coe et al., 2013; Bouwens et al., 2014, light blue circles), and Oesch et al. (2013, 2014, blue open circles). The dark red shaded region denotes the likely contribution for the SFR densities from IR bright sources at $z \sim 0.5$–2 (Daddi et al., 2009; Magnelli et al., 2009, 2011).

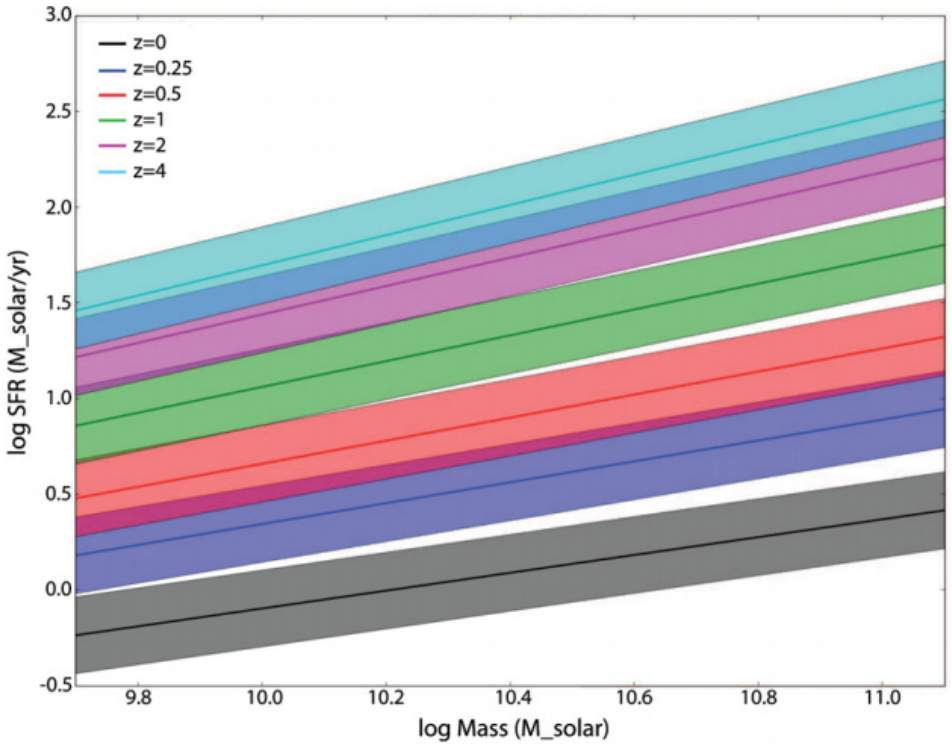

Fig. 1.2: Main-sequence (MS) relations at each redshift taken from the best fit to observations (Speagle et al., 2014). The MS slope and magnitude evolution in SFR ($\sim$ 2 orders) at fixed mass from $z = 4$ to 0 are easily visible.

The gas-phase metallicity is strongly coupled with the stellar mass of galaxies. This relation is so-called "mass-metallicity relation". Figure 1.4 shows the relation at the local Universe (Tremonti et al., 2004). Massive galaxies tend to show high metallicity, which can be simply explained by that many massive stars (i.e., short lifetime) were formed in such galaxies and then the ISM were chemically matured by supernovae. This relation is known to be established in the high-z Universe, at least $z \sim 3$ (e.g., Maiolino et al., 2008; Mannucci et al., 2009).

The completion time of the galaxy formation and star formation can be estimated by understanding the completing epoch of the metal enrichment in galaxies. In particular, it has been reported that the metallicity of massive galaxies is already high in high-z Universe (e.g., Maiolino et al., 2008; Troncoso et al., 2014). Hence investigations of the metallicity in such massive galaxies at high-z are very interesting. Unfortunately, the rest-frame optical emission lines are shifted out of the near-infrared atmospheric window, and thus observations towards $z \geq 3$ objects are more challenging than local galaxies. An alternative target to investigate metallicity of galaxies is active galactic nuclei (AGNs; see Section 1.2 for details). AGNs are emitting various emission lines in rest-UV wavelength, and thus emission-line spectra of AGNs at $z \leq 4$ can be examined at observed-frame optical. In previous studies, however, emission-line diagnostics required strong assumptions on some ISM parameters. For better accuracy,

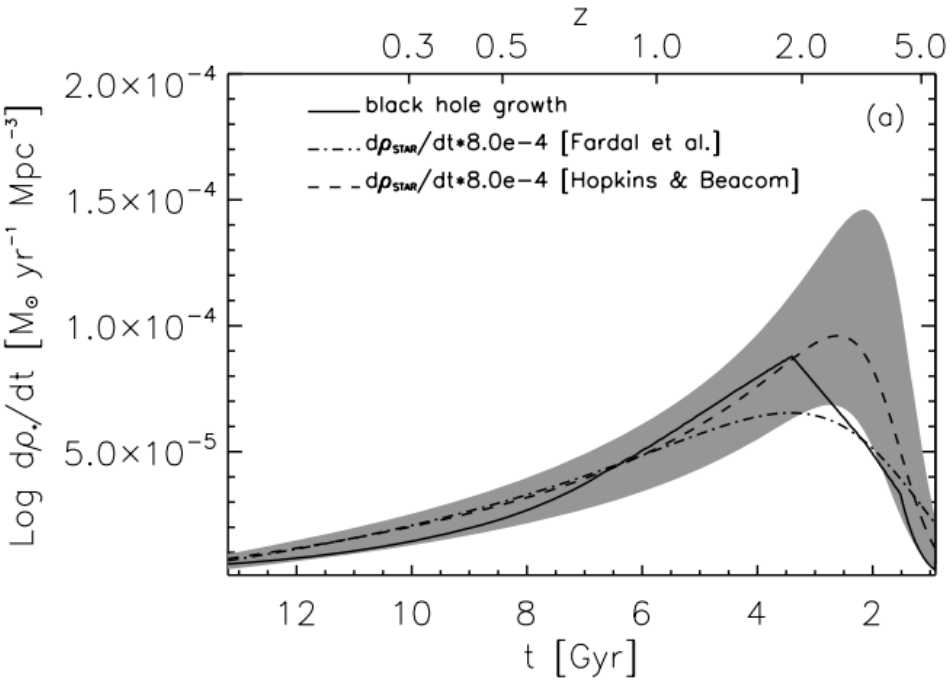

Fig. 1.3: The black hole growth and stellar mass growth as a function of redshift (Shankar et al., 2009). Solid line denotes the average black hole accretion rate, while dashed line and dot-dashed line are the star-formation rate as a function of redshift given by Hopkins & Beacom (2006) and Fardal et al. (2007). These parameters were scaled by the factor $M_{\rm BH}/M_{\rm STAR} = 0.8 \times 10^{-3}$. The shaded gray area shows the 3σ uncertainty region from Hopkins & Beacom (2006).

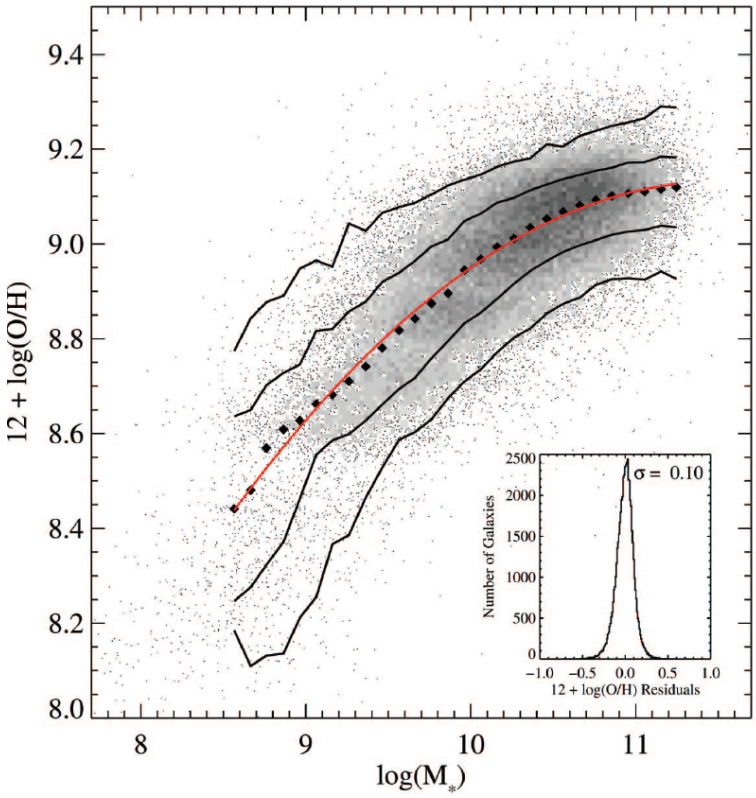

Fig. 1.4: Relation between stellar mass and gas-phase metallicity represented by oxygen abundance ratio (12+log(O/H)) for $\sim$ 53400 star-forming galaxies in the Sloan Digital Sky Survey (SDSS; Tremonti et al. 2004). The black diamonds denote the median in bins of 0.1 dex in mass that include at least 100 data points. The solid lines are the contours that enclose 68% and 95% of the data. The red line denotes a polynomial fit to the data. The inset figure shows the residuals of the fit.

it is important to do such diagnostics without assumptions with deeper observations and thus fainter emission lines (see Chapter 3 for details).

1.1.3 Coevolution of galaxy and supermassive black hole (SMBH)

In the context of the galaxy formation and evolution, a key result of these two decades was the realization that SMBHs ($M_{\rm BH} = 10^{6-10} M_{\odot}$) exist at nuclei in most stellar spheroids. Many observational studies confirmed that the mass of SMBHs correlates with some properties of the host galaxies such as stellar mass, luminosity, and stellar velocity dispersion of bulge components (e.g., Kormendy & Richstone, 1995; Magorrian et al., 1998; Ferrarese & Merritt, 2000; Marconi & Hunt, 2003; Gültekin et al., 2009; Kormendy & Ho, 2013; McConnell & Ma, 2013; Woo et al., 2013). Figure 1.5 shows a relation between the mass of SMBH and stellar mass of bulge component (Marconi & Hunt, 2003). These tight relations infer that the SMBH growth and the evolution of galaxies are closely linked. This idea of the coevolution is now commonly accepted in the related field. Although the details of the process remain unknown, a self-regulating process including AGN feedback is known to be necessary through many studies, such as current semi-analytic models and numerical simulations (Di Matteo et al., 2005; Croton et al., 2006; King & Pounds, 2015). The details of the AGN feedback are described in Section 1.2.5.

1.2 Active galactic nuclei

AGN is one of the most luminous objects in the Universe, and radiates vast energy in a broad wavelength (up to $L_{\rm bol} \approx 10^{48}$ erg s^{-1}). This energy is thought to be powered by the accretion of material onto a SMBH in the central part of a galaxy (Salpeter, 1964; Lynden-Bell, 1969). The first discovery of AGNs was reported by Seyfert (1943), who detected some broad and strong emission lines from nuclei of some nearby spiral galaxies. Such galaxies are nowadays called Seyfert galaxies. Seyfert galaxies are populated in the local Universe, and a large number of the local AGNs are classified as Seyferts (e.g., Ho, 2008). On the other hand, distant objects with similar properties but with a much higher luminosity, so-called quasars, were first discovered by Schmidt (1963). The quasar is the most luminous class among various populations of AGNs and mostly discovered at distant Universe.

There are many types of AGNs in the Universe, and those are mainly classified based on their luminosity, spectral features, and radio properties. Low-ionization nuclear emission-line regions (LINERs) are also classified into AGNs. LINERs are characterized by the presence of strong low-ionization emission lines such as [O I] (Heckman, 1980; Ho, 2008), though the origin of LINERs is still under debate (e.g., Maoz et al., 1998; Flohic et al., 2006; Molina et al., 2018). AGNs associated with a powerful radio source ($L_{1.4\rm GHz} > 10^{24}$ W Hz^{-1}) are classified as radio galaxies (Tadhunter, 2016). These various populations of AGNs show systematically different observational properties, but the physical mechanism to release their radiative energy

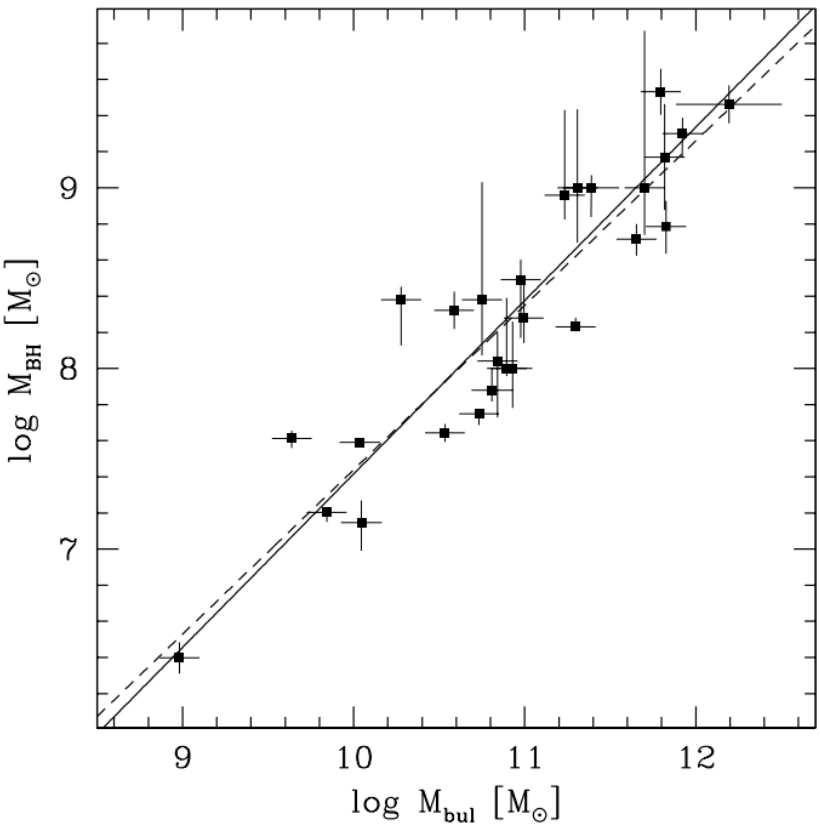

Fig. 1.5: The relation between mass of SMBHs ($M_{\rm BH}$) and stellar mass of bulges ($M_{\rm bul}$) (Marconi & Hunt, 2003). The solid lines are obtained with the bisector linear regression algorithm of Akritas & Bershady (1996), while the dashed lines are ordinary least-squares fits.

is thought to be essentially the same, i.e., the mass accretion onto SMBHs.

The triggering mechanism of luminous AGNs is thought to be gas-rich major mergers (e.g., Hopkins et al., 2008), because merger-induced turbulence helps bringing the gas towards the SMBH vicinity. On the other hand, low-luminous AGNs are possibly triggered by minor mergers or continual gas accretion from the host galaxies and surrounding halo (Hickox & Alexander, 2018).

The huge radiative energy released in various populations of AGNs is powered by the mass accretion onto SMBHs (Section 1.2.1). It is widely believed that the variety of the AGN population is caused partly by the axisymmetric structure around SMBHs. This picture, so-called "unified model", was proposed to explain various observational properties of AGNs (Section 1.2.2). From the ionized gas heated by the radiation from AGNs, numerous emission lines are detected in their spectra. These emission lines are typically divided into two groups, such as broad and narrow emission lines. The emitting region of narrow emission lines is so-called narrow-line region (NLR; Section 1.2.3). Those numerous emission lines can be utilized to investigate chemical properties and evolution of the ISM in host galaxies (Section 1.2.4). As shortly mentioned in Section 1.1.3, AGNs are thought to cause the feedback effect to the star-formation activity in their host galaxies, that is so-called "AGN feedback" (Section 1.2.5).

1.2.1 SMBH paradigm

AGNs are outstandingly luminous, and they sometimes outshine all the stars in their host galaxy. Such a vast amount of radiative energy is likely converted from the material accreting onto a SMBH, releasing its potential energy (Salpeter, 1964; Lynden-Bell, 1969). The accretion rate ($\dot{M} = dM/dt$) onto the SMBH is thus a key parameter to characterize the AGNs. The maximum achievable luminosity, so-called the Eddington luminosity ($L_{\rm Edd}$), is defined by a balance between the outward radiative force and the inward gravitational force. The Eddington luminosity is thus calculated by $L_{\rm Edd} = \frac{4\pi G M m_{\rm p} c}{\sigma_{\rm T}}$, where G is the gravitational constant, M is the mass of a SMBH, $m_{\rm p}$ is the proton mass, c is the speed of light, and $\sigma_{\rm T}$ is the Thomson scattering cross-section of an electron (Sparke & Gallagher, 2006). When the bolometric luminosity of an AGN ($L_{\rm bol}$) is available, one can estimate its central SMBH mass $M_{\rm BH}$ by assuming the Eddington-limit accretion (i.e., the outward radiative force and the inward gravitational force is balancing). On the other hand, in the case that the SMBH mass $M_{\rm BH}$ is known, one can define the ratio of the bolometric luminosity and the Eddington luminosity. This ratio is called Eddington ratio, which is also an important character to describe the properties of AGNs. The luminosity of AGNs can be written as $L = \eta \dot{M} c^2$, where $\dot{M}$ is the mass accretion rate, η is the energy conversion efficiency from the mass accretion to radiation, and c is the speed of light. Then the accretion rate is written as $\dot{M} = L/(\eta c^2)$. Thus the accretion rate can be estimated from the observed luminosity with an assumption on the value of η. We can define also the Eddington mass accretion rate, $\dot{M}_{\rm Edd}$, that is a mass accretion rate that realizes the Eddington-limit accretion. The mass accretion rate normalized by the Eddington mass accretion rate, $\dot{M}/\dot{M}_{\rm Edd}$,

is also an important parameter to characterize the accretion phenomenon of AGNs.

There are several accretion modes to explain nearby AGNs (see Heckman & Best 2014 for a review). A high accretion rate ($\dot{M}/\dot{M}_{\rm Edd} \gtrsim 0.01$) indicates that the AGN is radiatively efficient, that is seen in quasars and Seyfert galaxies. This is often called the quasar/radiative mode. A low accretion rate ($\dot{M}/\dot{M}_{\rm Edd} \lesssim 0.01$), in contrast, indicates that the AGN is radiatively inefficient. Such accretion is associated with hot gas accretion from the host galaxy or host dark matter halo, and preferentially seen in radio galaxies and LINERs. This is commonly known as the radio/jet mode accretion. However, how the accretion modes are determined remains unclear. In any cases, AGNs are in a phase of the SMBH growth, and many AGNs cause the feedback to their host galaxies at the same time (see Section 1.2.5), so to self-regulate the SMBH growth.

1.2.2 Unified model

In order to elucidate the physical nature of AGNs and SMBHs, one needs to clarify the geometry of AGNs. As already mentioned, emission lines from AGNs can be divided into two subgroups – one is broad permitted emission lines and another is narrow permitted/forbidden emission lines. The typical velocity width of broad emission lines is $\sim$ 1,000–10,000 km s^{-1}, while the typical width of narrow emission lines is $\sim$100–1000 km s^{-1} (e.g., Padovani et al., 2017). Some AGNs show both broad lines and narrow lines, that are called type 1 AGNs (or Seyfert 1s). Some AGNs show no broad emission lines but only narrow lines, that are called type 2 AGNs (or Seyfert 2s). Now we understand that the systematic difference in various observational properties between type 1 and type 2 AGNs is not intrinsic, but caused by orientation-dependent effects (so-called the unified model of AGNs). This model is based on the fact that emission lines with a different width are emitted from different regions – broad line regions (BLRs) that harbor ionized gas clouds orbiting just close to the luminous accretion disk, and narrow line regions (NLRs) that are located at much further from the central source. The BLRs are surrounded by optically-thick gas and dust distributed in a doughnut-like geometry (dusty torus), and accordingly the broad-line emission is obscured and invisible when they are seen from the equatorial direction toward the dusty torus (and therefore the AGN is observed as type 2). Figure 1.6 shows a schematic view of the unified model (e.g., Urry & Padovani, 1995).

This paradigm was observationally confirmed by the detection of broad emission lines in polarization spectra of type 2 AGNs (e.g., Antonucci & Miller, 1985; Miller et al., 1991). This observational result suggests that the emission from BLRs in type 2 AGNs is simply obscured by the optically-thick torus, and the inner structure in type 2 AGNs is essentially the same as that in type 1 AGNs. Also, the bi-conical distribution of narrow-line emitting regions is observed in some nearby AGNs, which supports the unified model (e.g., Fischer et al., 2013), because the observed distribution can be explained by the radiation of ionizing photons confined by the axisymmetric dusty torus. The details of this narrow emission-line region are described in the next section.

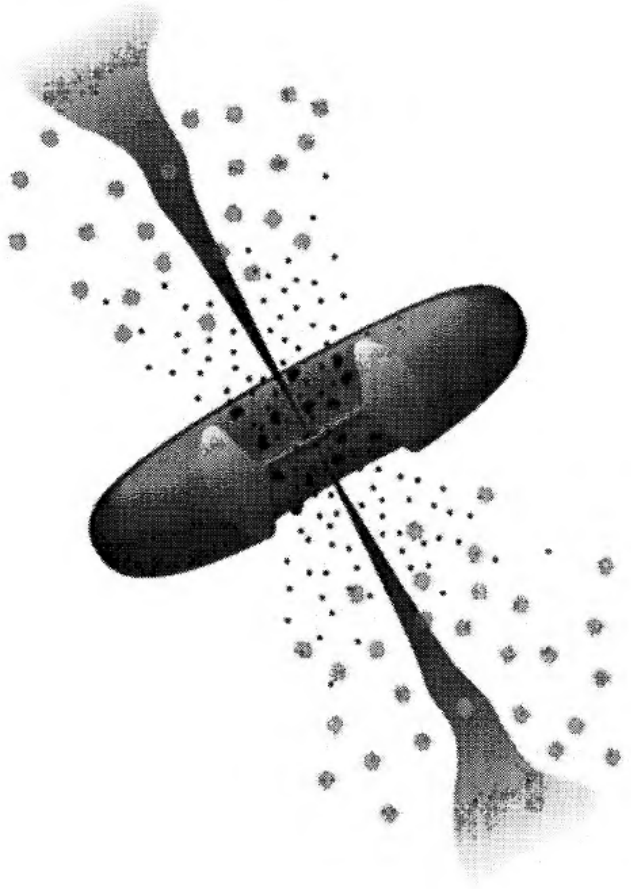

Fig. 1.6: A schematic view of the classical unified model paradigm (Urry & Padovani, 1995). Broad emission lines are produced in clouds orbiting at the very inner part of the AGN. A thick dusty torus obscures the BLR from the line-of-sight toward observers at the equatorial direction toward the dusty torus. Narrow lines are produced in clouds much farther from the central source. Radio jets emanate from the region near the SMBH.

1.2.3 Narrow line regions

The narrow-line regions (NLRs) emit permitted and forbidden narrow emission lines, and exist farther away from the nuclei (typically extends up to several kpc: e.g., Bennert et al. 2006a). The kinematics of NLRs is similar to the galaxy rotation, except for the additional outflowing component caused by the AGN radiative pressure. The gas density of ionized clouds in NLRs is typically $\sim 10^{2-6}$ cm^{-3} (e.g., Netzer, 1990; Osterbrock & Ferland, 2006), that is much lower than that in BLRs ($\sim 10^{11}$ cm^{-3}). This relatively low density is the reason why various forbidden lines are strongly emitted from NLRs. The ionization source of gas clouds in NLRs is mainly thought to be the photoionization by ionizing photons from the central engine of AGNs (e.g., Binette et al., 1996; Komossa & Schulz, 1997; Groves et al., 2004; Thomas et al., 2016). However, sometimes the fast shock also contributes to the ionization of gas clouds in NLRs, that is discussed in details at Chapter 2.

1.2.4 Chemical properties of AGNs

The estimation of the chemical composition of the ISM in AGNs has been carried out by emission-line diagnostics combined with detailed photoionization models (e.g., Groves et al., 2006; Nagao et al., 2006b,c; Matsuoka et al., 2018a; Xu et al., 2018). For low-z AGNs, the metallicity of gas clouds in NLRs of AGNs is inferred to be super-solar, $Z \sim 2-4\ Z_{\odot}$ (e.g., Groves et al., 2006). In high-z quasars (type 1 AGNs), ultraviolet emission line diagnostics have been used for estimating the metallicity of BLRs (e.g., Hamann & Ferland, 1993, 1999; Nagao et al., 2006b; Matsuoka et al., 2017; Xu et al., 2018), suggesting that BLRs also show super-solar metallicity, even at $z > 6$ (e.g., Jiang et al., 2007; Kurk et al., 2007; Juarez et al., 2009).

In high-z type 2 AGNs, some strong UV lines (such as N Vλ1240, C IVλ1549, He IIλ1640, and C III]λ1909) have been used for diagnostic studies so far (e.g., Nagao et al., 2006b; Villar-Martín et al., 2007; Humphrey et al., 2008; Matsuoka et al., 2009; Dors et al., 2014; Morais et al., 2017; Matsuoka et al., 2018a). These results suggest that the host galaxies of HzRGs had already chemically matured at $z \sim 4$ without significant redshift evolution for the redshift range of $1 < z < 4$.

1.2.5 AGN feedbacks

The AGN feedback, which is a negative/positive feedback effect on the star-formation activity in their host galaxies, is gaining more and more attention recently. Understanding the feedback process caused by AGNs is one of the most key issues to reveal the coevolution of galaxies and SMBHs. This effect is considered as a possible solution for a serious problem that theoretical simulations predict too many massive galaxies due to long-duration star formation, in contrast to early-time quenching of star formation in observed massive galaxies (e.g., Di Matteo et al.,

2005; Bower et al., 2006; Croton et al., 2006; Dubois et al., 2016).

Some models posit that the rapid growth of galaxies and SMBHs is triggered by mergers, interactions, and violent instabilities that can also disrupt the gas content of the galaxy and shroud the AGN (e.g., Sanders et al., 1988; Hopkins et al., 2008). Hopkins et al. (2008) showed a schematic picture for the galaxy-SMBH coevolution induced by a gas-rich major merger (Figure 1.7). Some of these merger scenarios for the galaxy-SMBH coevolution predict an intense starburst induced by the merger, which triggers also the AGN activity at the nucleus of such systems. Such AGNs are often observed as obscured AGNs, that seems to be an important phase in the SMBH and galaxy growth (e.g., Blecha et al., 2018). This obscured phase is followed by a blowout phase. Through this phase, the AGN transfers the energy to its surroundings by ejecting the energy and/or gas, and quenches the star-formation activity in the host galaxy and also the AGN activity (i.e., the SMBH growth) correspondingly (e.g., Ishibashi & Fabian, 2016).

Recent numerical simulations show that the AGN feedback is the most likely explanation for the observed relationship between the SMBH mass and stellar velocity dispersion (e.g., Di Matteo et al., 2005). Although it seemed challenging to transmit the energy very efficiently from the AGN to the ISM, it turned out that only a fraction (~ 5 %) of the kinetic energy and AGN bolometric luminosity is required to regulate the star formation (e.g., Zubovas & King, 2012). Harrison et al. (2018) recently showed a summary for observations and theoretical predictions of the energy budget of the AGN outflow. On the other hand, the observationally inferred kinetic energy of the AGN-driven outflow is < 1 % of the AGN bolometric luminosity (e.g., Schlesinger et al., 2009; Dunn et al., 2010; Storchi-Bergmann et al., 2010). Other physical mechanisms are thus required in the AGN feedback so to transfer more energy to the ISM.

The evidence of the AGN feedback is nowadays observed in many ways. Generally, AGNs show some outflowing phenomena reaching up to kpc scales such as radio jets and AGN winds (e.g., Crenshaw et al., 2003; Veilleux et al., 2005; Feruglio et al., 2015). The outflows are also observed indirectly by absorption features in AGN spectra, such as broad absorption lines (BALs; e.g., Weymann et al. 1991; Gibson et al. 2009), and ultra fast outflows (UFOs; e.g., Tombesi et al. 2010). These phenomena are considered as "negative feedback" to the ISM. This is because such outflows blow the gas out from the host galaxy, and consequently it suppresses both star formation and SMBH mass accretion (e.g., Fabian, 2012; Harrison, 2017). The evidence for the negative feedback has been reported by some observational studies (e.g., Moe et al., 2009; Alatalo et al., 2015; Veilleux et al., 2017; Bing et al., 2019), while it is claimed that the negative feedback in some AGNs is insufficient to regulate the star formation (e.g., Villar-Martín et al., 2016; Spacek et al., 2017; Shangguan et al., 2018). On the other hand, these outflows are also thought to cause a "positive feedback" through the condensation of the ISM by jets and outflows that results in the enhancement of the star-formation activity (e.g., Bicknell et al., 2000; Cresci et al., 2015; Mahoro et al., 2017). This positive feedback has been studied also in many theoretical works (e.g., Silk & Nusser, 2010; Dugan et al., 2014; Bieri et al., 2016).

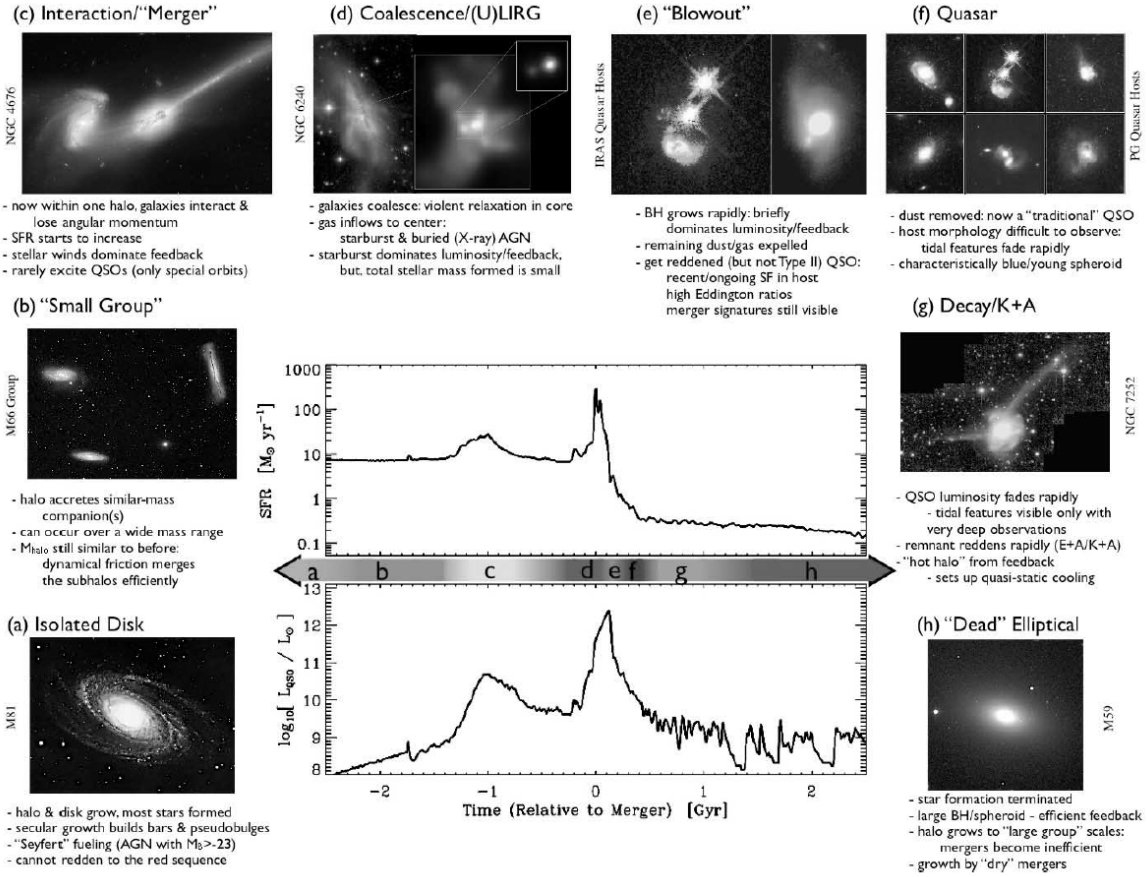

Fig. 1.7: Schematic view of various stages of the galaxy-SMBH coevolution induced by a gas-rich major merger (Hopkins et al., 2008). The upper and lower diagrams in the central panel show the SFR and AGN luminosity of a galaxy as a function of time based on numerical simulations. The figures around the central panel show images at each "epoch" (labeled with an alphabetical character, which corresponds to the epoch shown at the middle in the central panel) during an evolution of a typical galaxy.

Therefore, understanding the AGN feedback is necessary to reveal the coevolution of galaxies and SMBHs in addition to formation of massive galaxies. However, how the AGN activity transmits its energy to the ISM remains a serious mystery. We here investigate the shock ionization of the ISM as a possible physical mechanism of the AGN feedback, i.e., the AGN activity inputs its energy to the ISM through a shock heating induced by a jet or AGN wind (see Chapter 2).

1.3 The physics of the radiation process of emission lines

Emission-line spectra from the ISM tell us information about its physical state and heating source. For example, the detection of hydrogen recombination lines immediately tells us the presence of hydrogen-ionizing photons (i.e., photons with the energy higher than 13.6 eV) in the incident radiation. When the incident ionizing radiation is a blackbody from a hot star, a spherical zone of fully-ionized hydrogen region (Strömgren sphere) with a very sharp boundary (e.g., Osterbrock & Ferland, 2006) is created around the star. Inside this boundary, hydrogen is completely ionized. The radius of this boundary is called the Strömgren radius. Figure 1.8 shows the simulated ionization structure of hydrogen and oxygen ionized by blackbody radiation with $T = 40{,}000$ K, calculated with the public photoionization code Cloudy (Ferland et al., 2013) assuming the solar chemical composition without dust grains. Beyond the radius at the outer edge of the Strömgren sphere (Strömgren radius), the ionization fraction of hydrogen sharply drops close to zero. Interestingly, neutral oxygen has almost the same ionization potential (13.6 eV) as hydrogen and thus the relative abundance of singly-ionized oxygen drops around the Strömgren radius like ionized hydrogen. Ionic species with a higher ionization potential than hydrogen exist at inner part in the Strömgren sphere, such as doubly-ionized oxygen (see Figure 1.8). On the other hand, the AGN radiates power-law continuum radiation that extends to X-ray (or even much higher energy with a power-law spectral energy distribution). In this case, the photoionization cross-section of hydrogen to such high-energy photons is significantly smaller than that to UV photons (since the frequency dependence of the photoionization cross section is roughly proportional to ν^{-3}). Therefore X-ray photons reach far beyond the Strömgren radius and form a further ionized region, that is so-called the partial ionized region or X-ray dissociation region (XDR). Therefore, the ionization structure of gas clouds ionized by AGNs is completely different from H II regions as shown in Figure 1.9. This partially-ionized region is important to understand the observed emission-line spectrum of AGNs, especially low-ionization emission lines such as [O I]λ6300.

Atoms and molecules gain energy through the absorption of photons and/or collision with free electrons, resulting in the excitation and/or ionization of the particle. The wavelength of emission lines corresponds to the energy difference between the two energy levels related to the energy transition. There are two excitation mechanisms; one is caused by the absorption of a photon whose frequency corresponds to the energy required to the transition, and the another one is caused by the collision with free electrons. There are some deexcitation mechanisms, that are spontaneous emission, stimulated emission, and collisional deexcitation. All of these

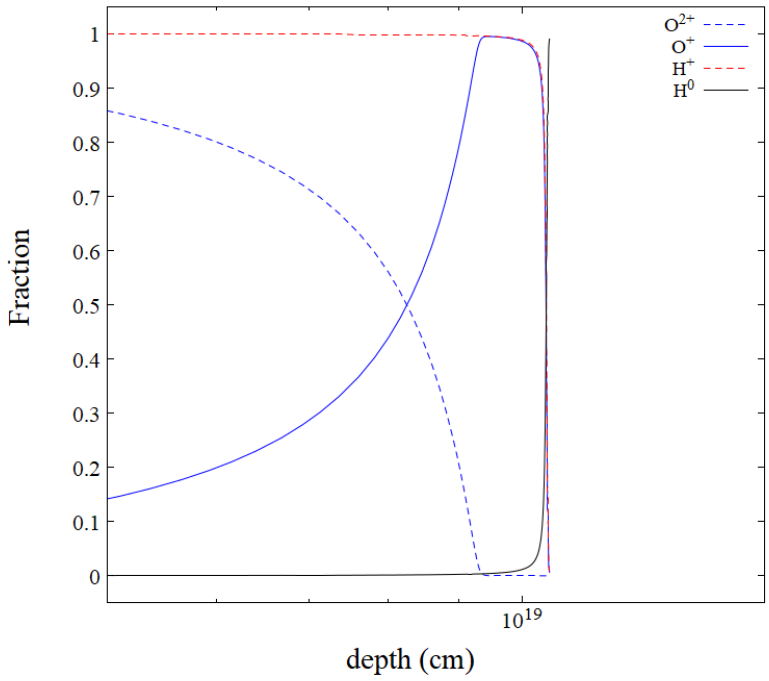

Fig. 1.8: An example of ionization structure of hydrogen and oxygen in a model for H II regions calculated by Cloudy. The depth represents the distance from the incident surface of gas cloud. This calculation stopped when the ionization fraction of hydrogen drops to 1 %. The assumed incident radiation is composed by a blackbody spectrum with T = 40000 K and ionization parameter $\log U = -1.0$. The assumed gas density of the cloud is $n_{\rm H} = 10^2$ cm^{-3}.

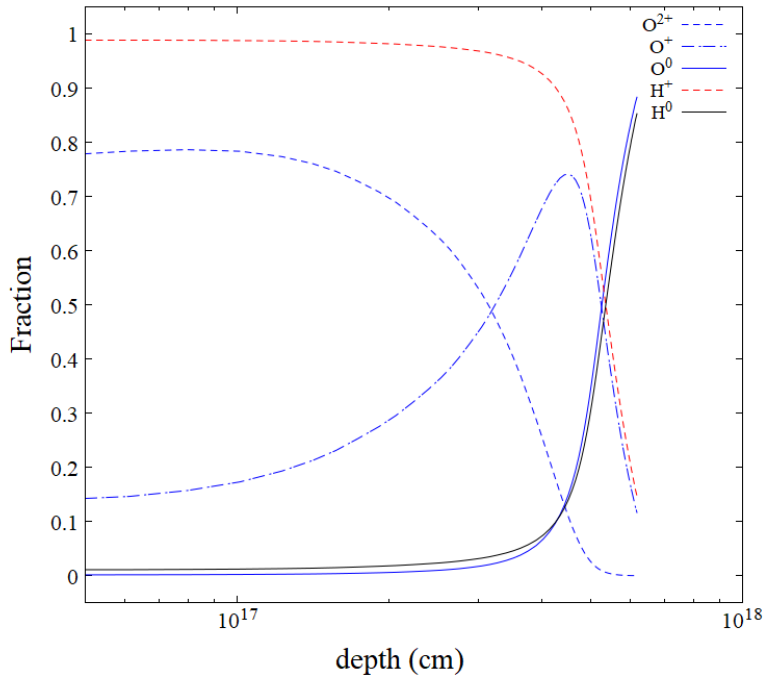

Fig. 1.9: An example of ionization structure of hydrogen and oxygen in a model for NLR clouds calculated by Cloudy. The depth represents the distance from the incident surface of gas cloud. This calculation stopped when the ionization fraction of hydrogen drops to 15 %. The assumed incident radiation, ionization parameter, and gas density of the cloud are a typical AGN spectrum (Mathews & Ferland, 1987), $\log U = -3.0$, and $n_{\rm H} = 10^2$ cm^{-3}, respectively.

transitions occur with a quantum-mechanical probability, which is described by the Einstein coefficient. The transitions occurred by radiating or absorbing photons follow the so-called selection rules as shown below; the orbital angular momentum of electron must change by one ($\Delta l = \pm 1$), the total angular momentum (J) satisfies $\Delta J = 0$ or $\pm$ 1 except for the transition from J = 0 to 0, the total orbital angular momentum (L) also satisfies $\Delta L = 0$ or $\pm$ 1 except for the transition from $L = 0$ to 0, and the total spin (S) must not change. The emission lines caused by transitions satisfying these selection rules are called the permitted emission lines. On the other hand, the forbidden emission lines are caused through transitions that do not satisfy the selection rules of the electric dipole radiation. Such forbidden emission lines occur through the transition by the magnetic dipole radiation or electric quadrupole radiation with a very low transition probability. Therefore the spontaneous emission coefficient of such forbidden transitions is very small.

Due to this very low transition probability of forbidden transitions, the emissivity of forbidden lines is very sensitive to the gas density. This is because the collisional deexcitation becomes more important than the spontaneous forbidden transition at a higher gas density in such a situation. Thus the collisional deexcitation is not negligible at all when we discuss the behavior of forbidden lines. For simple considerations of such density-dependent forbidden transitions, a model atom with only two energy levels is sometimes assumed. In this case, the transition between upper and lower levels is explained by three paths, that are spontaneous radiation, collisionally excitation, and collisonally deexcitation. Thus the balance between the two levels is described by the following equation,

$$N_2(A_{21} + N_e \alpha_{21}) = N_1 N_e \alpha_{12}, \tag{1.1}$$

where N_1 and N_2 are the number of atoms in each level, N_e is the number of free electron, A_{21} is the Einstein coefficient for the spontaneous radiation, and α_{12} and α_{21} are collisional coefficient at each level. The number of photons radiated through the transition from the level 2 to 1 (Q_{21}) by the transition from 2 to 1 is represented by $Q_{21} = N_2 A_{21}$. This is combined with the above equation, and then the following equation is obtained;

$$Q_{21} = \frac{N_1 N_e A_{21} \alpha_{12}}{A_{21} + N_e \alpha_{21}} \, . \tag{1.2}$$

Here, the critical density (n_{cr}) is defined by $n_{cr} = A_{21}/\alpha_{21}$. In a $N_e \ll n_{cr}$ case that is equivalent to $N_e \alpha_{21} \ll A_{21}$, the equation (1.2) is rewritten to $Q_{21} \sim N_1 N_e \alpha_{12}$. In this case, the transition probability of the spontaneous radiation becomes much higher than that of the collisional deexcitation even for forbidden lines, and thus almost all excited atoms show the spontaneous transition from the upper level to the lower level. Therefore, forbidden lines can be radiated in a low-density circumstance. On the other hand, in a $N_e \gg n_{cr}$ case that is equivalent to $N_e \alpha_{21} \gg A_{21}$, the equation (1.2) is rewritten to $Q_{21} \sim N_1 A_{21} \frac{\alpha_{12}}{\alpha_{21}}$. In this situation, the emissivity of forbidden lines is proportional to the spontaneous coefficient of forbidden lines (A_{21}). However, forbidden lines are not visible, because their A_{21} is very small ($\lesssim 10^{-3}$). The collisional deexcitation becomes predominant beyond the critical density and then the corresponding forbidden emission lines are suppressed. Therefore the combination of forbidden emission lines

with different critical densities enables us to diagnose the density of ISM (e.g., Osterbrock & Ferland, 2006).

Detailed comparisons of multiple forbidden emission-line fluxes with models are necessary to discuss the physical and chemical properties of ISM based on the observational result. As for the AGN, which is the main topic of this dissertation, ionized gas clouds in both NLRs and BLRs are thought to be mostly photoionized (but see Chapter 2 for the assessment of the ionization mechanism of gas clouds in NLRs), and thus theoretical calculations with photoionization models are required for assessing the characteristics of the gas clouds. In this dissertation, a widely-used public code of photoionization models, Cloudy version 13.03 (Ferland et al., 2013), is used. The radiative transfer equations in gas clouds illuminated by incident light are properly considered in Cloudy, and thus Cloudy can predict emission-line spectra emitted from ionized gas clouds in various states.

1.4 The purpose of this doctoral dissertation

The emission-line diagnostics are useful for investigating the physical and chemical properties of the ISM in galaxies. These properties are key to understand the formation and evolution of galaxies. AGNs are very luminous objects and thus one of the optimal targets for the diagnostics even in high-z Universe. In this dissertation, we describe the investigation for the ISM properties of galaxies through the emission-line diagnostics particularly focusing on AGNs.

We investigate the possible contribution of shock ionization, that is ionization mechanism of gas clouds in NLRs of AGNs. The fast shock is a possible mechanism of the AGN feedback, i.e., the AGN activity inputs its energy to the ISM through a shock heating induced by a jet or AGN wind. We analyzed near-infrared narrow emission line ratios of some nearby Seyfert galaxies, whose results are given in Chapter 2 (Terao et al., 2016) to investigate the possible contribution of the shock ionization in NLRs of nearby AGNs.

The properties of the NLR in high-z radio galaxies assessed by rest-UV emission lines and detailed photoionization models are described in Chapter 3. Thanks to the spatial extension of NLRs ($\sim$ kpc), their emission lines trace the properties of the ISM in host galaxies. Such high-z radio galaxies are considered to be progenitors of massive elliptical galaxies as seen in the local Universe. Since the formation and evolution of massive galaxies are still observationally unclear, this doctoral dissertation will give some new insights into the study of the formation and evolution of massive galaxies.

CHAPTER 2

IONIZATION MECHANISM OF THE NLR OF LOW-z AGNS[1]

One of the important unsettled problems regarding active galactic nuclei (AGNs) is the major ionization mechanism of gas clouds in AGN narrow-line regions (NLRs). In order to investigate this issue, we present our J-band spectroscopic observations of a sample of 26 nearby Seyfert galaxies. In our study, we use the flux ratio of the following two forbidden emission lines, [Fe II]1.257μm and [P II]1.188μm because it is known that this ratio is sensitive to the ionization mechanism. We obtain the [Fe II]/[P II] flux ratio or its lower limit for 19 objects. In addition to our data, we compile this flux ratio (or its lower limit) for 23 nearby Seyfert galaxies from the literature. Based on the collected data, we find that three Seyfert galaxies show very large lower limits of the [Fe II]/[P II] flux ratios ($\gtrsim 10$): NGC 2782, NGC 5005, and Mrk 463. It is thus suggested that the contribution of the fast shock in the gas excitation is significantly large for them. However, more than half of Seyfert galaxies in our sample show moderate [Fe II]/[P II] flux ratios (~ 2), which is consistent with pure photoionization by power-law ionizing continuum emission. We also find that the [Fe II]/[P II] flux ratio shows no clear correlation with the radio loudness, suggesting that the radio jet is not the primary origin of shocks in NLRs of Seyfert galaxies.

2.1 Introduction

Over the last two decades, it has been observationally suggested that the evolution of galaxies is intimately related to the growth of supermassive black holes (SMBHs) in galactic nuclei based on various scaling relations between the mass of SMBHs ($M_{\rm BH}$) and properties of their host galaxies (e.g., Magorrian et al. 1998; Marconi & Hunt 2003; Di Matteo et al. 2005; see, for reviews, Kormendy & Richstone 1995; Kormendy & Ho 2013). It is also known that a significant fraction of galaxies shows nuclear activity that is driven by the gas accretion onto an

[1]This chapter is described based on Terao et al. (2016).

SMBH (Rees, 1984; Ho et al., 1997b). Such active galactic nuclei (AGNs) emit huge radiative energy. In addition to the strong radiation, AGNs sometimes show strong outflows in various forms, which are recognized as the radio jet (e.g., Wilson & Willis, 1980; Gallimore et al., 2006), broad absorption-line (BAL) feature (e.g., Weymann et al., 1991; Gibson et al., 2009), ultra-fast outflow (UFO; e.g., Cappi 2006; Tombesi et al. 2010), and so on. The radiative and mechanical energies released are expected to have significant impact on various properties of the interstellar medium (ISM) in host galaxies, which may lead to the termination of star-forming activity. This "AGN feedback" possibly holds an important role in the galaxy-SMBH coevolution, and therefore there have been extensive observational effort to understand the AGN feedback phenomena (see Fabian 2012 for a review).

To study the AGN feedback, one interesting approach is focusing on the narrow-line region (NLR) in AGNs. This is because (1) the typical spatial scale of the NLR is $\sim 10^{1-4}$ pc, covering the spatial scale of host galaxies, and (2) the ionized gas clouds in the NLR radiate a variety of emission lines that enable us to diagnose the physical and chemical properties of the ISM in NLRs. It is widely believed that the dominant ionization mechanism of ionized gas clouds in NLRs is photoionization by ionizing photons from the AGN central engine (e.g., Binette et al., 1996; Komossa & Schulz, 1997; Groves et al., 2004). However, it has been sometimes claimed that the fast shocks may also contribute significantly to the ionization in the NLRs of some AGNs (e.g., Knop et al., 1996; Bicknell et al., 1998; Wilson & Raymond, 1999; Fu & Stockton, 2007). Discriminating the ionization mechanisms of gas clouds in the NLR is important in terms of the AGN feedback, because it is closely related to the question of whether either radiative or mechanical heating is important for the gas in NLRs. Unfortunately, emission-line diagnostics in the rest-frame optical and ultraviolet range are not powerful enough to discriminate the ionization mechanism of NLR gas clouds, since the photoionization by the power-law spectral energy distribution (SED) and the fast shock results in very similar emission-line flux ratios (e.g., Dopita & Sutherland, 1995, 1996; Allen et al., 2008).

A powerful method to determine the ionization mechanism of NLR gas clouds was proposed by Oliva et al. (2001). They reported that the flux ratio of two forbidden emission lines seen in near-infrared J-band, [P II]1.188μm and [Fe II]1.257μm, is useful to determine the ionization mechanism. The reason is as follows. These two transitions have similar critical densities ($n_{\rm cr} = 5.3\times10^4$ cm^{-3} for [P II]1.188μm and $n_{\rm cr} = 3.5\times10^4$ cm^{-3} for [Fe II]1.257μm at 10,000 K; Koo et al. 2013), and the ionization potentials of the related ions are both below 13.6 eV, which is the hydrogen ionization potential (7.9 eV for [Fe II] and 10.5 eV for [P II]). Therefore, these two lines should arise at similar locations in NLRs; more specifically, they are both mainly from partially ionized gas (see, e.g., Mouri et al., 2000). Consequently, their flux ratio should be almost proportional to the gas-phase abundance ratio of phosphorus and iron. Here, the iron is a well-known refractory species, and thus most of the iron is usually locked into dust grains. On the other hand, the depletion of phosphorus onto dust grains is only moderate (see, e.g., Cardelli et al., 1991). This means that the gas-phase elemental abundance ratio of iron to phosphorus in NLR gas clouds photoionized by the power-law ionizing radiation is significantly lower than the solar elemental abundance ratio due to the selective depletion of irons

onto dust grains. However, dust grains are easily destroyed due to fast shocks, and thus the relative abundance of the gas-phase iron in shock-dominated NLRs should be much higher than that in photoionized gas clouds. Therefore, the flux ratio of [Fe II]/[P II] is expected to be much higher in shock-dominated clouds ($\gtrsim 20$) than in photoionized clouds (~ 2). Observations of nearby AGNs show that the measured [Fe II]/[P II] flux ratio is actually in the range of $\sim$ 2–20 (Storchi-Bergmann et al., 2009; Riffel et al., 2010; Riffel & Storchi-Bergmann, 2011; Schönell et al., 2014), and the flux ratio also varies with the location in the NLR (e.g., Storchi-Bergmann et al., 2009; Riffel et al., 2010, 2014, 2015; Hashimoto et al., 2011; Riffel & Storchi-Bergmann, 2011; Schönell et al., 2014). Note that this flux ratio is totally free from the dust reddening, thanks to the narrow wavelength separation between the two lines, which makes this flux ratio a powerful diagnostic tool for investigating the ionization mechanism of NLRs.

Though the [Fe II]/[P II] flux ratio is an interesting tool to explore the nature of AGN feedback on the NLR scale, this emission-line flux ratio has not been measured in many objects so far ($\sim$ 20 objects; e.g., Oliva et al. 2001; Ramos Almeida et al. 2006, 2009; Riffel et al. 2006, 2013; Jackson & Beswick 2007; Krajnović et al. 2007; Hashimoto et al. 2011; Riffel & Storchi-Bergmann 2011; Schönell et al. 2014; Riffel et al. 2015). Therefore, it is currently hard to carry out various statistical analyses on the [Fe II]/[P II] flux ratio. Also, the small sample size does not allow us to investigate possible connections between the NLR ionization and AGN outflows such as the radio jet, BAL, and UFO, given the fact that the fraction of AGNs showing those outflow features is relatively low ($\sim$ 10 % for radio jets, $\sim$ 10 % for BALs, and $\sim$ 35 % for UFOs; see, e.g., Tombesi et al. 2010).

In this chapter, we present the result of our J-band spectroscopic observations of the central region in a number of nearby Seyfert galaxies, with the aim to investigate the [Fe II]/[P II] flux ratio and examine the ionization mechanism of gas clouds in the NLR. In Section 2.2, we describe the details of our observations and the data reduction procedure. In Section 2.3, we summarize the obtained results. We discuss the implications of our results in Section 2.4, and then we give the conclusion of this chapter in Section 2.5.

2.2 Observations and data

The targets were selected based on the optical [O III]λ5007 flux (given by Whittle, 1992; Ho et al., 1997a; Risaliti et al., 1999), focusing on objects with relatively strong NLR emission lines. Near-infrared long-slit spectroscopic observations were carried out for 26 nearby Seyfert galaxies and associated standard stars (to correct the telluric absorption features and the wavelength dependence of the sensitivity) from 2010 August to 2011 April with ISLE (Yanagisawa et al., 2006, 2008), a near-infrared imager and spectrograph for the Cassegrain focus of the 188 cm telescope at the Okayama Astrophysical Observatory (OAO). The detector (a HAWAII 1k $\times$ 1k array) provides a $4'.3 \times 4'.3$ field of view with $0''.25$ pixel^{-1} spatial sampling. The observations were performed in the J-band (1.11$-$1.32 μm) using a $2''.0$ width longslit, and the typical nodding width was $\sim 30''$ ($\sim$120 pixels). The slit was oriented to PA $= 90^\circ$ (E–W) for

all targets. The unit exposure time was 120 s, and the total on-source integration times for science targets were 18–288 minutes, depending on the target. The achieved spectral resolution is ~ 1300, which is measured from the width of observed OH airglow emission lines. The typical seeing size was $\sim 1''.0 - 2''.0$, inferred from the spatial extension of standard stars on the two dimensional spectra. We summarize the redshift, J-band magnitude, the AGN activity type, total exposure time, date of observations for each target, and also the corresponding standard star in Table 2.1.

Table 2.1: Observation log

Name	z[a]	m_J[b] (mag)	Type[c]	Exposure Time (minutes)	Date	Standard Star[d]	m_J[e] (mag)
NGC 1667	0.0152	9.92	Sy 2	114	2011 January 13	HIP 20507 (A2V)	5.09
NGC 2273	0.0061	9.45	Sy 2	94	2011 January 15, 16	HIP 30060 (A2V)	4.28
NGC 2782	0.0085	9.79	Sy 2	552	2011 January 13, 15	HIP 45590 (A1V)	5.76
					2011 March 24, 27		
NGC 3079	0.0037	8.44	Sy 2	68	2011 January 12	HIP 47006 (A2V)	4.63
NGC 3982	0.0037	9.77	Sy 1.9	18	2011 April 25	HIP 62402 (A9V)	5.45
NGC 4102	0.0028	8.76	LINER	110	2011 April 21, 28	HIP 62402 (A9V)	5.45
NGC 4169	0.0126	10.06	Sy 2	68	2011 January 12	HIP 60746 (A4V)	4.80
NGC 4192	−0.0005	7.82	LINER	48	2011 April 26	HIP 59819 (A3V)	5.17
NGC 4258	0.0015	6.38	Sy 2	48	2011 April 23	HIP 64906 (A0V)	5.15
NGC 4388	0.0084	8.98	Sy 2	36	2011 April 24	HIP 59819 (A3V)	5.17
NGC 4419	−0.0009	8.78	LINER[f]	60	2011 April 24	HIP 59819 (A3V)	5.17
NGC 4941	0.0037	9.09	Sy 2	48	2011 April 24	HIP 62983 (A2V)	5.87
NGC 5005	0.0032	7.46	LINER	100	2011 April 23	HIP 62641 (A3V)	5.40
NGC 5194	0.0015	6.40	Sy 2	168	2010 August 14−18	HIP 66234 (A5V)	4.53
NGC 5506	0.0062	9.71	Sy 2	212	2011 April 23, 28	HIP 68092 (A8V)	5.45
NGC 6500	0.0100	10.13	LINER	208	2010 August 16−18	HIP 91118 (A0V)	5.63
						HIP 87192 (A1V)	5.99
NGC 6951	0.0048	8.31	Sy 2	74	2010 August 12	HIP 102253 (A8V)	5.18
Mrk 3	0.0135	10.03	Sy 2	56	2011 January 12	HIP 29997 (A0V)	4.97
Mrk 6	0.0188	11.08	Sy 1.5	64	2011 January 13	HIP 29997 (A0V)	4.97
Mrk 34	0.0505	12.77	Sy 2	26	2011 April 26	HIP 52478 (A0V)	5.80
Mrk 463	0.0504	12.16	Sy 2	160	2011 April 24, 26, 28	HIP 68276 (A0V)	5.67
Mrk 477	0.0377	12.95	Sy 2	84	2010 August 10, 12	HIP 71573 (A1V)	5.76
Mrk 509	0.0344	11.58	Sy 1.5	166	2010 August 14, 15	HIP 102618 (A1V)	3.85
Mrk 766	0.0129	11.10	Sy 1	84	2011 April 26	HIP 60746 (A4V)	4.80
Mrk 1073	0.0233	11.26	Sy 2	288	2010 August 12, 14−18	HIP 15648 (A3V)	4.80
MCG +08-11-011	0.0205	10.49	Sy 1.5	100	2011 January 12	HIP 25143 (A3V)	5.14

[a]Redshift taken from the NASA/IPAC Extragalactic Database (NED).
[b]Apparent total J-band magnitude (in Vega), taken from the 2MASS All-Sky Extended Source Catalog (Skrutskie et al., 2006).
[c]Activity classification is taken from Véron-Cetty & Véron (2010), unless a remark is given.
[d]Spectral type of each standard star is given in the parentheses.
[e]Apparent J-band magnitude (in Vega) taken from the 2MASS All-Sky Catalog of Point Sources (Cutri et al., 2003).
[f]Boselli et al. (2014).

The data analysis was performed using the IRAF software (Tody, 1986, 1993) in the standard manner: i.e., flat fielding, background subtraction, stacking individual spectra, spectral extraction from two-dimensional spectra, wavelength calibration, correction for the atmospheric absorption and sensitivity function using the spectra of standard stars, and finally conversion of the spectra from the observed frame to the rest frame. We adopted a $2''.0$ (8 pixels) aperture for the spectral extraction, taking account the seeing size during the observations. The magnitude

and spectral type of standard stars were collected from the 2MASS (*Two Micron All Sky Survey*) All-Sky Catalog of Point Sources (Cutri et al., 2003) and the *Hipparcos* and *Tycho* catalogues (ESA, 1997), respectively. During the process of correcting for the atmospheric absorption and sensitivity function, a blackbody spectrum with the temperature corresponding to the spectral type was assumed as the intrinsic spectrum. The fluxes, central wavelengths, and FWHMs of the detected emission lines were measured with the IRAF command `splot`, assuming a single Gaussian for each emission line. For undetected emission lines, we calculate the 3σ flux upper limit based on the rms of the spectra around the expected wavelength, assuming a velocity width of 500 km s^{-1} in FWHM, which is the typical value for the detected emission lines in our observations.

2.3 Results

The fully reduced spectra of the 26 Seyfert galaxies are shown in Figure 2.1. Here the flux scale is normalized by the flux density of the continuum emission at $\lambda_{\rm rest}$ = 1.235 μm. The [P II] emission is significantly detected in 6 objects (NGC 5506, Mrk 3, Mrk 6, Mrk 477, Mrk 1073, and MCG +08-11-011) of the 26 targets, while 19 objects show the significant [Fe II] emission. The Paβ emission is also detected in 11 objects, but we do not measure the emission-line properties of Paβ for Mrk 6 and MCG +08-11-011 because of their very complex spectral profiles. The measured central wavelength and velocity width in FWHM for each detected emission line are given in Table 2.2, and the derived flux ratios of [Fe II]/[P II] and [Fe II]/Paβ are given in Table 2.3. The averages and standard deviations of the velocity width of the detected emission lines are 717 $\pm$ 265 km s^{-1}, 596 $\pm$ 337 km s^{-1}, and 497 $\pm$ 321 km s^{-1} (for [P II], [Fe II], and Paβ, respectively) in FWHM.

In addition to the results obtained in our observations, we also collected flux ratios of [Fe II]/[P II] and [Fe II]/Paβ from the literature in order to expand the sample size to enable better statistical analyses of the flux ratios. The compiled flux ratios for 23 objects are summarized in Table 2.4.

Figure 2.2 shows the histograms of the measured [Fe II]/[P II] flux ratio or its lower limit of the objects observed in our OAO observations and also compiled from the literature. The averages and standard deviations of the [Fe II]/[P II] flux ratio for objects with [P II] detected in our OAO sample and in the sample from the literature are 4.24 $\pm$ 1.47 and 2.83 $\pm$ 1.15, respectively. Note that Mrk 766 is included in both our OAO sample and also the sample compiled from the literature, and both of the independent data of Mrk 766 are shown in Figure 2.2. Specifically, Schönell et al. (2014) reported that [Fe II]/[P II] = 2.654 $\pm$ 0.164, which is consistent with our result ([Fe II]/[P II] $>$ 2.483). Hereafter we adopt the flux ratio reported by Schönell et al. (2014) for Mrk 766. Mrk 34 is also included in our sample and in the sample from the literature; we adopt the flux ratio reported by Jackson & Beswick (2007) since our OAO observation did not detect any emission lines (see Figure 2.1). Our OAO observations show the presence of many nearby AGNs with lower limits of [Fe II]/[P II] flux ratios that have

not been often reported in the literature. This may be partly because the lower limit of the [Fe II]/[P II] flux ratio for objects with [P II] undetected has been unreported in the literature.

Figure 2.3 shows the histograms of the measured [Fe II]/[P II] flux ratio or its lower limit for each AGN type. The averages and standard deviations of the [Fe II]/[P II] flux ratio for unobscured (i.e., type 1 and type 1.5) Seyfert galaxies (9 objects) and obscured (i.e., type 2) Seyfert galaxies (16 objects) with [P II] detected are 2.78 ± 0.82 and 3.32 ± 1.53, respectively. Though there may be a tendency that objects showing a large [Fe II]/[P II] flux ratio are in the Seyfert 2 and LINER samples, we cannot statistically conclude this because of small sample sizes in this work. Note that a Fanaroff-Riley type I (FR I) galaxy, NGC 5128, shows a moderate value of the [Fe II]/[P II] flux ratio (~ 3.0; see Table 2.4), despite the presence of a radio jet. We will discuss the implication for the relation between the radio jet and the ionization mechanism of the NLR gas clouds inferred from the measured [Fe II]/[P II] flux ratio in Section 2.4.2.

2.4 Discussion

2.4.1 Emission-line flux ratios of the targets

As shown in the previous section, we measured the flux ratio of [Fe II]/[P II] for 6 objects with [P II] detection in our OAO sample and collected 22 objects from the literature, for a total of 28 objects with [P II] detected. The average and standard deviation of this flux ratio for the 28 objects with [P II] detected are 3.13 ± 1.33, and the median value is 2.88 (see also Tables 2.3 and 2.4). This is roughly consistent with the prediction of photoionization models, that expect ~ 2 for the [Fe II]/[P II] ratio (e.g., Oliva et al., 2001). On the other hand, some objects show a much higher ratio of [Fe II]/[P II], reaching ~ 10 or even more. As demonstrated by Oliva et al. (2001), such a high [Fe II]/[P II] ratio suggests a significant contribution of fast shocks to the ionization of NLR gas clouds. It is therefore concluded that shock-dominated NLRs actually exist, at least in some NLRs of AGNs in the nearby Universe.

Some previous long-slit and integral-field unit observations show the spatial variation of the [Fe II]/[P II] flux ratio in some nearby Seyfert galaxies, in the sense that the [Fe II]/[P II] flux ratio increases as a function of the distance from the nucleus (e.g., Storchi-Bergmann et al., 2009; Riffel et al., 2010; Hashimoto et al., 2011). The flux ratio reaches up to ~ 10 at the outer part of NLRs in NGC 4151 (Storchi-Bergmann et al., 2009) and Mrk 1066 (Riffel et al., 2010), suggesting that the shock contribution could be much more significant at the outer part than the inner part of NLRs. This trend is a natural consequence of the geometrical dilution of ionizing photons from the nucleus (see also, e.g., Jackson & Beswick 2007). However, the surface emissivity of emission lines at the outer part of NLRs is generally much lower than the inner part of NLRs, and thus the integrated NLR spectrum of AGNs does not necessarily show shock-dominated line-flux ratios even if the outer part of NLRs shows such a high [Fe II]/[P II] flux ratio. Our OAO/ISLE spectra are extracted at the nuclear $2''.0$ region, and the extracted spectra should not be dominated by the outer part of the NLR in the target AGNs. To examine

whether or not our OAO targets with a high flux ratio of [Fe II]/[P II] are affected by such a possible aperture effect, we show the relation between the measured [Fe II]/[P II] flux ratio and the physical scale covered by the aperture size (= $2''.0$) at the target redshift in Figure 2.4. Though a positive correlation between the measured [Fe II]/[P II] flux ratio and the physical scale covered by the adopted aperture is expected if the high [Fe II]/[P II] flux ratio seen in our sample is caused by the significant contribution of the outer part of NLRs, Figure 2.4 does not show such a significant positive correlation. This suggests that the high [Fe II]/[P II] flux ratio seen in some objects in our OAO sample is not due to the geometrically diluted ionizing photons at the outer part of NLRs.

It has been reported that enhancement of the [Fe II]/Paβ flux ratio, and not only of the [Fe II]/[P II] flux ratio, is seen in shock-excited regions (e.g., Larkin et al. 1998; Mouri et al. 2000; Ramos Almeida et al. 2009; Koo & Lee 2015), which is due mostly to the destruction of dust grains by fast shocks. Figure 2.5 shows a clear positive correlation between the [Fe II]/[P II] and [Fe II]/Paβ flux ratios, i.e., objects showing a large [Fe II]/[P II] ratio also show a large [Fe II]/Paβ ratio. This positive correlation has been reported by Ramos Almeida et al. (2009) for a smaller sample (six Seyfert galaxies), but now the correlation is shown for a much larger sample in this work. This supports the interpretation that the large [Fe II]/[P II] ratio seen in NLRs of some AGNs is caused by fast shocks.

Note that at high-ionization parameter where Compton heating becomes significant, the photoionization may also destroy dust grains, resulting in higher [Fe II]/[P II] ratios without fast shocks. Such objects should be distinguished by checking the relative strength of coronal forbidden lines, because their ionization potentials are very high ($\gtrsim$ 100 eV). In order to examine this possibility, we investigate the relative strength of coronal forbidden lines in our samples. We find the [Fe VII]λ6087/[O III]λ5007 flux ratio for 21 objects (20 objects with [P II] detected and 1 object with [P II] undetected) from the literature (Nagao et al., 2000, 2003; Bennert et al., 2006b). Note that this flux ratio is very sensitive to the ionization parameter, in the sense that a higher [Fe VII]λ6087/[O III]λ5007 flux ratio is achieved by a higher ionization parameter (see, e.g., Figure 13 in Nagao et al. 2001a). We also focus on a mid-infrared coronal line of [Ne V]14.32 μm, and compile the [Ne V]14.32 μm/[Ne II]12.81 μm flux ratio for 24 objects (17 objects with [P II] detected and 7 objects with [P II] undetected) from the literature (Pereira-Santaella et al., 2010; Weaver et al., 2010; Wu et al., 2011; Petric et al., 2011; Dasyra et al., 2011). Figures 2.6 and 2.7 show the relation between the [Fe II]/[P II] flux ratio and the relative strength of two coronal forbidden lines. Though we expect a positive correlation in these figures if high-ionization gas clouds without fast shocks result in high [Fe II]/[P II] flux ratios, we do not see such a trend in both figures. These results further support our conclusion that the large [Fe II]/[P II] flux ratio seen in our samples is due to fast shocks and not photoionization with a very high ionization parameter.

2.4.2 Relation between the emission-line flux ratio and radio loudness

As already described, the large [Fe II]/[P II] ratios seen in some AGNs are attributed to fast shocks in NLRs. The simplest idea for the origin of the fast shocks in NLRs is the effect of the AGN jet. Previous radio observations show that AGN jets exist not only in powerful radio galaxies; actually less powerful radio jets, with much smaller spatial extension than those seen in powerful radio galaxies, are seen in many radio-quiet AGNs such as Seyfert galaxies (e.g., Miller et al., 1993; Ulvestad et al., 1999; Nagar et al., 2001). Therefore, such AGN jets including small-scale weak jets may cause fast shocks in NLRs and then the gas-phase iron abundance increases through grain destruction or the sputtering process, resulting in the large [Fe II]/[P II] ratio observed in some AGNs.

To examine whether or not the observed large [Fe II]/[P II] ratio seen in some AGNs can actually be attributed to the AGN jet, the most straightforward test is to investigate the relation between the [Fe II]/[P II] ratio and the power of the AGN jet. To quantify the power of the AGN jet, we adopt the radio loudness (R), defined as the ratio of the flux density of the radio (5 GHz) to the optical (4400 Å), i.e.,

$$R = \frac{\text{5 GHz flux density}}{\text{4400 Å flux density}} \tag{2.1}$$

(Kellermann et al., 1989). In this definition, AGNs are classified as radio-loud and radio-quiet populations at the threshold of $R = 10$ (Kellermann et al., 1989). We calculate the radio loudness by compiling the optical and radio flux densities from previous observations, for both our OAO sample and the sample from the literature. For cases where multiple photometric data are available, we use the data whose aperture size is as small as possible to avoid contributions from the host galaxy. From the compiled photometric data, we derive the flux density at 5 GHz and 4400 Å by adopting the typical spectral index of Seyfert galaxies, i.e., -0.5 (optical) and -0.7 (radio), respectively (Singh et al., 2015).

Figure 2.8 shows the [Fe II]/[P II] flux ratio as a function of the radio loudness in the logarithmic scale. There is no apparent positive or negative correlation between the [Fe II]/[P II] flux ratio and the radio loudness. For objects with [P II] detection, there is no statistically significant difference in the average value of the [Fe II]/[P II] flux ratio between the radio-loud and radio-quiet populations: 3.67 ± 1.09 for 9 objects with $R > 10$ (i.e., radio-loud, including NGC 5128, which is an FR I radio galaxy) and 2.87 ± 1.38 for 19 objects with $R < 10$ (i.e., radio-quiet). We thus conclude that the [Fe II]/[P II] flux ratio is not determined primarily by the AGN jet. Note that this conclusion does not change even when the objects with [P II] undetected are taken into account, because there is only one (Mrk 463) in the radio-loud domain in our samples. This result strongly suggests that the radio jet is not the main origin of fast shocks in NLRs of AGNs.

2.4.3 Relation between the emission-line flux ratio and kinematics

As described in Section 2.1, the [Fe II] and [P II] emission lines arise at similar locations in the NLR due to the similarity of the critical density and ionization potential. Therefore, the velocity profiles of these two lines are expected to be similar to each other. However, NLR clouds affected by fast shocks may be kinematically disturbed. Therefore, the velocity profile of [Fe II] and [P II] emission lines may give us some hints about the contribution of fast shocks in NLRs. Figure 2.9 shows the relation between the [Fe II]/[P II] flux ratio and the FWHM ratio of [Fe II] and [P II], and we see a significant positive correlation between the two quantities. Specifically, AGNs showing a larger [Fe II]/[P II] flux ratio tend to show a wider [Fe II] velocity profile with respect to the [P II] velocity profile. The linear fit to this correlation results in the relation of

$$[\mathrm{Fe\ II}]/[\mathrm{P\ II}] = (4.690 \pm 1.866) \times \frac{\mathrm{FWHM}_{[\mathrm{Fe\ II}]}}{\mathrm{FWHM}_{[\mathrm{P\ II}]}} + (-1.128 \pm 2.174) \tag{2.2}$$

(see Figure 2.9). Note that this positive correlation is not expected if all of the observed flux of the [Fe II] and [P II] emission lines comes from NLR clouds excited by fast shocks, because in this case both [Fe II] and [P II] velocity profiles should be disturbed similarly by the shock and thus the FWHM ratio is expected to be ~ 1. The observed correlation shown in Figure 2.9 is explained by the mixture of the photoionized cloud and shock-excited cloud in NLRs. More specifically, the [Fe II] flux of AGNs with a large [Fe II]/[P II] flux ratio is significantly attributed to fast shocks while the [P II] flux is largely attributed to photoionized clouds in the NLR. This picture is consistent with the fact that the observed [Fe II]/[P II] flux ratio does not reach the value expected from pure shocks (~ 20).

As already described, our results show that the radio jet is not the primary origin of fast shocks in NLRs, at least for the low-z AGNs investigated in this work. What, then, is the origin of fast shocks in NLRs? Recently, powerful AGN-driven outflows were observed in some high-z (e.g., Maiolino et al., 2012; Carniani et al., 2015) and low-z AGNs (e.g., Rupke & Veilleux, 2011; García-Burillo et al., 2014; Feruglio et al., 2015). The possible launching mechanisms of powerful AGN outflows are radiation pressure from the UV photons and/or line force (e.g., Murray et al., 1995; Binette et al., 1997; Proga et al., 2008; Nomura et al., 2016), thermally driven (e.g., Begelman et al., 1983; Krolik & Kriss, 2001), magnetocentrifugal force due to an accretion disk (e.g., Blandford & Payne, 1982; Konigl & Kartje, 1994). Those outflows are characterized by broad (FWHM $\gtrsim$ 1000 km s^{-1}) and/or blueshifted emission lines, mostly extending up to the kiloparsec scale. The opening angle of those outflows is much wider than that of radio jets generally, and such powerful outflows are seen not only in radio-loud AGNs. Therefore, it is strongly suggested that the main driving source of those AGN outflows is not the radio jet. For example, Feruglio et al. (2015) reported the discovery of a molecular outflow spreading ~ 1 kpc in all directions from the nucleus of a type 1 Seyfert Mrk 231 (which is known also as an ultraluminous infrared galaxy, ULIRG) based on CO(2-1) observations. The inferred mass-outflow rate and kinetic energy of the molecular outflow are $\dot{M} = 500 - 1000\ M_{\odot}\mathrm{yr}^{-1}$ and $\dot{E}_{\mathrm{kin}} = 7 - 10 \times 10^{43}$ erg s^{-1}, corresponding to 1–2 % of

the AGN bolometric luminosity. Similarly, Cicone et al. (2014) reported that the ratio of the kinetic energy of the outflow to the AGN bolometric luminosity in 14 low-z luminous AGNs (including ULIRGs) is up to 5 %, also based on CO observations. The value of this ratio is close to the predicted value from theoretical model explaining the $M_{\rm BH} - \sigma$ relation in local galaxies (e.g., Silk & Rees, 1998; Zubovas & King, 2012). Therefore, it is likely that powerful AGN-driven outflows can have impacts on NLR clouds and consequently cause fast shocks in NLRs.

However, the physical origin of such powerful AGN-driven outflows in the galactic scale is also unknown. At a smaller spatial scale in AGNs, powerful outflows are sometimes recognized as the BAL and UFO. Since BAL features are seen in rest-frame UV spectra and thus they are mainly observed in high-z quasars (e.g., Weymann et al., 1991), we here focus on the UFOs, which are seen in the rest-frame hard X-ray spectra of nearby AGNs (e.g., Tombesi et al., 2010). Specifically, the UFO is identified as a blueshifted Fe K absorption line, whose outflowing velocity reaches mildly relativistic values (> 0.033 c). Based on hydrodynamical simulations, Wagner et al. (2013) showed that the uncollimated UFO from the central engine of AGNs has strong feedback effects on the ISM in the host galaxy at the kiloparsec scale, similar to well-collimated radio jets (see, e.g., Wagner et al., 2012). Among our sample, five objects (NGC 4151, NGC 5506, Mrk 79, Mrk 509, and Mrk 766) show the UFO feature in their X-ray spectra (Tombesi et al., 2010; Gofford et al., 2013). These objects show relatively low [Fe II]/[P II] flux ratios that reach only ~ 3, except for NGC 5506 (6.876 ± 0.487) and Mrk 509 (unmeasured). This may suggest that for AGNs with a shock-excited NLR, the NLR is not necessarily associated with the UFO feature in their X-ray spectra. Here it should be noted that the UFO could be still important as a possible origin of fast shocks in NLRs, because AGNs without UFO features may possess powerful nuclear outflows that are not recognized as UFOs due to various effects, such as the viewing-angle effect and obscuration effect. A larger sample of AGNs with measurement of the [Fe II]/[P II] flux ratio and hard X-ray spectra is needed to investigate the possible link between the fast shock in NLRs and the UFO phenomenon.

Moreover, we discuss another possible candidate for the origin of fast shocks: the wind originating from nuclear starburst (e.g., Heckman et al., 1990; Rich et al., 2010; Ho et al., 2014, 2016). In order to examine whether or not the starburst is the main origin of fast shock in the NLR, we investigate two indicators of starburst activity. First, we focus on the far-infrared luminosity ($L_{\rm FIR}$), which is a tracer of starburst activity in galaxies. We adopt the following definition of the far-infrared flux ($F_{\rm FIR}$) to derive $L_{\rm FIR}$,

$$F_{\rm FIR} = 1.26 \times 10^{-11} (2.58 S_{60\mu{\rm m}} + S_{100\mu{\rm m}}) \tag{2.3}$$

where $S_{60\mu{\rm m}}$ and $S_{100\mu{\rm m}}$ are the *IRAS* flux densities in Jy at 60 μm and 100 μm, respectively (Fullmer & Londsdale, 1989; Sanders & Mirabel, 1996), and $F_{\rm FIR}$ is given in unit of erg s^{-1} cm^{-2}. Since the outflow due to the starburst is determined by both starburst activity and depth of the gravitational potential of galaxies, we investigate the far-infrared luminosity normalized by the $K_{\rm s}$-band luminosity ($\nu L_\nu(K_{\rm s})$), where the latter is derived from the total $K_{\rm s}$ magnitude taken from the 2MASS All-Sky Extended Source Catalog (Skrutskie et al., 2006).

Figure 2.10 shows the relation between the [Fe II]/[P II] flux ratio and $L_{\rm FIR}/\nu L_\nu(K_{\rm s})$, and we find no significant positive correlation. This suggests that the large [Fe II]/[P II] flux ratio is not caused by the starburst activity in host galaxies of Seyfert galaxies. Second, we checked the 3.3 μm polycyclic aromatic hydrocarbon (PAH) feature, which is an indicator of nuclear starburst (e.g., Imanishi & Dudley, 2000; Imanishi & Wada, 2004). Since strong PAH emission is expected for starburst galaxies while the PAH is destroyed in pure AGNs, we can infer the strength of the starburst relative to the AGN through the PAH emission. We collected the 3.3 μm PAH data from the literature (Rodríguez-Ardila & Viegas, 2003; Watabe et al., 2008; Oi et al., 2010; Castro et al., 2014). The averages and standard deviations of the [Fe II]/[P II] flux ratio for the objects with PAH detection (7 objects) and no PAH detection (6 objects; upper limit) in the sample with [P II] detected are 3.28 ± 1.75 and 3.52 ± 1.04, respectively. Since there is no systematic difference in the [Fe II]/[P II] flux ratio between the samples with PAH detection and non detection, the contribution of starburst-driven shocks to the [Fe II]/[P II] flux ratio appears to be negligible. Therefore, based on the two tracers of the starburst, $L_{\rm FIR}$ and PAH, we conclude that the starburst is not the primary origin of fast shocks in NLRs.

2.4.4 Suggestions from photoionization models

Rather surprisingly, detailed photoionization model calculations focusing on the [Fe II]/[P II] flux ratio in NLRs have not been performed previously, mainly due to the lack of observations of the [Fe II]/[P II] flux ratios. Here we show some results obtained through the detailed photoionization models using Cloudy v13.03 (Ferland et al., 2013) to see if the observed [Fe II]/[P II] flux ratios can be consistently explained by photoionization models. The plane parallel geometry and constant pressure inside clouds are assumed in our models. Our model parameters and their ranges covered in our study are the following: the ionization parameters ($U = 10^{-3.5} - 10^{-2.5}$), hydrogen density ($n_{\rm H}$ = 10^3 – 10^5 cm^{-3}), and metallicity ($Z = 1 - 4\ Z_\odot$). The adopted relative elemental abundance ratio is the solar composition ("old solar 84"; see Grevesse et al. 1989, 1993), by taking into account of the dust depletion effect that is different for each element (Table 2.6). The parameter ranges covered in our model runs are determined by referring typical values for gas clouds in NLRs (e.g., Nagao et al., 2001b; Matsuoka et al., 2009; Araki et al., 2012). We used three SED models as the incident continuum (Figure 2.11). One is the *table AGN* model, which reproduces the typical SED of AGNs (Mathews & Ferland, 1987). The others are broad-line Seyfert 1 (BLS1; i.e., usual Seyfert 1) and narrow-line Seyfert 1 (NLS1; see, e.g., Osterbrock & Pogge 1985; Boller et al. 1996; Nagao et al. 2002) SED models, which were constructed to create the typical SEDs of BLS1s and NLS1s based on multi-wavelength observational results (Nagao et al., 2001b).

Figures 2.12 – 2.23 show the observational result of [Fe II]/[P II] versus [Fe II]/Paβ with photoionization model grids obtained with each SED template. Our models reproduce the observed [Fe II]/[P II] flux ratios, while the [Fe II]/Paβ flux ratio of our models always show significant offsets from the observed values. We also calculated some models without any depletion, so to increase the relative abundance of Fe and P. Figure 2.24 shows the grid of

non-depletion models with the observational results. In this case, the relative abundance of iron increases by a factor of 100 compared to depleted models, while the relative abundance of phosphorus increases only by a factor of 4. The [Fe II] relative intensity thus becomes much higher than the depleted models, and consequently those model grids can reproduce the observed [Fe II]/Paβ flux ratios. However, the [Fe II]/[P II] flux ratios are now over-predicted due to the non-depleted abundance ratio between iron and phosphorus. These results clearly show that the flux ratios of [Fe II]/Paβ and [Fe II]/[P II] are very sensitive to the depletion factors. Note that the adopted depletion factors listed in Table 2.6 are highly uncertain, due to the observational difficulty to estimate the depletion factor for each element. Therefore, we may consider some systematic uncertainties in the depletion factors as a reason of the discrepancy between observations and photoionization models.

We thus tested another set of photoionization models with the same depletion factor (0.01) for iron but no depletion for phosphorus (see Figure 2.25), following the approach adopted by Oliva et al. (2001). The new treatment of the elemental depletion results in the increase of the [P II] flux by a factor of ~ 4 (not exactly 4 because the relative elemental abundance and the emission-line flux do not obey the one-to-one relation depending on the physical properties of gas clouds), that corresponds to the decrease of the [Fe II]/[P II] flux ratio. This new [Fe II]/[P II] flux ratio predicted by photoionization models may be consistent with some of our observations and also with observations by Oliva et al. (2001) especially for objects that are considered to be photoionization-dominated, but further model calculations with a much wider coverage of gas parameters are needed to examine this in more detail.

From our model predictions, the emission in photoionization-dominated objects characterized by a low [Fe II]/[P II] flux ratio (< 2) was explained with high-density and low-ionized clouds ($n_{\rm H} = 10^5$ cm^{-3}, $\log U = -3.5$). This density is close to the critical densities of both lines ($n_{\rm cr,[PII]} = 5.3\times10^4$ cm^{-3} and $n_{\rm cr,[FeII]} = 3.5\times10^4$ cm^{-3} for the gas with $T_{\rm e} = 10,000$ K; Koo et al. 2013), and together with the low ionization parameter, this condition seems plausible for emitting the [Fe II] and [P II] lines.

2.5 Conclusion

In order to investigate how the fast shock contributes to the NLR ionization, we have carried out near-infrared J-band spectroscopic observations of 26 nearby AGNs. In our analysis, we use the [Fe II]/[P II] flux ratio as a powerful diagnostics of the fast shock in the NLR. Among the 26 observed AGNs, the [P II] emission is significantly detected in 6 AGNs, while the [Fe II] emission is significantly detected in 19 AGNs. By adding the data from the literature, we gather the [Fe II]/[P II] flux ratio or its lower limit for 23 nearby AGNs. Based on this combined large sample of Seyfert galaxies, we obtain the following results and conclusions.

1. We find that the [Fe II]/[P II] flux ratio in more than half of Seyfert galaxies in our sample is consistent with the prediction by the photoionization model (~ 2). However, the three Seyfert galaxies, NGC 2782, NGC 5005, and Mrk 463, show very large [Fe II]/[P II]

flux ratios ($\gtrsim$ 10), suggesting a significant contribution of the fast shock in the NLR excitation.

2. The positive correlation between the [Fe II]/[P II] flux ratio and the [Fe II]/Paβ reported in the literature is confirmed in our large sample of Seyfert galaxies. This also supports the interpretation that the NLR in AGNs with a large [Fe II]/[P II] flux ratio is affected by fast shocks.

3. The positive correlation between the [Fe II]/[P II] flux ratio and the FWHM ratio of [Fe II] and [P II] is found in our sample. This is consistent with the interpretation that the observed [Fe II] flux in AGNs with a large [Fe II]/[P II] flux ratio is significantly attributed to shock-excited clouds.

4. The [Fe II]/[P II] flux ratio in our sample shows no clear correlation with the radio loudness or the strength of the starburst, suggesting that the radio jet and starburst are not the primary origins of the fast shocks in the NLR.

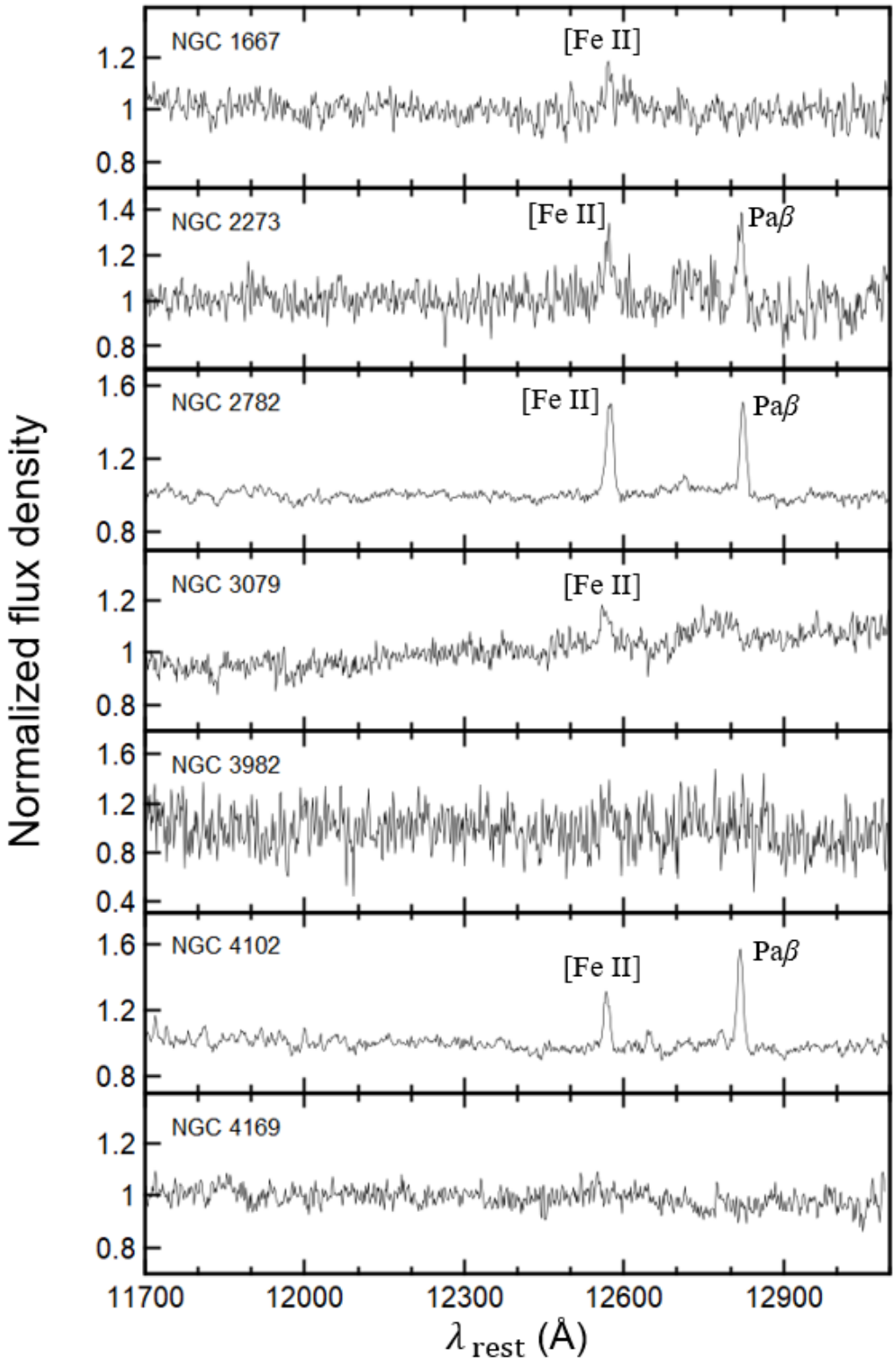

Fig. 2.1: Rest-frame J-band spectra of our sample galaxies. Flux density is normalized to the 1.235 μm continuum level.

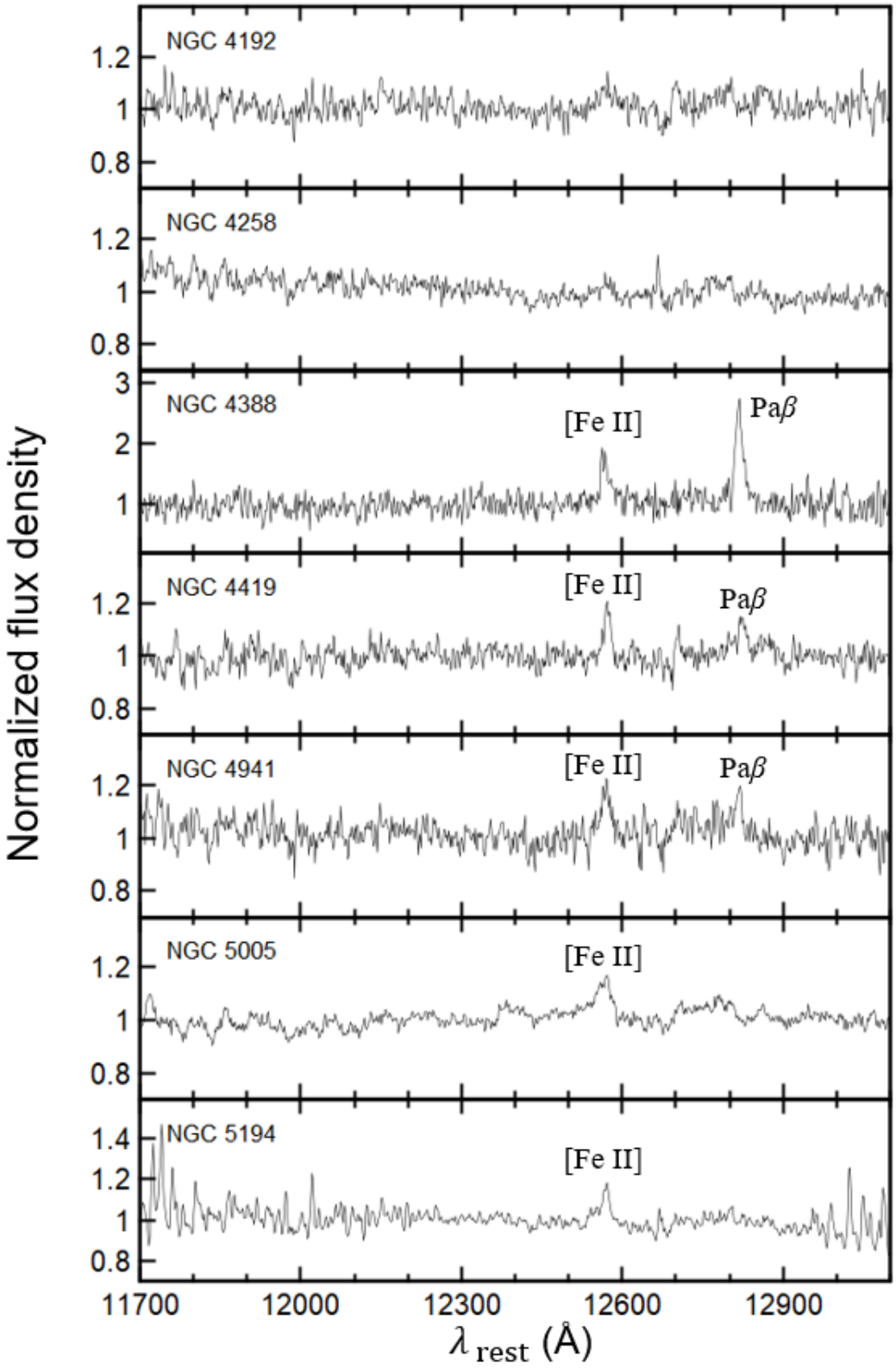

Fig. 2.1: (Continued.)

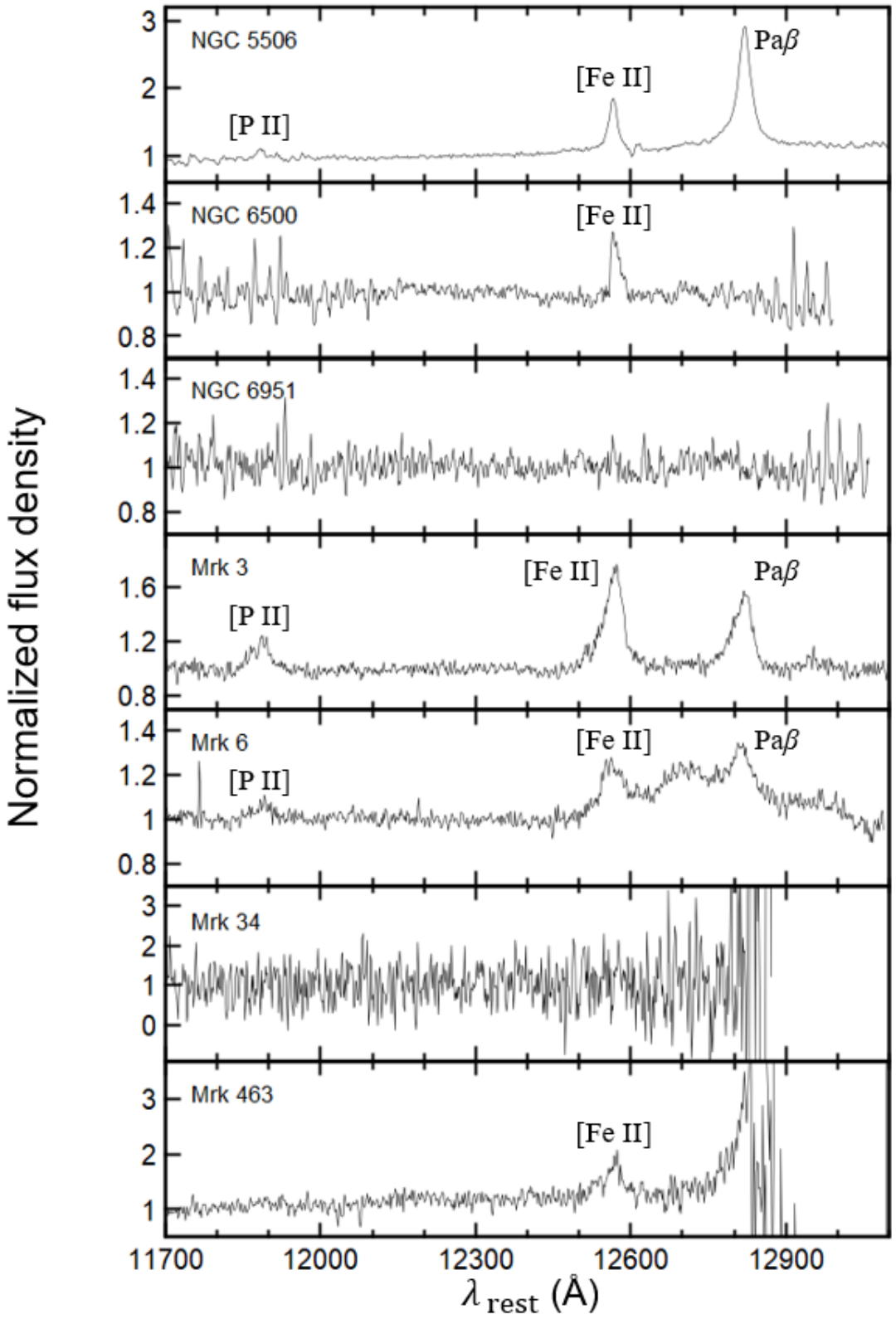

Fig. 2.1: (Continued.)

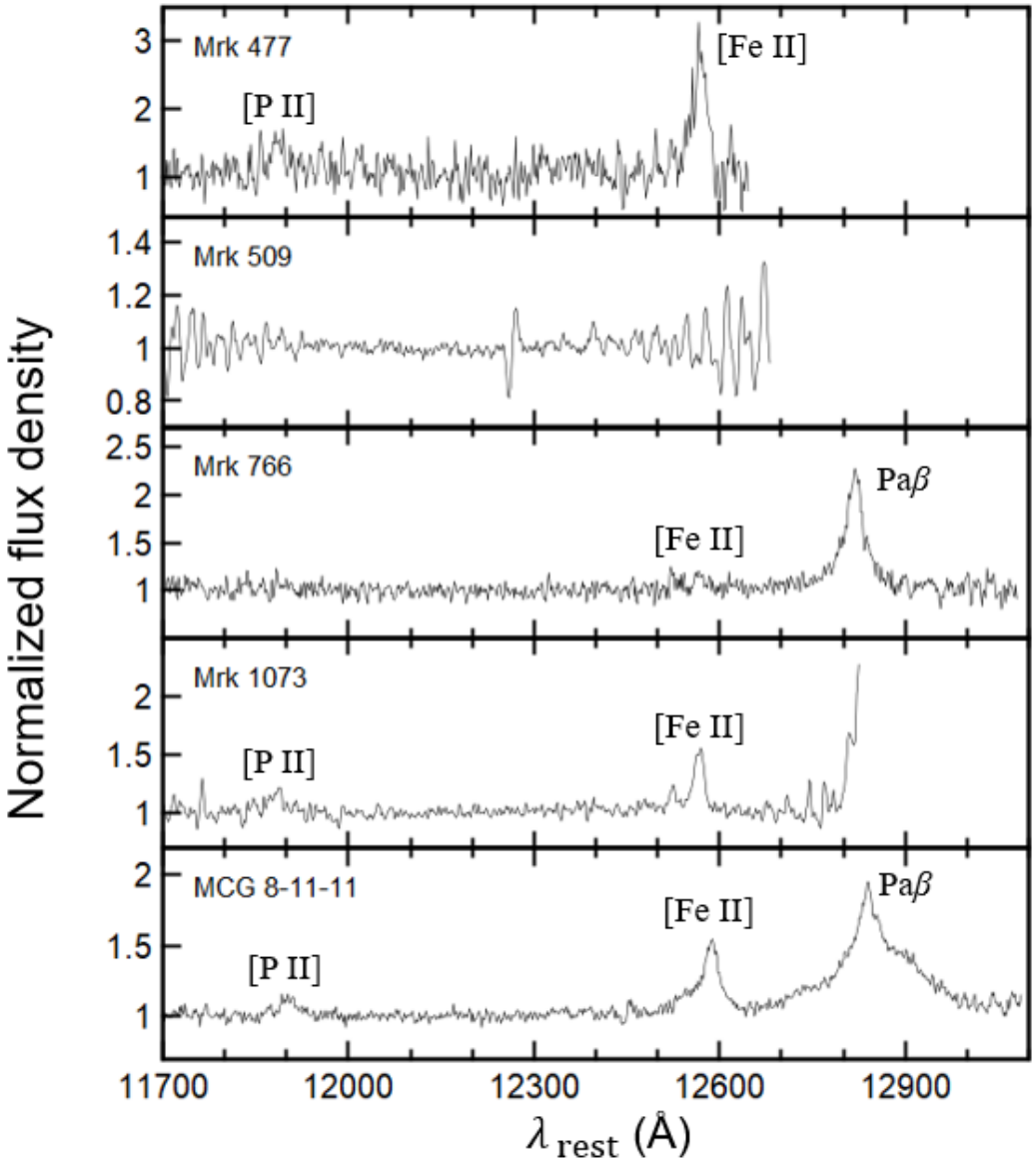

Fig. 2.1: (Continued.)

Table 2.2: Detected emission lines[a]

name	[P II] 1.188 μm		[Fe II] 1.257 μm		Paβ 1.282 μm[b]	
	λ_{obs}	FWHM	λ_{obs}	FWHM	λ_{obs}	FWHM
NGC 1667	–	–	1.2763	164	–	–
NGC 2273	–	–	1.2648	354	1.2897	258
NGC 2782	–	–	1.2681	300	1.2933	200
NGC 3079	–	–	1.2611	446	–	–
NGC 3982	–	–	–	–	–	–
NGC 4102	–	–	1.2603	229	1.2855	175
NGC 4169	–	–	–	–	–	–
NGC 4192	–	–	–	–	–	–
NGC 4258	–	–	–	–	–	–
NGC 4388	–	–	1.2566	511	1.2926	324
NGC 4419	–	–	1.2561	301	1.2812	511
NGC 4941	–	–	1.2616	475	1.2865	233
NGC 5005	–	–	1.2604	1251	–	–
NGC 5194	–	–	1.2587	548	–	–
NGC 5506	1.1957	340	1.2644	468	1.2900	808
NGC 6500	–	–	1.2696	474	–	–
NGC 6951	–	–	–	–	–	–
Mrk 3	1.2045	1050	1.2737	1091	1.2989	1072
Mrk 6	1.2113	1017	1.2797	1062	–[c]	–[c]
Mrk 34	–	–	–	–	–[d]	–[d]
Mrk 463	–	–	1.3199	1212	–[d]	–[d]
Mrk 477	1.2333	480	1.3042	691	–[d]	–[d]
Mrk 509	–	–	–	–	–[d]	–[d]
Mrk 766	–	–	1.2729	276	1.2984	888
Mrk 1073	1.2160	605	1.2859	470	–[d]	–[d]
MCG +08-11-011	1.2127	812	1.2821	957	–[c]	–[c]

[a]Observed central wavelength (μm) and FWHM (km s^{-1}) where the latter is corrected for instrumental broadening.
[b]Narrow component.
[c]Not measured due to complex spectral features.
[d]Not covered due to the insufficient spectral coverage of our observations.

Table 2.3: Emission-line flux ratios of the targets

Name	[Fe II]/[P II]	[Fe II]/Paβ
NGC 1667	> 3.174	> 3.064
NGC 2273	> 5.406	0.876 ± 0.086
NGC 2782	> 15.88	1.218 ± 0.019
NGC 3079	> 4.481	> 4.048
NGC 4102	> 7.427	0.627 ± 0.021
NGC 4388	> 5.896	0.614 ± 0.038
NGC 4419	> 4.067	1.242 ± 0.118
NGC 4941	> 4.880	1.525 ± 0.155
NGC 5005	> 12.37	> 12.31
NGC 5194	> 3.512	> 6.660
NGC 5506	6.876 ± 0.645	0.278 ± 0.003
NGC 6500	> 4.349	> 8.259
Mrk 3	3.974 ± 0.162	1.314 ± 0.023
Mrk 6	3.508 ± 0.245	– [a]
Mrk 463	> 17.46	– [b]
Mrk 477	4.330 ± 0.414	– [b]
Mrk 766	> 2.280	0.071 ± 0.007
Mrk 1073	2.460 ± 0.168	– [b]
MCG +08-11-011	4.256 ± 0.220	– [a]

3σ lower limits.

[a]Not measured due to complex spectral features.

[b]Paβ is out of the wavelength coverage in our observations.

Table 2.4: Emission-line flux ratios in the literature

Name	z[a]	[Fe II]/[P II]	[Fe II]/Paβ	Type[b]	Ref[c]
NGC 34	0.0196	1.55±0.43	1.07±0.14	Sy 2	1
NGC 1068	0.0038	1.33±0.06	0.46±0.02	Sy 2	2
NGC 1275	0.0176	3.35±0.12	1.05±0.06	Sy 1.5	1
NGC 2110	0.0078	5.61±1.07	5.45±0.32	Sy 2	1
NGC 3227	0.0039	2.80±0.61	1.21±0.08	Sy 1.5	1
NGC 4151	0.0033	2.98±0.21	0.54±0.03	Sy 1.5	1
NGC 5128	0.0018	3.0[d]	2.3[d]	FR I[e]	3
NGC 5929	0.0083	4.3±1.1	–[f]	LINER	4
NGC 7212	0.0266	3.64±0.42	0.86±0.05	Sy 2	5
NGC 7465	0.0065	>3.42[g]	1.28±0.34	LINER	5
NGC 7469	0.0163	1.76±0.27	0.39±0.03	Sy 1.5	1
NGC 7674	0.0289	1.90±0.19	1.04±0.11	Sy 2	1
Mrk 34	0.0505	3.2±1.0	–[f]	Sy 2	4
Mrk 78	0.0372	1.82±0.39	0.55±0.11	Sy 2	6
Mrk 79	0.0222	1.55±0.67	0.17±0.05	Sy 1	7
Mrk 334	0.0219	2.17±0.47	0.58±0.03	Sy 1.8	1
Mrk 348	0.0150	4.14±0.67	0.99±0.10	Sy 2	5
Mrk 573	0.0172	5.00±1.07	1.08±0.11	Sy 2	5
Mrk 766	0.0129	2.65±0.16	0.38±0.03	Sy 1	8
Mrk 1066	0.0120	2.74±0.24	0.79±0.03	Sy 2	5
Mrk 1157	0.0152	2.63±0.31	0.82±0.07	Sy 2	9
Ark 564	0.0247	2.07±0.40	0.09±0.01	LINER	1
ESO 428−G014	0.0057	1.99±0.11	0.67±0.02	Sy 2	1

[a]Redshift taken from the NASA/IPAC Extragalactic Database (NED).
[b]Activity classification is taken from Véron-Cetty & Véron (2010), unless a remark is given.
[c]References: (1) Riffel et al. (2006); (2) Hashimoto et al. (2011); (3) Krajnović et al. (2007); (4) Jackson & Beswick (2007); (5) Ramos Almeida et al. (2009); (6) Ramos Almeida et al. (2006); (7) Riffel et al. (2013); (8) Schönell et al. (2014); (9) Riffel & Storchi-Bergmann (2011).
[d]The error of the flux ratio is not given in the literature.
[e]Hardcastle et al. (2003).
[f]Not available in the literature.
[g]3σ lower limit.

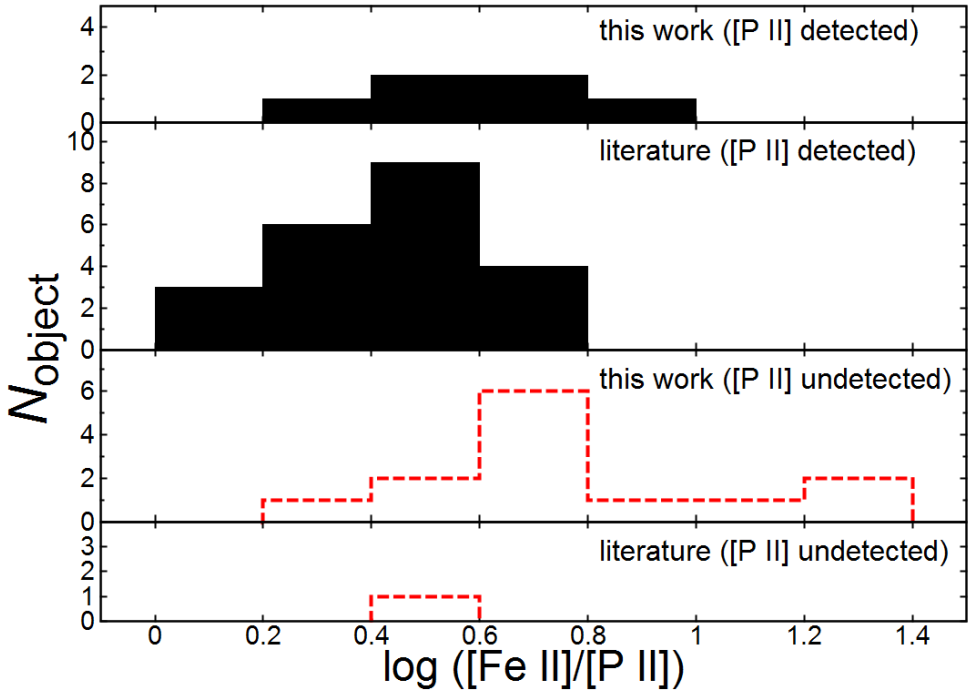

Fig. 2.2: Histograms for our sample and the compiled one. Filled black histograms denote data where [P II] is detected while red dashed histograms denote data with [P II] undetected one. The data for objects with [P II] detected in our OAO sample, objects with [P II] undetected in our OAO sample, objects with [P II] detected in the literature, and objects with [P II] undetected in the literature are shown from the top to the bottom panel. For objects with [P II] undetected, the 3σ lower limit of the [Fe II]/[P II] flux ratio is shown.

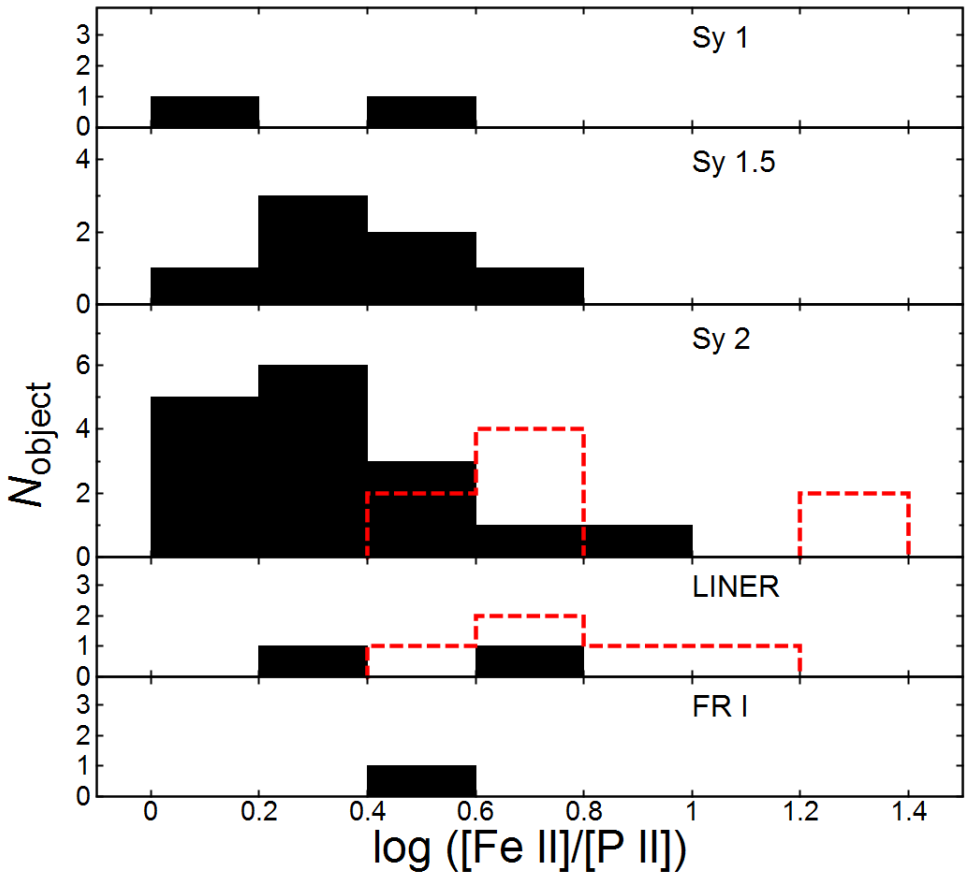

Fig. 2.3: Same as Figure 2.2 but for each AGN type. The type 1 Seyfert galaxies, type 1.5 Seyfert galaxies (including type 1.8 Seyfert galaxies), type 2 Seyfert galaxies, LINERs, and FR I radio galaxies, are shown from the top to the bottom panel, respectively. The filled black and red dashed histograms are the same as in Figure 2.2.

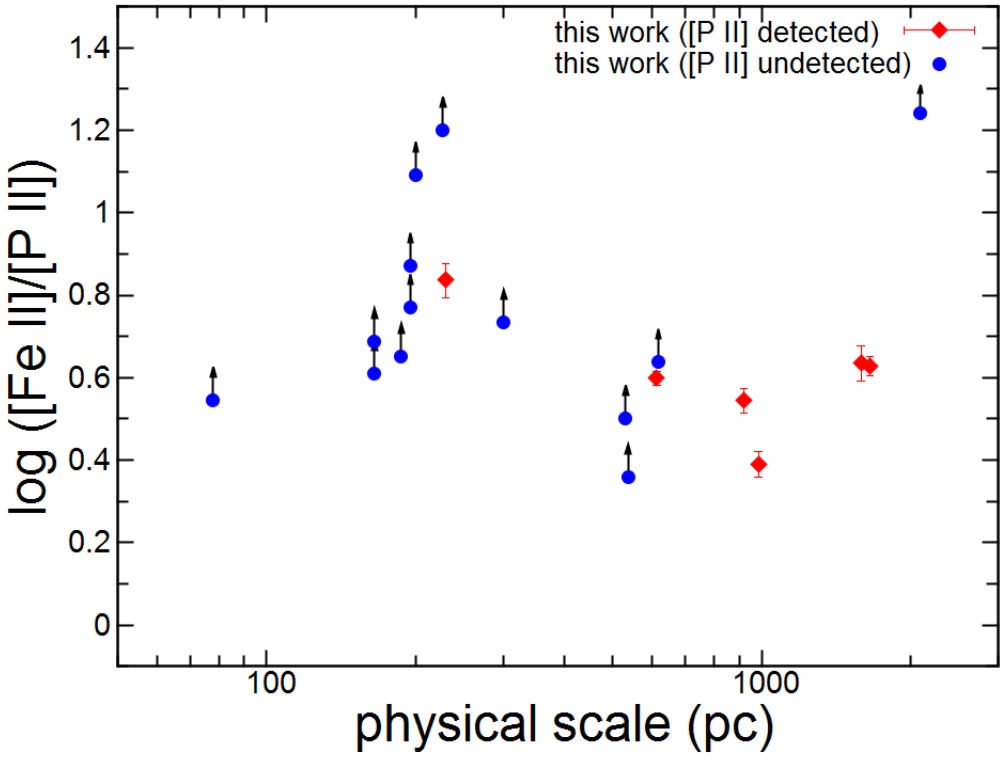

Fig. 2.4: Relation between the measured [Fe II]/[P II] flux ratio and the physical scale covered by the aperture size (= 2″.0) at the target redshift. Red diamonds and blue circles denote objects with [P II] detected and undetected in our OAO sample, respectively. For the objects with [P II] undetected, the 3σ lower limit of the [Fe II]/[P II] flux ratio is shown.

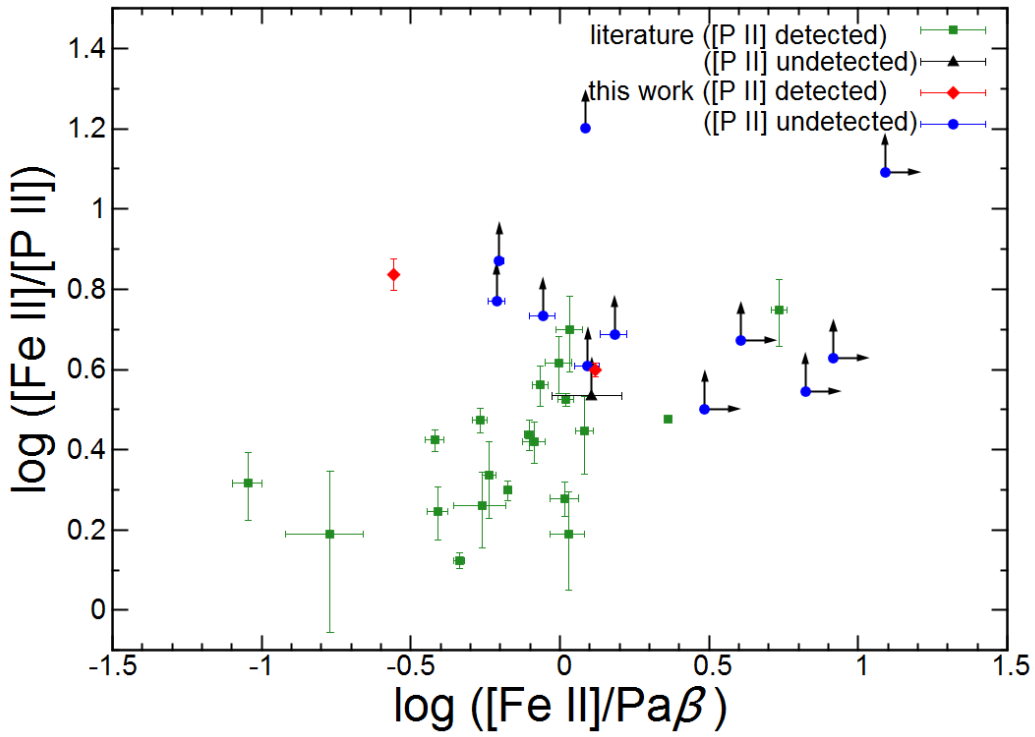

Fig. 2.5: Relation between the [Fe II]/[P II] and [Fe II]/Paβ flux ratios. Red diamonds and blue circles are the same as in Figure 2.4, while green squares and black triangles denote objects with [P II] detected and undetected in the sample from the literature. Arrows denote 3σ limits on the emission-line flux ratio.

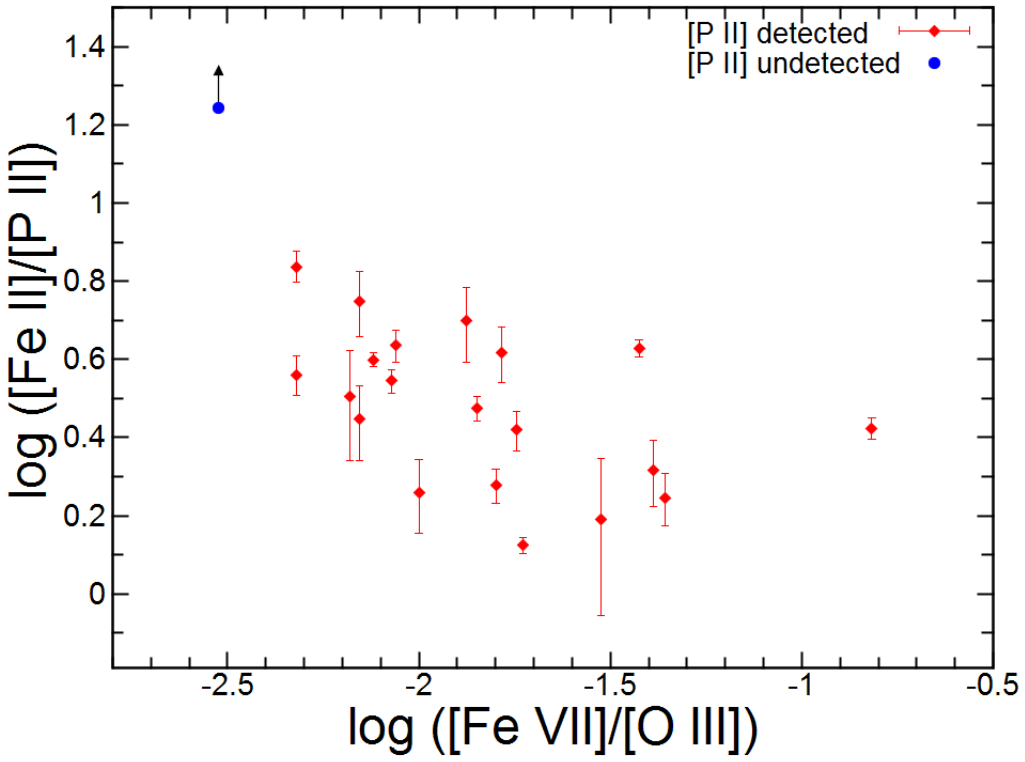

Fig. 2.6: Relation between the [Fe II]/[P II] and the [Fe VII]λ6087/[O III]λ5007 flux ratios. Red diamonds and blue circles denote objects with [P II] detected and undetected, respectively. Arrows denote 3σ limits on the emission-line flux ratio.

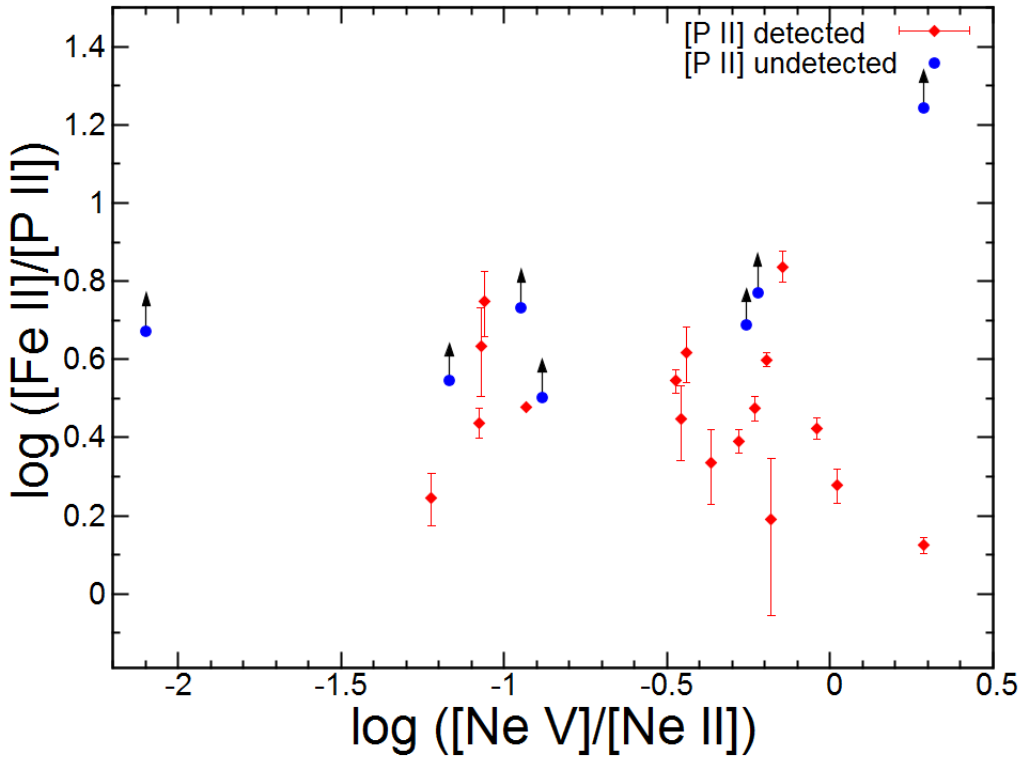

Fig. 2.7: Relation between the [Fe II]/[P II] and the [Ne V]14.32μm/[Ne II]12.81μm flux ratios. Symbols are the same as in Figure 2.6

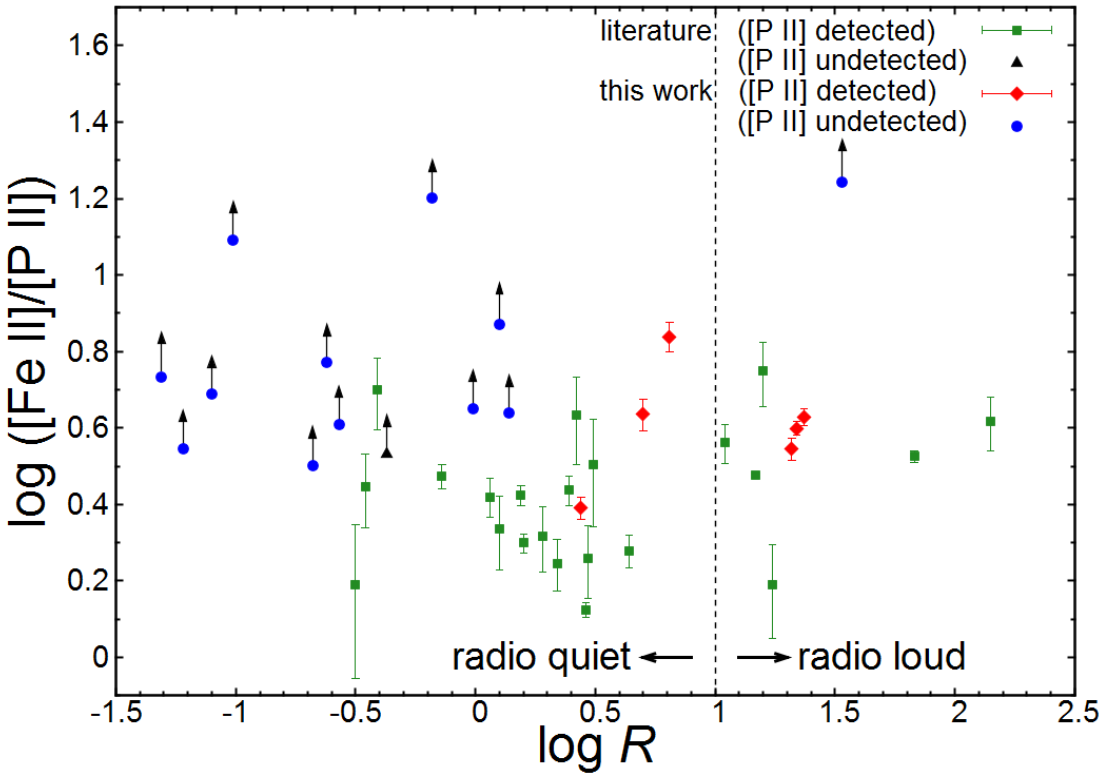

Fig. 2.8: Relation between the [Fe II]/[P II] flux ratio and the radio loudness (R). Symbols are the same as in Figure 2.5. Perpendicular dashed line shows the threshold dividing the radio-loud and radio-quiet populations.

Table 2.5: Various properties of our samples

Name	[Fe VII]/[O III]	Ref	[Ne V]/[Ne II]	Ref	$f_{5\mathrm{GHz}}$ (mJy)	Ref	f_{4400} (mJy)	Ref	log R	log L_{FIR} ($L_\odot$)	log $\nu L_\nu(K_\mathrm{s})$ ($L_\odot$)
objects observed at OAO											
NGC 1667	–		0.131	4	5.0	9	24.1±7.08	19	−0.68	10.55	10.38
NGC 2273	–		0.113	5	2.4	10	49.4±9.44	19	−1.31	10.00	10.05
NGC 2782	–		–		44.05	11	66.9±9.91	19	−0.18	9.89	9.65
NGC 3079	–		0.008	5	120.15	11	124±17.1	19	−0.01	10.47	10.12
NGC 3982	–		–		1.63	11	82.7±13.1	19	−1.71	9.80	9.59
NGC 4102	–		–		91.60	11	72.7±10.8	19	0.10	10.48	9.61
NGC 4169	–		–		0.59	11	23.0±4.14	19	−1.59	10.29	10.32
NGC 4192	–		–		6.88	11	222±21.4	19	−1.51	9.49	10.09
NGC 4258	–		–		2.43	11	819±121	19	−2.53	9.46	10.01
NGC 4388	–		0.600	5	18.46	11	76.1±5.82	19	−0.62	9.86	9.86
NGC 4419	–		–		16.20	11	60.5±4.62	19	−0.57	9.64	9.82
NGC 4941	–		0.554	5	4.92	11	61.6±14.5	19	−1.10	8.93	9.63
NGC 5005	–		–		18.78	11	191±30.4	19	−1.01	10.25	10.51
NGC 5194	–		0.068	5	6.04	11	994±147	19	−1.22	9.71	10.06
NGC 5506	0.0048	1	0.716	5	138.53	11	21.5±3.89	19	0.81	9.86	9.93
NGC 6500	–		–		35.8	10	25.7±4.91	19	0.14	9.86	10.40
NGC 6951	–		–		36±8	12	73.3±11.7	19	−0.31	10.17	10.19
Mrk 3	0.0076	1	0.640	5	355.59	13	16.2±2.75	19	1.34	10.33	10.47
Mrk 6	0.0085	1	0.336	5	98.5	13	4.76±0.76	19	1.32	10.12	10.59
Mrk 34	0.0066	1	–		7.91	11	2.56±0.71	20	0.49	10.73	10.49
Mrk 463	0.0030	2	1.935	5	150.81	11	4.42±0.85	19	1.53	11.14	11.09
Mrk 477	0.0087	1	–		24.28	11	4.89±1.35	20	0.70	10.75	10.07
Mrk 509	–		–		7.87±0.41	14	7.76±2.14	20	0.01	11.07	11.22
Mrk 766	0.1524	1	0.913	5	16.54	11	10.7±2.16	19	0.19	10.25	10.01
Mrk 1073	–		0.525	6	38.58±1.19	14	14.1±4.49	19	0.44	11.13	10.42
MCG +08-11-011	0.0376	1	–		100.90±3.57	14	4.26±0.86	21	1.37	11.13	11.26
objects from the literature											
NGC 34	–		–		44.39±5.79	15	2.58±0.01	22	1.24	11.24	10.28
NGC 1068	0.0187	1	1.941	5	1650.25	11	577±85.5	19	0.46	10.66	10.35
NGC 1275	–		–		3100±160	16	45.4±5.78	19	1.83	10.71	10.89
NGC 2110	0.0070	1	0.087	7	104.80±4.92	17	6.66±0.43	23	1.20	9.95	10.30
NGC 3227	0.0070	1	0.348	5	33.96	11	98.5±16.7	19	−0.46	9.85	10.08
NGC 4151	0.0142	1	0.588	5	135.83	11	186±27.6	19	−0.14	9.30	9.80
NGC 5128	–		0.117	5	52662±2662	18	3540±756	19	1.17	9.65	10.04
NGC 5929	–		0.085	5	28.95	11	10.92±0.29	24	0.42	10.35	10.05
NGC 7212	0.0048	3	–		42.29	11	3.89±1.73	25	1.04	10.84	10.51
NGC 7465	–		–		8.53±0.57	14	20.2±3.86	19	−0.37	9.61	9.51
NGC 7469	0.0440	1	0.060	5	59.73	11	27.4±3.77	19	0.34	11.27	10.58
NGC 7674	0.0159	1	1.050	5	72.48	11	16.7±3.18	19	0.64	10.78	10.37
Mrk 34	0.0066	1	–		7.91	11	2.56±0.71	20	0.49	10.73	10.49
Mrk 78	0.0100	1	–		17.37±3.86	15	5.88±1.63	20	0.47	10.62	10.38
Mrk 79	0.0299	1	0.660	5	6.09	11	19.3±3.69	19	−0.50	10.64	10.80
Mrk 334	–		0.433	4	9.65±3.86	15	7.68±1.38	19	0.10	10.82	10.36
Mrk 348	0.0165	1	0.363	5	801.7	9	5.72±1.16	19	2.15	9.99	10.07
Mrk 573	0.0133	1	–		5.64	11	14.4±2.13	19	−0.41	9.99	10.05
Mrk 766	0.1524	1	0.913	5	16.54	11	10.7±2.16	19	0.19	10.25	10.01
Mrk 1066	–		0.084	8	36.67±3.86	15	14.9±2.21	19	0.39	10.62	9.97
Mrk 1157	0.0180	1	–		13.65±0.45	14	11.8±2.14	19	0.06	10.17	10.08
Ark 564	0.041	1	–		11.93±0.41	14	6.26±1.48	19	0.28	10.23	10.22
ESO 428-G014	–		–		33.50±1.23	14	21.2±4.51	19	0.20	9.57	9.68

References: (1) Nagao et al. 2000; (2) Nagao et al. 2003; (3) Bennert et al. 2006b; (4) Wu et al. 2011; (5) Pereira-Santaella et al. 2010; (6) Petric et al. 2011; (7) Weaver et al. 2010; (8) Dasyra et al. 2011; (9) Gallimore et al. 2006; (10) 1.4 GHz data from Nagar et al. 2005; (11) FIRST catalog (*Faint Images of the Radio Sky at Twenty-cm*); (12) Sramek 1975; (13) 4.89 GHz data from Laurent-Muehleisen et al. 1997; (14) 1.4 GHz data from Condon et al. 1998; (15) Bicay et al. 1995; (16) Taylor et al. 2006; (17) 4.89 GHz data from Ulvestad & Wilson 1984; (18) 4.85 GHz data from Gregory et al. 1994; (19) de Vaucouleurs et al. 1991, RC3 (*Third Reference Catalog of Bright Galaxies*), photographic magnitude; (20) 4680 Å data from Petrosian et al. 2007; (21) de Vaucouleurs et al. 1991 (RC3), total magnitude; (22) Schweizer & Seitzer 2007; (23) 4480 Å data from McAlary et al. 1983; (24) SDSS, *g*-band (4860 Å); (25) Zwicky & Kowal 1968, CGCG (*Catalogue of Galaxies and Clusters of Galaxies*).

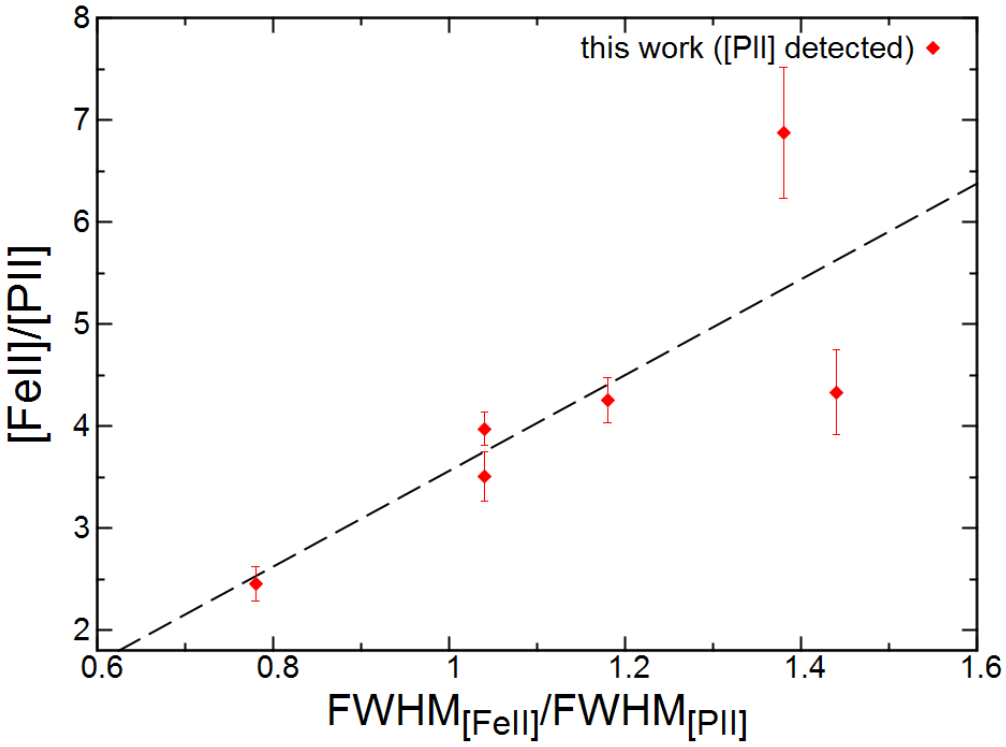

Fig. 2.9: Relation between the [Fe II]/[P II] flux ratio and the FWHM ratio of [Fe II] and [P II] for objects whose [Fe II] and [P II] are detected in our OAO run. The dashed line represents the linear-fit result.

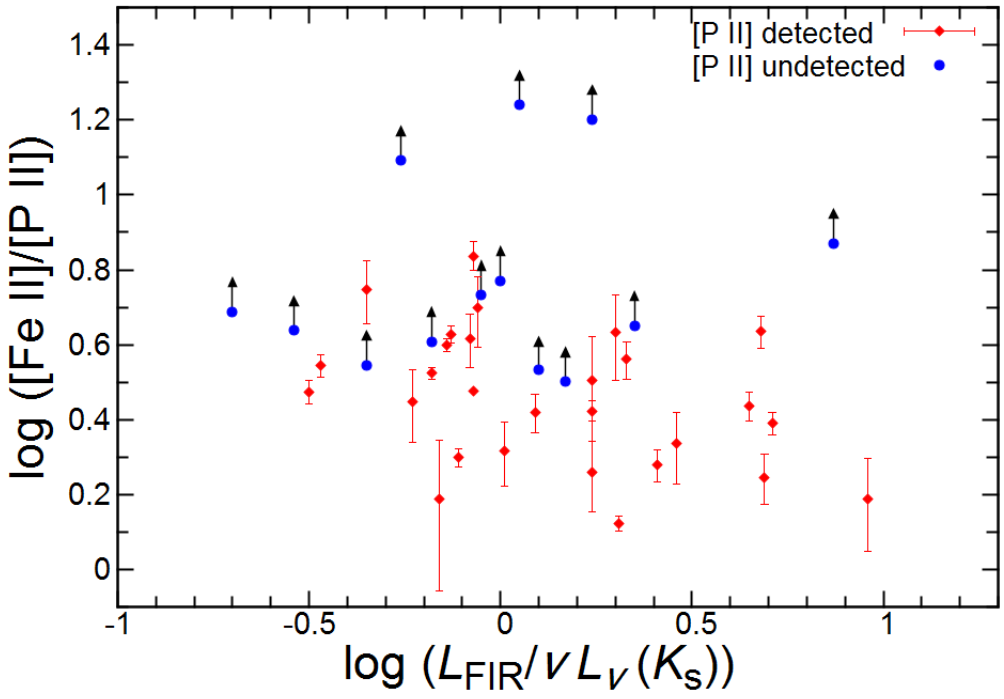

Fig. 2.10: Relation between the [Fe II]/[P II] flux ratio and the far-infrared luminosity normalized to the K_s luminosity. Symbols are the same as in Figure 2.6.

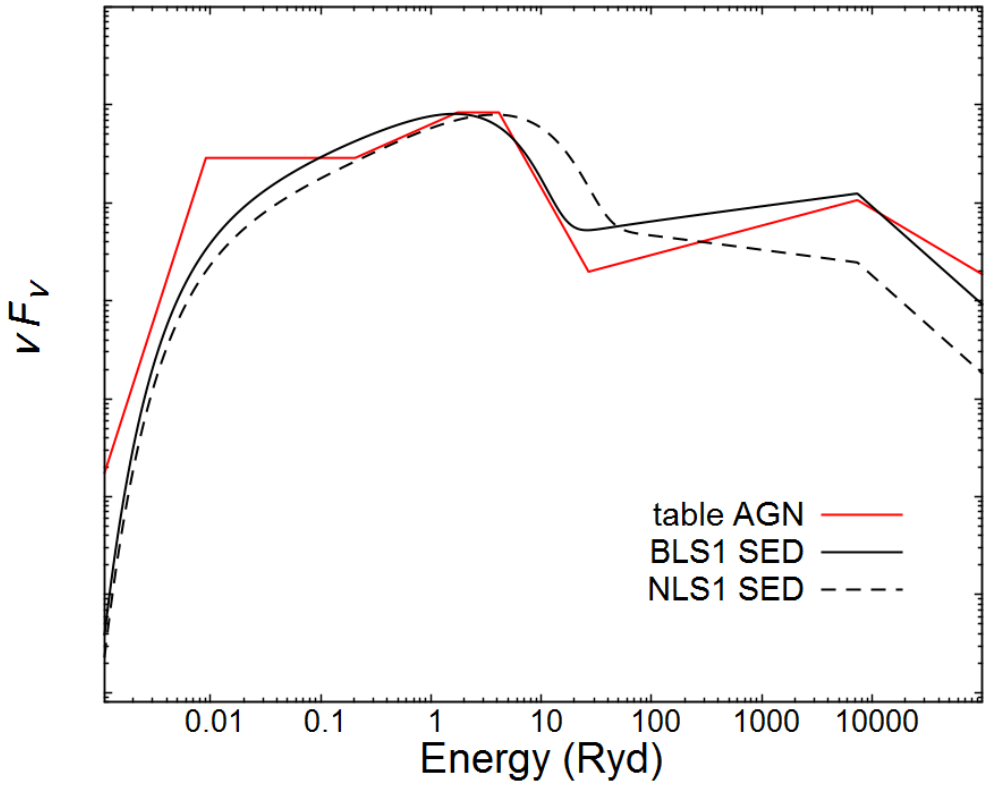

Fig. 2.11: The spectra of each incident continuum. The solid-red, solid-black, and dashed black lines denote the table AGN, BLS1, and NLS1 SED, respectively.

Table 2.6: Depletion factor adopted in our model calculations

	Depletion
He	1.0
Li	0.16
Be	0.6
B	0.13
C	0.4
N	1.0
O	0.6
F	0.3
Ne	1.0
Na	0.2
Mg	0.2
Al	0.01
Si	0.03
P	0.25
S	1.0
Cl	0.4
Ar	1.0
K	0.3
Ca	1×10^{-4}
Sc	5×10^{-3}
Ti	8×10^{-3}
V	6×10^{-3}
Cr	6×10^{-3}
Mn	0.05
Fe	0.01
Co	0.01
Ni	0.01
Cu	0.1
Zn	0.25

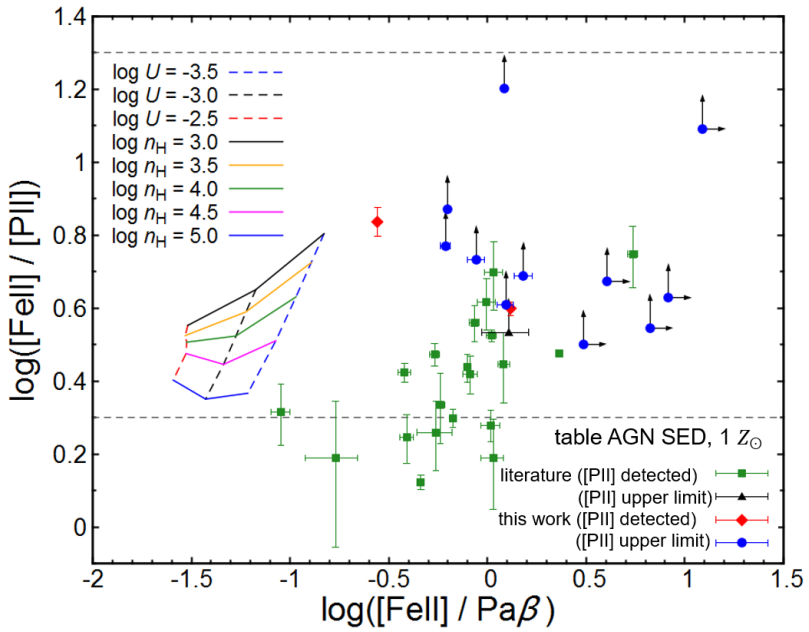

Fig. 2.12: The [Fe II]/[P II] versus [Fe II]/Paβ diagram with model grid in case of table AGN SED and 1 $Z_\odot$. The plots are same as Figure 2.5. The dashed and solid lines denote constant of ionization parameter and density, respectively. The two horizontal dashed lines show the typical values of [Fe II]/[P II] in shock-dominated (upper one) and photoionized-dominated (lower one) clouds, respectively.

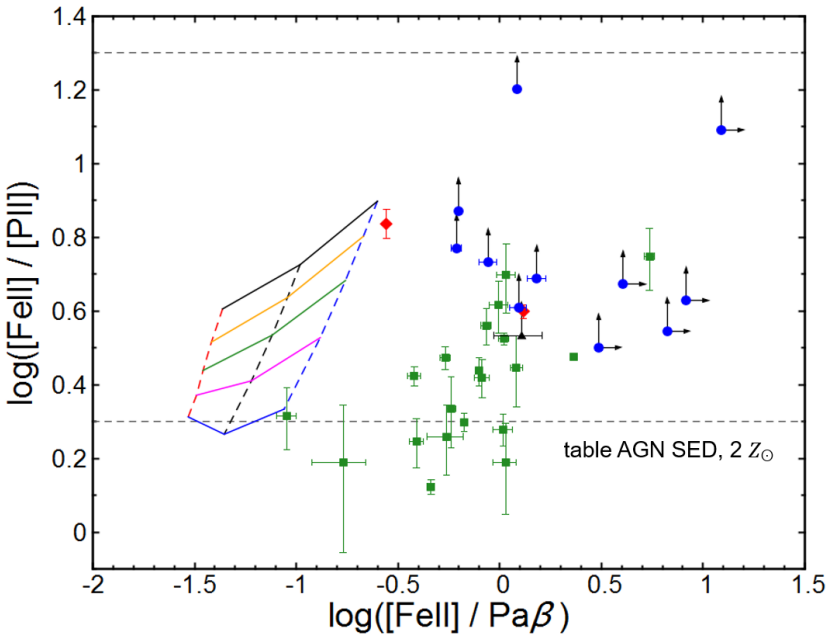

Fig. 2.13: Same as Figure 2.12 but for model grid in case of table AGN SED and 2 $Z_\odot$.

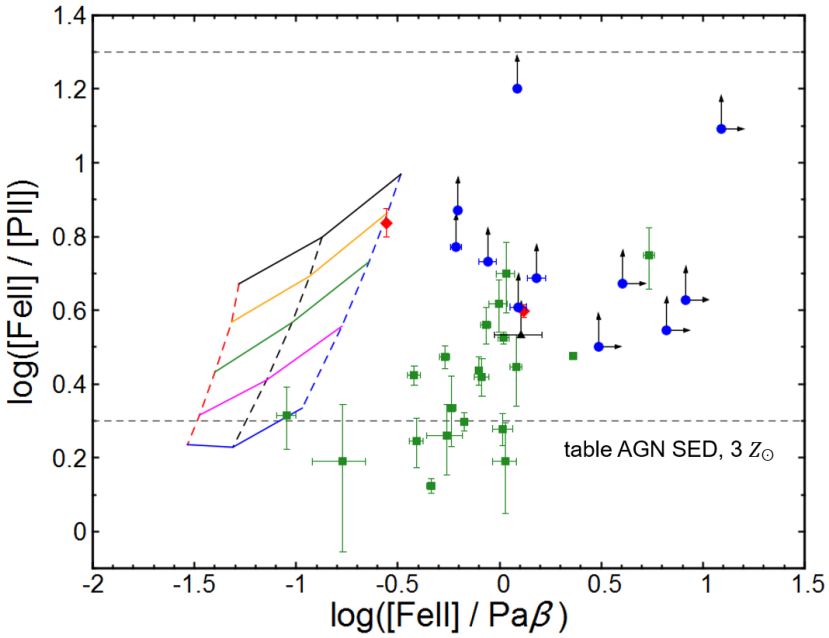

Fig. 2.14: Same as Figure 2.12 but for model grid in case of table AGN SED and 3 $Z_\odot$.

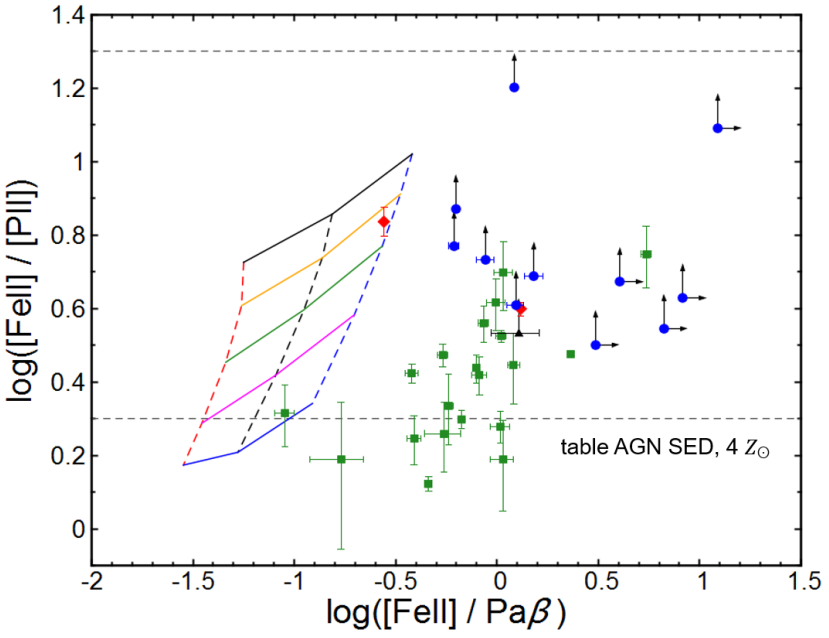

Fig. 2.15: Same as Figure 2.12 but for model grid in case of table AGN SED and 4 $Z_\odot$.

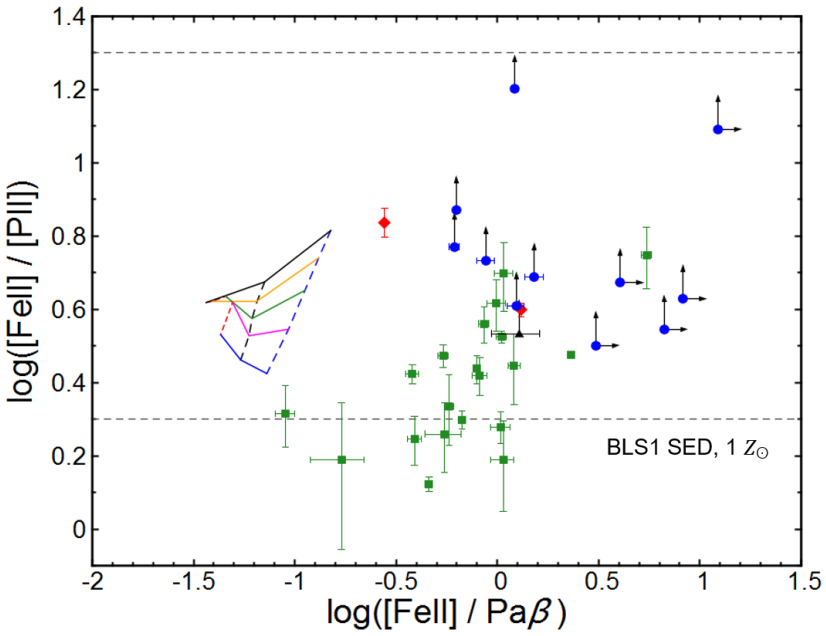

Fig. 2.16: Same as Figure 2.12 but for model grid in case of BLS1 SED and 1 $Z_{\odot}$.

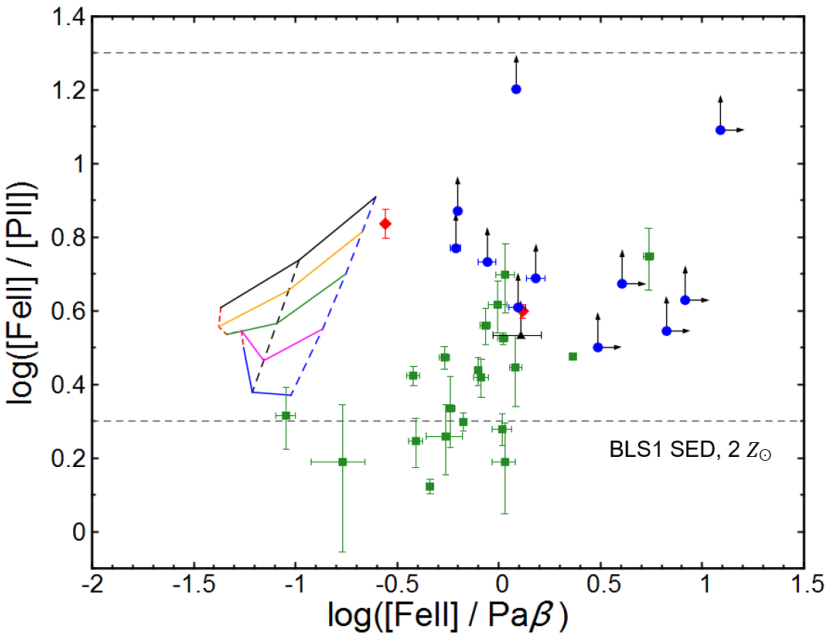

Fig. 2.17: Same as Figure 2.12 but for model grid in case of BLS1 SED and 2 $Z_{\odot}$.

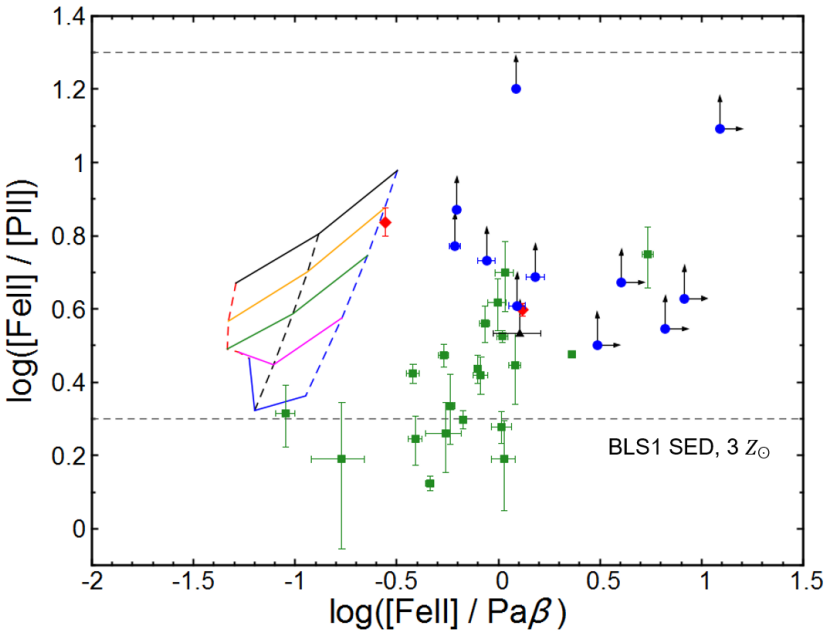

Fig. 2.18: Same as Figure 2.12 but for model grid in case of BLS1 SED and 3 $Z_\odot$.

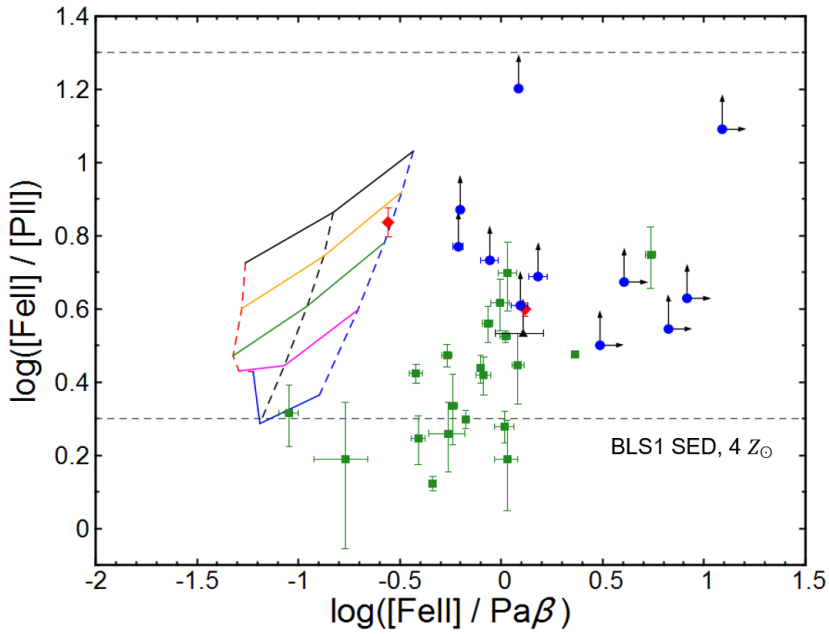

Fig. 2.19: Same as Figure 2.12 but for model grid in case of BLS1 SED and 4 $Z_\odot$.

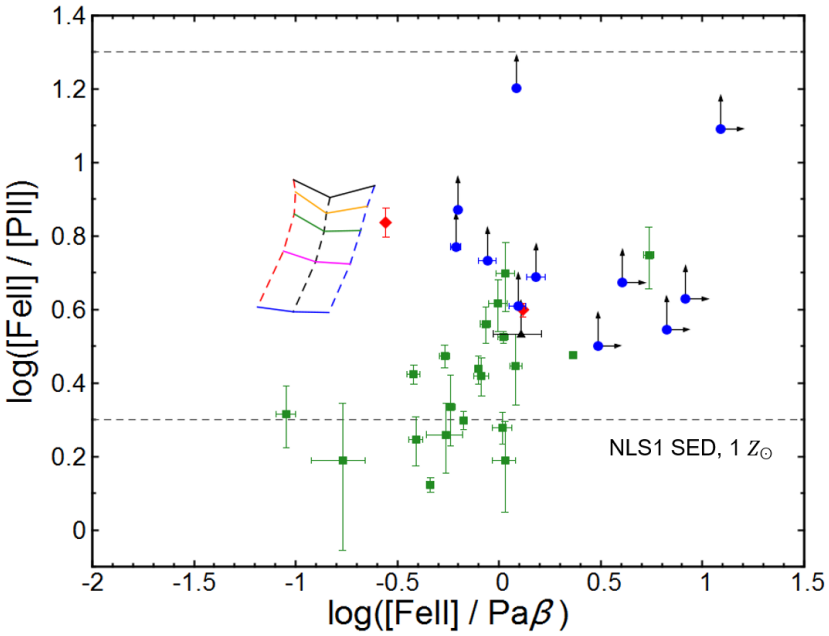

Fig. 2.20: Same as Figure 2.12 but for model grid in case of NLS1 SED and 1 $Z_\odot$.

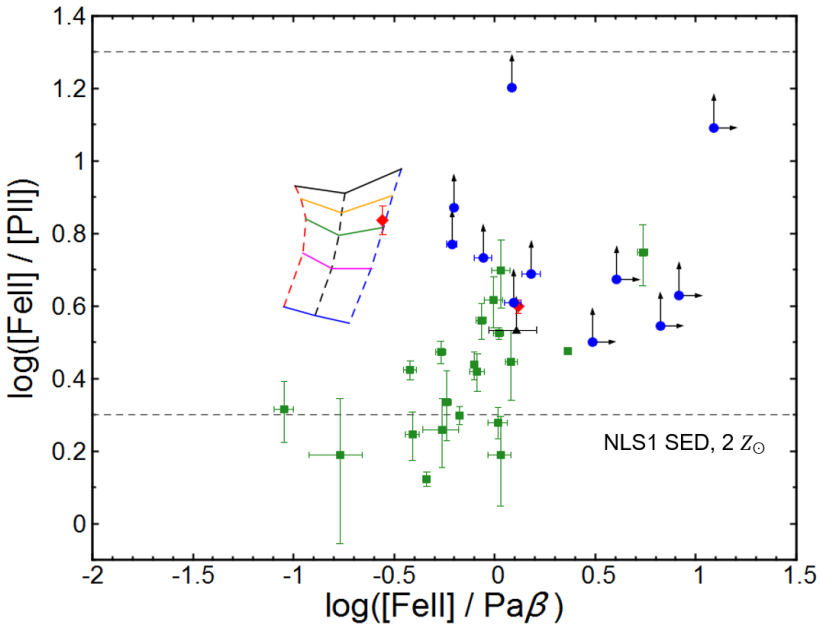

Fig. 2.21: Same as Figure 2.12 but for model grid in case of NLS1 SED and 2 $Z_\odot$.

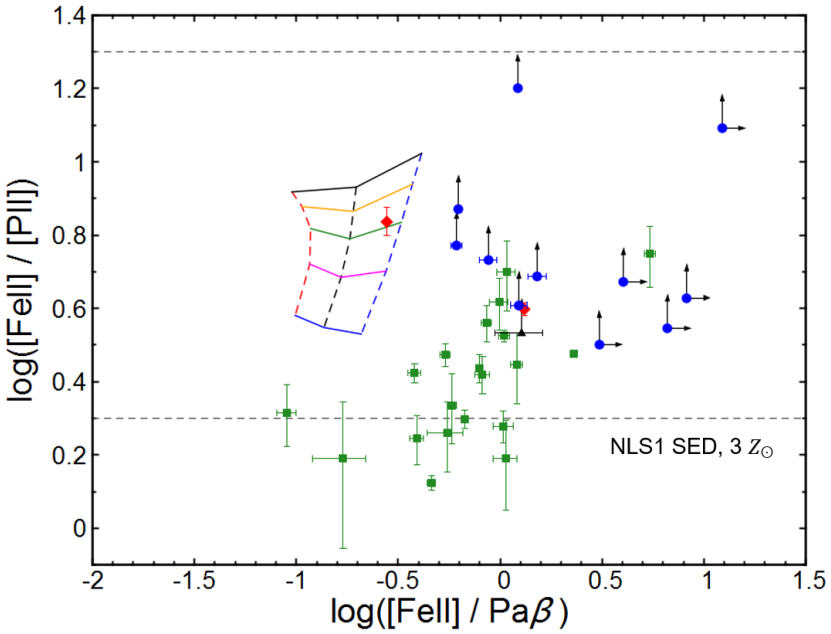

Fig. 2.22: Same as Figure 2.12 but for model grid in case of NLS1 SED and 3 $Z_\odot$.

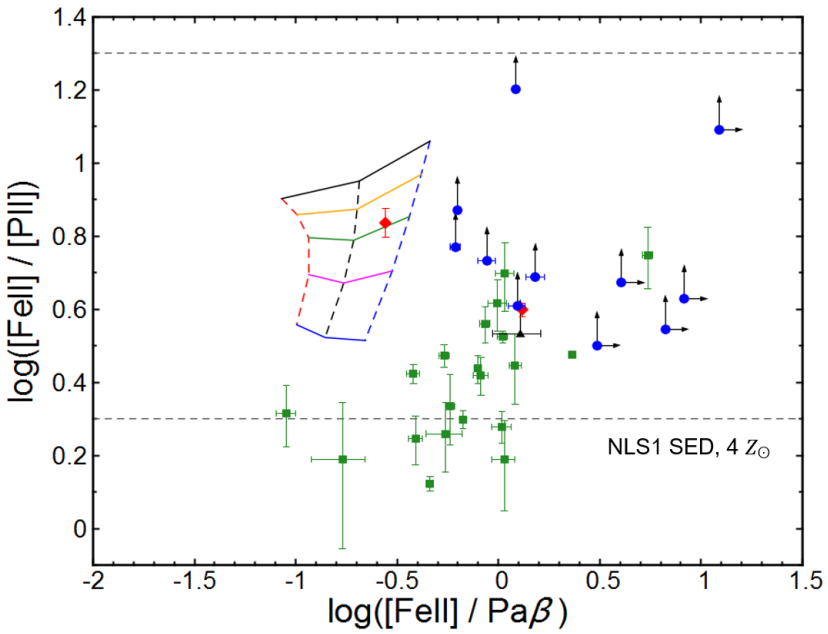

Fig. 2.23: Same as Figure 2.12 but for model grid in case of NLS1 SED and 4 $Z_\odot$.

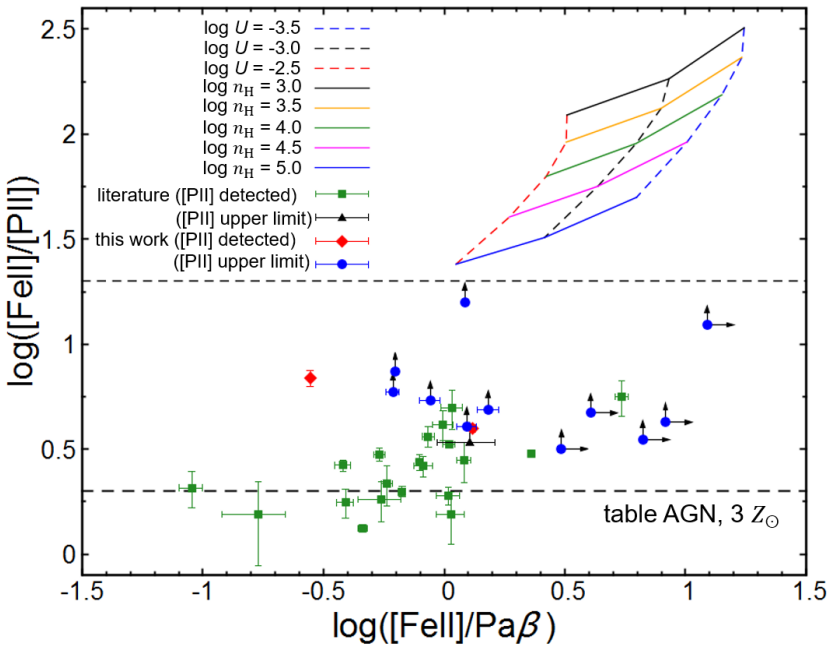

Fig. 2.24: Same as Figure 2.12 but for model grid of table AGN SED and 3 $Z_\odot$ without depletion factor. In this case, the model grids can be reproduce the [Fe II]/Paβ, however the [Fe II]/[P II] plots are out of model grids.

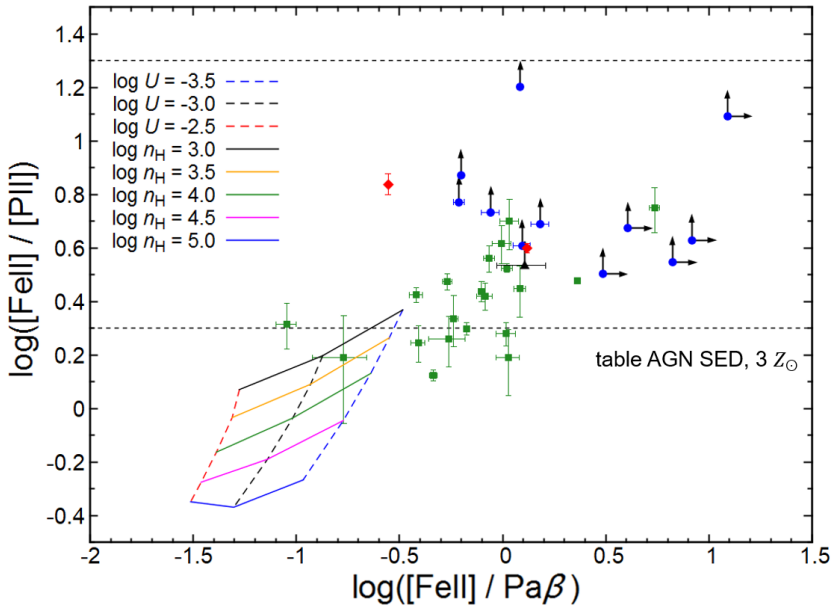

Fig. 2.25: Same as Figure 2.12 but for model grid of table AGN SED and 3 $Z_\odot$ without depletion factor for P.

CHAPTER 3

THE PHYSICAL AND CHEMICAL PROPERTIES OF ISM IN HIGH-z RADIO GALAXIES

Physical and chemical properties of narrow-line regions (NLRs) in high-z active galactic nuclei (AGNs) have been investigated mostly by using only strong rest-UV emission-lines. Such strong-line diagnostics require various assumptions due to the limited number of available emission lines. In this chapter, we present high-quality rest-UV spectra of three radio galaxies at $z \sim 3$ observed with VLT/FORS2 for attempting to measure the flux of several emission lines including relatively faint ones, such as N IV]λ1486, O III]λ1663, and [Ne IV]λ2424. In addition, we collect fluxes of faint UV emission lines in 12 $z \sim 3$ radio galaxies from the literature. We diagnose the physical and chemical properties of NLR clouds in each object through the comparison between the measured emission-line fluxes and detailed photoionization models with Cloudy. We confirm that the metallicity of NLRs in AGNs at $z \sim 3$ is solar or super-solar metallicity, without assuming the gas density and ionization parameter thanks to the newly detected faint emission lines. The inferred gas density and ionization parameter tend to be higher than those seen in NLRs of low-z AGNs. These results suggest that (1) high-z radio galaxies are already chemically matured at $z \sim 3$, and (2) ISM properties of host galaxies of AGNs are systematically different between low-z and high-z Universe.

3.1 Introduction

It is one of the hottest topics in modern astronomy to understand the formation and evolution of galaxies. For this purpose, investigating the nature of various ingredients of galaxies such as stars, gas, and dark matter at various cosmic epochs is a fundamental approach. Especially, it is clearly important to understand the redshift evolution of interstellar medium (ISM) properties that are characterized by physical and chemical parameters such as the gas density, ionization parameter, and metallicity. In particular, the metallicity is an indicator of the star-formation

history and gas inflow/outflow history of galaxies (e.g., Erb, 2008; Lilly et al., 2013; Lu et al., 2015; Belfiore et al., 2016; Vangioni et al., 2018). For low-redshift galaxies, optical emission-line diagnostics are commonly used for measuring the ISM properties in local Universe (e.g., Izotov et al., 2006; Nagao et al., 2006a; Kewley & Ellison, 2008; Curti et al., 2017). In high-z Universe, those rest-frame optical emission lines are shifted into near-infrared and thus observations are more challenging. Recently, the ISM properties of such high-z star-forming galaxies have been also investigated (e.g., Förster Schreiber et al., 2009; Yabe et al., 2012; Yuan et al., 2013; Maier et al., 2014; Newman et al., 2014; Nakajima et al., 2018) and show the evolution of ISM properties that are consistent to predictions by some theoretical models (e.g., Kewley et al., 2013). However, the determination of detail physical parameters for high-redshift star-forming galaxies is generally difficult because they are faint.

On the other hand, active galactic nuclei (AGNs) are very luminous and thus their emission-line flux ratios can be measured even in high-z Universe. One significant advantage of the spectroscopic study for AGNs with respect to star-forming galaxies is that AGNs show some rest-frame UV strong emission lines which are very faint in star-forming galaxies. Therefore many spectroscopic observations for high-z AGNs have been carried out for various diagnostic studies (e.g., Villar-Martín et al., 1999; De Breuck et al., 2000; Vernet et al., 2001; Solórzano-Iñarrea et al., 2004; Nagao et al., 2006b; Humphrey et al., 2008; Matsuoka et al., 2011a; Feltre et al., 2016). In particular, spectroscopic properties of narrow-line regions (NLRs) in AGNs have been often investigated because NLR gas clouds distribute at $\sim$kpc scale that is comparable to the spatial scale of host galaxies. Since NLR clouds are mostly ionized through the photoionization process (e.g., Binette et al., 1996; Komossa & Schulz, 1997; Groves et al., 2004; Thomas et al., 2016), ISM properties of host galaxies can be studied through detailed comparisons between photoionization models and emission-line spectra of NLRs.

For studying spectroscopic properties of NLRs in AGNs, it is convenient to focus on type 2 AGNs. This is because the strong broad-line emission from broad-line regions (BLRs) is blocked by optically-thick dusty tori, and thus both of forbidden and permitted emission lines can be used for various diagnostic studies without affected by the BLR emission. Among some populations of type 2 AGNs, high-z radio galaxies (HzRGs) have been targeted in high-z spectroscopic studies because their discovery is relatively easier than radio-quiet type 2 AGNs in high-redshift Universe. In previous spectroscopic studies of HzRGs, strong UV lines (such as N Vλ1240, C IVλ1549, He IIλ1640, and C III]λ1909) have been used for diagnostic studies so far (e.g., Nagao et al., 2006b; Villar-Martín et al., 2007; Humphrey et al., 2008; Matsuoka et al., 2009; Dors et al., 2014; Morais et al., 2017; Matsuoka et al., 2018a). These results suggest that the host galaxies of HzRGs had already chemically evolved in $z \sim 4$ without significant redshift evolution in $1 < z < 4$.

In previous studies, however, emission-line diagnostic studies have required strong assumptions on some ISM parameters; in other words, it has been difficult to determine various ISM parameters simultaneously because of the small number of detected emission lines. In this chapter, we focus on deep rest-UV spectra of HzRGs to measure the flux of several emission lines including relatively faint ones. We investigate the physical and chemical properties of the

ISM in host galaxies of HzRGs without assuming many ISM parameters for diagnostic studies by utilizing a large number of rest-frame UV emission lines. In Section 3.2, we describe the data and reductions. We show the results in Section 3.3 and describe our photoionization models in Section 3.4. We discuss the interpretation of our results in Section 3.5 and draw the conclusion of this chapter in section 3.6. Throughout this chapter, we assume $\Omega_{\rm M}$ =0.3, Ω_{Λ}=0.7, and H_0 =70 km s^{-1} Mpc^{-1}.

3.2 Data

3.2.1 Our targets and data reduction

We focus on high-sensitivity rest-UV spectra of three HzRGs (TN J0920−0712, 4C 24.28, and USS 1545−234), that are taken from 9 HzRGs investigated by Matsuoka et al. (2009). Those three HzRGs are selected in this study because the spectra of the three HzRGs show very high signal-to-noise ratios, resulting in the detection of many emission lines including relatively faint ones. These 9 HzRGs were originally selected from a HzRG catalog (De Breuck et al., 2000) with the criteria that (1) their redshift should be higher than 2.7, and (2) their emission-line fluxes of C IV, He II, and C III] have not yet been measured so far. Basic properties of these three objects are summarized in Table 3.1. The observations were carried out using FORS2 (FOcal Reducer and low dispersion Spectrograph 2; Appenzeller et al. 1998) at VLT (Very Large Telescope) between 2005 October and 2006 October (PI: Tohru Nagao; the details of the observations are described in Matsuoka et al. 2009). The spectral resolution is $R \sim 500$, which was measured using the width of sky emission lines. The typical seeing during observations was $\sim 1''.4$.

Table 3.1: Target properties

Name	z^a	$E(B-V)^b$	Exp. (min)	Date of observations
TN J0920−0712	2.758	0.041	180	2006 Apr. 3, 4
4C 24.28	2.913	0.018	180	2006 Apr. 23
USS 1545−234	2.751	0.257	240	2006 Apr. 5, 23, 24

[a]Redshifts are determined from the observed C IV wavelength.
[b]Galactic extinction (Schlegel et al., 1998).

The data reduction of the three objects were described in Matsuoka et al. (2009). The data analysis was performed by using the IRAF software (Tody, 1986, 1993) i.e., bias subtraction using average bias frames, flat fielding, cosmic ray subtraction, wavelength calibration using sky emission-lines, sky subtraction, spectral extraction from two-dimensional spectra by adopting $2''.25$ (9 pixels) aperture, and flux calibration by standard stars. The Galactic reddening maps from Schlegel et al. (1998) and extinction law from Cardelli et al. (1989) were adopted for correcting of the Galactic reddening of the three targets. Here we focus on the relatively faint emission-lines, thus we reanalyzed the spectra with additional procedure. In particular, sky

subtractions were performed carefully to remove noises from the spectra. Cosmic-ray events were removed using the "lacos_spec" task (van Dokkum, 2001). The spectra of targets were divided by the spectra of standard stars to correct for atmospheric absorption features.

In many cases, fluxes of emission lines from NLRs are affected by the dust reddening caused in their host galaxies, not only in the Galaxy. The Balmer decrement is mostly used to correct for such internal reddening. However, it is not straightforward to estimate the amount of the reddening for HzRGs in our sample, since reddening indicators such as the Balmer decrement are not available. In this work, we did not correct for such internal extinction because of the following consideration. For low-redshift radio galaxies, Robinson et al. (1987) investigated the Balmer decrement of 11 radio galaxies at $z < 0.1$ and showed that extended emission-line regions of more than half of their targets show the Case B flux ratio (i.e., $A_V \sim 0$ mag). For HzRGs, Humphrey et al. (2008) investigated flux ratios of Hα/Hβ and/or He IIλ1630/He IIλ4686 of 11 HzRGs, and reported that more than half of them show a low extinction ($A_V < 0.5$ mag). These results are consistent with the idea that radio galaxies are gas-poor and thus dust is not abundant. Therefore we assume that the internal dust extinction is negligible for our HzRG sample.

3.2.2 Additional rest-UV data from the literature

In addition to the re-analyzed data, we collected 12 rest-UV spectra of HzRGs that show various rest-UV emission lines including relatively faint ones. The emission-line data of 10 $z \sim 3$ HzRGs are obtained from Vernet et al. (2001) and Humphrey et al. (2008). These targets were selected from ultra-steep spectrum (USS) radio galaxy survey (Rottgering et al., 1995) for $z > 2.2$ and $R \sim 21 - 23$ mag. These spectra were observed with the LRISp (the spectro-polarimetric mode of Low-Resolution Imaging Spectrometer; Goodrich et al. 1995; Oke et al. 1995) at the Keck II 10 m telescope. Another spectrum of a $z \sim 2$ HzRG (NVSS J002402−325253) obtained with the FORS1 at VLT is collected from De Breuck et al. (2006). This target had been selected from a USS radio galaxy sample (De Breuck et al., 2004). The other spectrum is 3C 256 ($z = 1.824$) which was observed with the double spectrograph (Oke & Gunn, 1982) at the Hale 5 m telescope (Simpson et al., 1999).

For low-z objects, it is generally difficult to obtain sensitive rest-UV spectra because the UV emission cannot be observed from ground-based telescopes due to the atmospheric absorption. Space telescopes such as Hubble Space Telescope (HST) and International Ultraviolet Explorer (IUE) are needed to carry out sensitive spectroscopic observations in the UV wavelength. Therefore, high-sensitively rest-UV spectra of low-z AGNs are available only for a few objects, and thus we compiled the data of only radio-quiet Seyfert galaxies to compare the high-z objects and low-z ones. We collected the data of 3 low-z type 2 AGNs (NGC 1068; Snijders et al. 1986, NGC 5643 and NGC 5728; Evans et al. 1999). These line fluxes had been obtained with Short-Wavelength Prime (SWP), Long-Wavelength Prime (LWP), and Long-Wavelength Redundant (LWR) cameras at IUE for NGC 1068 and by the Faint Object Spectrograph (FOS)

at HST for NGC 5643 and NGC 5728.

3.3 Results

3.3.1 Rest-frame UV spectra of our targets

The reduced spectra of the three objects described in Section 3.2.1 are shown in Figures 3.1–3.3. We also show in Figures 3.1–3.3 a typical atmospheric transmission and sky spectrum, which suggest that the detected weak emission-lines are not seriously affected by strong atmospheric features nor strong air-glow emission lines. This sky spectrum was obtained from the SkyCalc sky model calculator[1] (Noll et al., 2012; Jones et al., 2013) provided by ESO. Many emission lines were detected including weak emission lines, such as N IV]λ1486, O III]λ1663, and [Ne IV]λ2424. Especially, 13 emission-lines were detected in TN J0920−0712. The spectra of 4C 24.28 and USS 1545−234 show 10 and 9 emission-lines, respectively (Table 3.2).

The fluxes, central wavelengths, FWHMs, and observed equivalent widths (EWs) of the detected emission lines with S/N $>$ 3 were measured with the IRAF task `splot` assuming a single Gaussian profile. Here the flux errors given in Table 3.2 include the pixel-to-pixel variance and the uncertainty in the continuum level estimate. Note that narrow emission lines in AGN spectra have been often fitted by more complicated profiles such as multi-component Gaussian profile (e.g., Veilleux, 1991; Greene & Ho, 2005; Mullaney et al., 2013). However, such complicated profiles have a larger number of free parameters than the simple Gaussian profile and thus difficult to be applied to weak emission lines with an insufficient S/N. Since the single Gaussian fit to our spectra works without significant residuals, we adopt the single Gaussian profile to fit emission lines in the spectra. The emission-line properties obtained through the fit are given in Table 3.2.

To confirm the consistency between the emission-line fluxes given in Matsuoka et al. (2009) and our results, we compare the emission-line flux ratios obtained in this work and in Matsuoka et al. (2009). The C III]/C IV flux ratio of TN J0920−0712 is 0.615±0.030 in this work and 0.578±0.018 in Matsuoka et al. (2009), thus these values are consistent within the 1σ error range. The remaining two objects also show consistent emission-line flux ratios with Matsuoka et al. (2009); the C III]/C IV flux ratio of 4C 24.28 is 0.657±0.035 in Matsuoka et al. (2009) and 0.719±0.056 in this work, and that of USS 1545−234 is 0.451±0.024 in Matsuoka et al. (2009) and 0.426±0.036 in this work. Therefore, we conclude that the flux ratios obtained through our analysis are consistent with those presented in Matsuoka et al. (2009).

[1] https://www.eso.org/observing/etc/bin/gen/form?INS.MODE=swspectr+INS.NAME=SKYCALC

Table 3.2: Detected emission lines

Name	line	flux (10^{-17} erg s^{-1} cm^{-2})	$\lambda^a_{\rm obs}$ (Å)	FWHM$^b_{\rm obs}$ (Å)	FWHM$^c_{\rm corr}$ (km s^{-1})	EW$_{\rm obs}$ (Å)
TN J0920−0712	Ly$\alpha\lambda$1216	305±16	4568.4	29.8	1861	2277±125
	N vλ1240	7.14±0.51	4664.7	28.1	1704	41.83±1.11
	O i+Si iiλ1305	1.15±0.17	4912.0	23.7	1316	7.51±0.46
	C iiλ1335	1.62±0.16	5018.0	18.5	928	12.54±0.77
	Si ivλ1397+O iv]λ1402	4.24±0.41	5264.7	40.9	2250	25.70±1.60
	N iv]λ1486	2.50±0.19	5581.3	34.3	1742	17.63±0.81
	C ivλ1549	29.6±0.8	5821.4	26.2	1209	214.1±1.7
	He iiλ1640	18.3±1.0	6161.5	21.2	839	138.4±1.1
	O iii]λ1663	3.32±0.48	6253.8	30.1	1313	24.24±1.32
	Si iiλ1814	1.68±0.20	6790.9	35.4	1443	9.95±1.63
	C iii]λ1909	18.2±1.1	7163.1	28.8	1045	185.9±6.6
	[O iii]+C ii+Si iiλ2322	11.1±0.83	8735.4	37.2	1127	208.5±17.0
	[Ne iv]λ2424	6.18±0.50	9104.5	32.8	898	88.23±4.11
4C 24.28	Ly$\alpha\lambda$1216	46.5±2.5	4761.8	29.3	1744	730.2±21.5
	N vλ1240	10.5±0.7	4854.8	42.8	2574	148.7±12.4
	O i+Si iiλ1305	0.67±0.10	5108.9	17.6	841	9.07±0.67
	Si ivλ1397+O iv]λ1402	3.34±0.29	5488.1	50.7	2704	37.72±1.71
	N iv]λ1486	1.28±0.20	5811.1	37.0	1812	23.25±3.25
	C ivλ1549	10.3±0.4	6061.9	46.3	2210	158.6±2.1
	He iiλ1640	8.98±0.30	6416.3	28.5	1189	132.8±8.0
	O iii]λ1663	2.13±0.25	6509.8	51.6	2370	39.89±0.89
	C iii]λ1909	7.41±0.50	7463.9	39.8	1481	111.2±8.7
	[O iii]+C ii+Si iiλ2322	0.96±0.21	9105.9	22.8	452	59.57±3.81
USS 1545-234	Ly$\alpha\lambda$1216	18.0±1.1	4563.9	15.2	798	672.8±25.8
	N vλ1240	7.01±0.48	4642.0	59.9	3822	140.6±14.6
	Si ivλ1397+O iv]λ1402	1.30±0.14	5253.2	33.2	1797	56.96±2.14
	C ivλ1549	6.76±0.30	5810.4	24.8	1130	283.7±3.4
	He iiλ1640	4.72±0.20	6150.7	17.3	593	173.7±6.5
	O iii]λ1663	0.85±0.13	6237.7	20.7	794	28.99±1.23
	C iii]λ1909	2.88±0.21	7151.3	22.2	712	141.6±2.3
	[O iii]+C ii+Si iiλ2322	1.13±0.31	8730.5	24.0	566	190.6±10.3
	[Ne iv]λ2424	1.72±0.24	9088.3	27.0	659	594.3±67.2

[a]Central wavelength. [b]Observed wavelength width in FWHM before the correction for the instrumental broadening.
[c]Velocity width in FWHM after the correction for the instrumental broadening.

3.3.2 Rest-frame UV spectra of additional data

The rest-frame UV emission lines whose properties are available in the literature for HzRGs and low-z type 2 AGNs described in Section 3.2.2 are listed in Table 3.3. These objects show many UV emission lines including relatively weak emission lines, such as N iv], O iii], and [Ne iv], as well as strong emissions such as C iv, He ii, and C iii]. The UV spectrum of 0828+193 shows the largest number of emission lines among our sample (for details, see Table 4 in Humphrey et al., 2008). By combining the emission-line flux ratios of our own sample (Section 3.3.1) and also the objects taken from the literature (Section 3.3.2), we discuss the physical and chemical properties of NLRs in HzRGs and low-z AGNs combined with photoionization models whose details are explained in the next section.

Table 3.3: Data of additional targets

Name	z	available emission lines	Reference[a]
0211−122	2.340	Si IV + O IV], N IV], C IV, He II, O III], C III], [Ne IV]	H08
0406−244	2.440	Si IV + O IV], C IV, He II, O III], C III], [Ne IV]	H08
0731+438	2.429	Si IV + O IV], N IV], C IV, He II, O III], C III], [Ne IV]	V01
0828+193	2.572	Si IV + O IV], N IV], C IV, He II, O III], C III], [Ne IV]	H08
0943−242	2.922	Si IV + O IV], N IV], C IV, He II, O III], C III]	V01
1558−003	2.479	Si IV + O IV], N IV], C IV, He II, O III], C III], [Ne IV]	H08
3C 256	1.824	Si IV + O IV], C IV, He II, O III], C III], [Ne IV]	S99
4C−00.54	2.360	Si IV + O IV], C IV, He II, O III], C III], [Ne IV]	H08
4C+23.56	2.470	Si IV + O IV], N IV], C IV, He II, O III], C III], [Ne IV]	H08
4C+40.36	2.265	Si IV + O IV], N IV], C IV, He II, O III], C III], [Ne IV]	H08
4C+48.48	2.343	Si IV + O IV], N IV], C IV, He II, O III], C III], [Ne IV]	V01
NVSS J002402−325253	2.043	Si IV + O IV], C IV, He II, O III], C III], [Ne IV]	DB06
NGC 1068	0.0038[b]	Si IV + O IV], N IV], C IV, He II, O III], C III], [Ne IV]	S86
NGC 5643	0.0040[b]	Si IV + O IV], N IV], C IV, He II, C III], [Ne IV]	E99
NGC 5728	0.0094[b]	Si IV + O IV], N IV], C IV, He II, O III], C III], [Ne IV]	E99

[a]S86 = Snijders et al. (1986); E99 = Evans et al. (1999); S99 = Simpson et al. (1999); V01 = Vernet et al. (2001); DB06 = De Breuck et al. (2006); H08 = Humphrey et al. (2008).
[b]Redshifts from the NASA/IPAC Extragalactic Database (NED).

3.4 Photoionization models

As mentioned in Section 3.1, the main ionization mechanism of NLR clouds in AGNs has been thought to be the photoionization by ionizing photons from the central engine of AGNs (e.g., Binette et al., 1996; Komossa & Schulz, 1997; Groves et al., 2004; Thomas et al., 2016). On the other hand, the collisional ionization of NLR clouds by fast shocks associated to radio jet and outflows has been also suggested for some AGNs (e.g., Knop et al., 1996; Bicknell et al., 1998; Allen et al., 2008; Shih et al., 2013; Terao et al., 2016). Matsuoka et al. (2009) reported that most gas clouds (especially clouds emitting high-ionization emission lines) in NLRs of HzRGs are photoionized, based on the C III]/C IV versus C IV/He II diagnostic diagram. Physical and chemical properties of ionized gas clouds in NLRs can be investigated through the comparison between photoionization models and observed emission-line spectra. In particular, the UV emission-line spectrum of high-z type 2 AGNs has been studied extensively, because it can be accessible in optical spectroscopic observations without suffering from the BLR emission that is very strong in type 1 AGNs. Most of past studies about rest-UV emission-line diagnostics for high-z type 2 AGNs have been performed by using only strong emission lines, such as C IV, C III], He II, and N V (e.g., Villar-Martin et al., 1996; De Breuck et al., 2000; Nagao et al., 2006b; Humphrey et al., 2008; Bryant et al., 2009; Matsuoka et al., 2018a). In such studies, due to an insufficient number of available emission lines, any diagnostic analysis requires some important assumptions to infer any physical or chemical parameters; e.g., the gas metallicity has been sometimes determined by assuming a fixed gas density (Nagao et al., 2006b; Matsuoka et al., 2009). Therefore, analyses including also weaker UV emission lines are crucially required to diagnose ISM properties without assuming such important ISM parameters. However, weaker UV emission lines have not been widely utilized to diagnose NLR gas clouds so far, because of the observational difficulty. Since deep rest-UV spectra of AGNs in this work clearly show various weak emission lines, we can perform diagnostic studies with many

combinations of emission lines. Therefore in this work, we try to derive chemical and physical parameters of ionized gas clouds in NLRs through the comparison between the measured emission-line fluxes and detailed photoionization models.

We calculated the photoionization model using Cloudy version 13.03 (Ferland et al., 2013). We used the "table AGN" command as the input SED (see Figure 2.11), which reproduces the typical SED of AGNs (Mathews & Ferland, 1987). The relative elemental abundance ratio is assumed to be the solar composition (Grevesse et al., 2010), except for helium and nitrogen. For helium, we take the primordial component and the primary nucleosynthesis component into account. Specifically, it is determined by He/H $= 0.08096 + 0.02618(Z/Z_{\odot})$. The nitrogen relative abundance is assumed to be proportional to the square of the metallicity at the high-metallicity range, taking the nature of nitrogen as a secondary element into account. More specifically, the nitrogen relative elemental abundance is determined by log (N/H) $= -4.57+\log(Z/Z_{\odot})$ for 0.1 and 0.2 $Z_{\odot}$ models and log (N/H) $= -4.17 + 2\log(Z/Z_{\odot})$ for $Z > 0.3$ $Z_{\odot}$ models. These analytic expressions adopted in this work for helium and nitrogen were taken from Dopita et al. (2000). We assumed dust-free gas clouds in our Cloudy runs, because high-ionization lines arise mostly at the inner part of the NLR where dust grains do not survive (Marconi et al., 1994; Nagao et al., 2003, 2006b). The parameter ranges covered in the model calculations were the hydrogen gas density $n = 10^2 - 10^6$ cm^{-3}, ionization parameter $U = 10^{-3} - 10^{-0.5}$, and metallicity $Z = 0.1-5.0$ $Z_{\odot}$. The step of calculations was 0.1 dex for each parameter, and thus 53300 models were calculated. The model calculations stopped when the ionized fraction of hydrogen drops to 15 %, below which the gas does not emit rest-frame UV emission lines significantly.

Although the model runs in this work were executed by assuming one-zone constant-density clouds, it has been reported that high-ionization lines and low-ionization lines arise at different parts in the NLR with a significantly different gas density (e.g., Ferguson et al., 1997; Rose et al., 2015; Adhikari et al., 2016). In this work, we focus only on high-ionization lines (Si IV, O IV], N IV], C IV, He II, O III], C III], and [Ne IV]) that are expected to arise at a similar part within NLRs. We determine the model parameters (the gas density, ionization parameter, and gas metallicity) simultaneously, by the χ square (χ^2) test where the reduced χ^2 ($\tilde{\chi}^2$) is calculated as follows, except for the non-detection lines:

$$\tilde{\chi}^2 = \sum^{n} \left(\frac{O_{\rm obs} - O_{\rm model}}{\sigma_{\rm obs}} \right)^2 / d, \tag{3.1}$$

where $O_{\rm obs}$ is the observed line ratio, $O_{\rm model}$ is the predicted line ratio by a photoionization model, $\sigma_{\rm obs}$ is the error of the observed line ratio, and d is the degree of the freedom. All line fluxes are normalized by the C IV flux. The best-fit parameters are determined by searching for the minimum $\tilde{\chi}^2$. The obtained minimum $\tilde{\chi}^2$ and best-fit parameters are summarized in Table 3.4 for 15 HzRGs and three nearby AGNs in our sample. The errors of parameters were estimated by the 1σ confidence level inferred from the minimum χ^2.

Table 3.4: Comparison between photoionization models and observations

Name	$\tilde{\chi}^2$	Z ($Z_\odot$)	$\log n$ (cm^{-3})	$\log U$
TN J0920−0712	7.49	$1.3^{+0.2}_{-0.1}$	$4.2^{+0.4}_{-0.1}$	$-1.7^{+0.0}_{-0.1}$
4C 24.28	26.1	$2.3^{+0.2}_{-0.1}$	$5.3^{+0.1}_{-0.1}$	$-0.5_{-0.1}$ [a]
USS 1545−234	16.0	$1.8^{+0.5}_{-0.5}$	$4.4^{+0.5}_{-0.6}$	$-1.4^{+0.4}_{-0.1}$
0211−122	27.3	$1.2^{+0.1}_{-0.1}$	$4.0^{+0.2}_{-0.3}$	$-1.2^{+0.1}_{-0.1}$
0406−244	5.13	$2.1^{+2.9}_{-1.3}$ [a]	$4.5^{+1.2}_{-2.5}$ [a]	$-2.0^{+1.5}_{-0.1}$ [a]
0731+438	32.2	$0.9^{+0.1}_{-0.1}$	$2.7^{+0.5}_{-0.4}$	$-1.4^{+0.0}_{-0.1}$
0828+193	29.3	$0.8^{+0.1}_{-0.1}$	$2.5^{+0.9}_{-0.5}$ [a]	$-1.4^{+0.0}_{-0.1}$
0943−242	13.7	$0.9^{+0.1}_{-0.0}$	$2.0^{+0.8}$ [a]	$-1.6^{+0.0}_{-0.1}$
1558−003	6.00	$0.8^{+0.3}_{-0.2}$	$4.0^{+0.8}_{-1.4}$	$-1.5^{+0.0}_{-0.1}$
3C 256	203.0	$1.6^{+0.1}_{-0.0}$	$4.2^{+0.1}$	$-1.9^{+0.0}_{-0.0}$
4C−00.54	55.4	$1.7^{+0.1}_{-0.7}$	$4.4^{+0.3}_{-2.0}$	$-0.8^{+0.1}_{-0.4}$
4C+23.56	17.9	$1.3^{+0.7}_{-0.5}$	$3.6^{+0.9}_{-1.6}$ [a]	$-1.5^{+0.2}_{-0.2}$
4C+40.36	15.7	$0.5^{+0.0}_{-0.1}$	$2.0^{+1.6}$ [a]	$-1.8^{+0.0}_{-0.1}$
4C+48.48	29.2	$1.5^{+0.2}_{-0.2}$	$3.8^{+0.3}_{-0.3}$	$-1.5^{+0.0}_{-0.1}$
J0024−3252	3.79	$1.7^{+0.9}_{-0.5}$	$4.1^{+0.6}_{-0.5}$	$-1.8^{+0.1}_{-0.1}$
NGC 1068	3.30	$1.4^{+0.6}_{-0.5}$	$4.7^{+0.5}_{-0.7}$	$-1.5^{+0.3}_{-0.2}$
NGC 5643	178.7	$1.3^{+0.0}_{-0.1}$	$4.4^{+0.0}_{-0.2}$	$-1.7^{+0.0}_{-0.0}$
NGC 5728	18.1	$1.4^{+0.4}_{-0.4}$	$4.4^{+0.3}_{-0.6}$	$-1.9^{+0.1}_{-0.0}$

[a]The cases reaching the upper/lower limit of parameter ranges in our model runs.

3.5 Discussion

3.5.1 Interpretations of model calculations

As shown in Table 3.4, the best-fit $\tilde{\chi}^2$ value in many cases is very large ($\gtrsim 20$). This large $\tilde{\chi}^2$ is caused probably due to over-simplification of our photoionization models. In our model calculations, we assumed the constant chemical composition without dust grains, a typical AGN SED, and one-zone constant-density clouds. It has been reported that gas clouds in NLRs are stratified, in the sense that more highly-ionized clouds with higher density reside at inner parts in NLRs, which is inferred from kinematic studies (e.g., De Robertis & Osterbrock, 1984; Veilleux, 1991; Ho et al., 1996) and detailed photoionization models (e.g., Ferguson et al., 1997; Nagao et al., 2000). Though our models focus only on relatively high-ionization lines, the models still suffer from such non-uniformity of NLRs that makes the minimum $\tilde{\chi}^2$ values considerably high. However, we adopt best-fit parameters even when the minimum $\tilde{\chi}^2$ values are rather high, because our main aim is to infer the averaged properties of highly-ionized parts of NLRs. Note that an earlier study that tried to reproduce emission-line spectra of NLRs in AGNs with photoionization models also reported high χ^2 for some AGNs, plausibly due to the

same reason as our work (Iwamuro et al., 2003).

Figure 3.4 shows the difference in emission-line flux ratios between the observed data and prediction by our photoionization models at the minimum $\tilde{\chi}^2$. In most cases, the observed C III]/C IV and He II/C IV flux ratios are comparable with model predictions, while [Ne IV]/C IV flux ratios are under-predicted by models. One possible explanation of this discrepancy is the higher ionization potential of Ne IV (63.5 eV) compared to the other emission lines (Table 3.5). Given the stratified structure of actual NLRs, there could be an additional highly-ionized clouds at the inner part in NLRs that are not taken into account in our one-zone photoionization models.

Table 3.5: Ionization potentials of ions

Ion	ionization potential (eV)
C III	24.4
He II	24.6
O III	35.1
Si IV	33.5
N IV	47.4
C IV	47.9
O IV	54.9
Ne IV	63.5

The comparison between observed emission-line flux ratios and photoionization models suggests that most objects show higher gas metallicities than the solar metallicity ($Z \gtrsim 1.0\ Z_\odot$). These inferred metallicities are consistent with earlier works for HzRGs (De Breuck et al., 2000; Nagao et al., 2006b; Matsuoka et al., 2009). This result suggests that the NLRs of HzRGs in our sample are already chemically evolved even at $z > 2$. The inferred ionization parameter is $U \sim 10^{-2} - 10^{-1}$ in our sample. De Breuck et al. (2000) and Bryant et al. (2009) reported that the ionization parameter of HzRGs is in the range of $10^{-2.5} < U < 10^{-1.5}$ using rest-UV emission line ratios combined with photoionization models assuming the solar metallicity and gas density ($n = 10^2$ and 10^3 cm^{-3}). Our results are slightly higher than those previous works, but the difference is insignificant. The inferred gas density of HzRGs is widely distributed in the range of $n = 10^2 - 10^5$ cm^{-3} with a relatively large uncertainty than the derived uncertainty in the ionization parameter and gas metallicity. The inferred range of the gas density is consistent with earlier works, in which photoionization models with $n = 10^2 - 10^5$ cm^{-3} are adopted (e.g., De Breuck et al., 2000; Nagao et al., 2006b; Matsuoka et al., 2009). Silva et al. (2018) examined photoionization models for studying the rest-frame UV and optical emission-line spectrum of 0943−242, which is included in our sample. In their models, the hydrogen gas density was fixed to $n = 100$ cm^{-3}. The derived best-fit parameters are $Z = 2.1\ Z_\odot$ and $\log U = -1.74$. The derived ionization parameter is close to our measurement ($\log U = -1.6^{+0.0}_{-0.1}$) while the derived metallicity is higher than our measurement ($Z = 0.9^{+0.1}_{-0.0}\ Z_\odot$). This discrepancy in the metallicity may be caused by the fixed gas density in their models or the difference in the

emission lines used in the analysis.

Here we discuss which emission line ratios are effective for diagnosing each parameter. For this purpose, we check the behavior of each flux ratio depending on the physical parameters. Figures 3.5−3.10 show the dependence of the flux ratios on the metallicity, where the models are calculated with parameter sets of log $U = -3, -2, -1$, and -0.5, and log n =2, 4, and 6. Figure 3.7 and 3.10 show that the He II/C IV and [Ne IV]/C IV line ratios decrease with increasing the gas density from log n = 2 to 6 (i.e., from left to right panel). These trends suggest that the gas density is largely constrained by these two line ratios. This density dependence of He II/C IV in NLRs has been reported in earlier works (e.g., Nagao et al., 2006b). It is natural that the [Ne IV]/C IV line ratio shows a negative dependence on the gas density, since the [Ne IV] line is a forbidden emission with a critical density of $n_{\rm cr} \sim 10^5$ cm^{-3} (actually the [Ne IV] line is an unresolved doublet emission of [Ne IV]λ2422 and [Ne IV]λ2425 with $n_{\rm cr} = 2.5 \times 10^5$ cm^{-3} and 8.0×10^4 cm^{-3}, respectively; see, e.g., Zheng 1988). In Figure 3.6, the N IV]/C IV line ratio shows no difference with changing the gas density and ionization parameter except for models with a high metallicity, low density, and low ionization parameter, but depends on the metallicity except for low gas density models. The lack of dependences of this N IV]/C IV line ratio on the ionization parameter is because the ionization potential of N IV] and C IV is very similar (see Table 3.5), while the dependence of this line ratio on the metallicity is largely caused by the nature of a secondary element of the nitrogen (see Nagao et al. 2012 for similar discussion). Therefore N IV]/C IV line ratio is useful to give constraints on the metallicity. The ionization parameter can be diagnosed by combining Si IV+O IV]/C IV, He II/C IV, O III]/C IV, C III]/C IV, and [Ne IV]/C IV, i.e., combinations of two emission lines with different ionization potentials (see Table 3.5). These line ratios increase with a decreasing ionization parameter.

The dependence on the gas density of C III]/C IV flux ratio is thought to be small, while that of He II/C IV is not small (e.g., Nagao et al., 2006b; Matsuoka et al., 2009). Although these emission-line flux ratios have been used to discuss the metallicity of NLR clouds by assuming a certain gas density, the uncertainty of gas density for discussing the metallicity had not been discussed in detail. Figure 3.7 shows that the He II/C IV flux ratio depends on the gas density at most 2 dex from log n = 2 to 6 at the highest metallicity model, and thus the previous metallicity measurement may be affected by this density dependence. For example, the He II/C IV flux ratio of TN J0920−0712 is 0.618. This corresponds to $\sim 1.5\ Z_\odot$ assuming a model with $n = 10^4$ cm^{-3} and $U = 10^{-1}$, while metallicity is inferred to be $\sim 5\ Z_\odot$ at a $n = 10^6$ cm^{-3} model. In this work, the density is well determined with an accuracy within 0.5 dex thanks to many faint emission lines, and thus the metallicity can be estimated with a smaller uncertainty than previous studies on the NLR metallicity.

3.5.2 The nature of HzRGs

Here we investigate possible dependencies of the derived parameters of NLR clouds on the AGN luminosity. In Table 3.6, the C IV and He II luminosities of our sample are summarized. Both of the two line luminosities have been often used as indicators of the AGN luminosity, but the He II luminosity is a better indicator for the AGN activity. This is because the He II luminosity is mostly determined by the luminosity of the He^+-ionizing photon but insensitive to various gas parameters such as the gas density and ionization parameter. Note that, though the relative He^+-ionizing photon luminosity depends on the SED in UV, the UV SED of AGNs is very similar (e.g., Zheng et al., 1997; Koratkar & Blaes, 1999; Richards et al., 2006). The derived parameters of NLR clouds, i.e., the gas density, ionization parameter, and metallicity, are shown as functions of the He II luminosity in Figure 3.11. Those parameters show no significant dependencies on the He II luminosity. This is interesting because some previous studies reported the dependence of the NLR metallicity on the AGN luminosity (e.g., Nagao et al., 2006b; Matsuoka et al., 2009). Note that such luminosity dependence of the AGN metallicity has been reported also for BLR clouds (e.g., Hamann & Ferland, 1993; Nagao et al., 2006c; Matsuoka et al., 2011b). The lack of the significant luminosity dependence of the NLR metallicity in our sample is probably due to the small number statistics of our work; in previous works the luminosity dependence of the NLR metallicity is investigated based on a larger sample that consists of $\sim$50 HzRGs (see Nagao et al., 2006b; Matsuoka et al., 2009).

We also examine the dependence of the NLR parameters on the radio power, for investigating whether some NLR parameters are strongly affected by the radio jet in HzRGs. For this purpose, we compiled the radio power at 325 MHz (P_{325}) and 1400 MHz (P_{1400}), that are taken from De Breuck et al. (2000). The relation between the NLR parameters and the radio power is shown in Figures 3.12 and 3.13. These figures show that there are no clear dependence of the NLR parameters on the radio power, suggesting that the physical properties of NLRs in our sample are not significantly affected by the radio jet. This is consistent to the idea that the NLR clouds are mostly ionized by the photoionization, not by the fast shock associated with the radio jet.

The obtained NLR metallicity for our sample is distributed in the range of 0.5–2.3 $Z_\odot$ (Figure 3.11). Since the NLR of most HzRGs in our sample is characterized by the solar or super-solar metallicity, it is suggested that host galaxies of HzRGs are chemically well matured even at $z \sim 3$. Some earlier works (e.g., Nagao et al., 2006b; Matsuoka et al., 2009) also showed this picture, but with some assumptions on the NLR gas parameters (such as a fixed gas density). Now the chemical maturity of HzRGs is obtained with less assumptions thanks to deep spectra with weak emission lines.

3.5.3 Comparison with low-z AGNs

It is interesting to compare the inferred ionization parameter and gas density of NLRs in HzRGs at $z \sim 3$ with those in low-z type 2 AGNs, because it has been claimed that the ionization

Table 3.6: Line luminosities and radio power

Name	log $L_{\rm CIV}$ (erg s^{-1})	log $L_{\rm HeII}$ (erg s^{-1})	log P_{325} [a] (erg s^{-1} Hz^{-1})	log P_{1400} [a] (erg s^{-1} Hz^{-1})
J0920−0712	43.27	43.06	36.00	35.05
4C 24.28	42.87	42.81	36.39	35.65
USS 1545−234	42.63	42.47	35.92	35.24
Additional HzRG samples				
0211−122	42.44	42.18	35.94	35.21
0406−244	42.63	42.75	36.46	35.62
0731+438	43.33	43.15	36.16	35.53
0828+193	43.48	43.14	35.55	34.84
0943−242	43.53	43.53	36.10	35.36
1558−003	43.09	42.66	–	–
3C 256	43.08	43.10	36.15	35.51
4C−00.54	42.18	42.04	35.65	35.00
4C+23.56	41.94	41.86	–	–
4C+40.36	42.43	42.18	36.24	35.42
4C+48.48	43.37	43.35	35.87	35.10
J0024−3252	42.50	42.50	–	–
low-z sample				
NGC 1068	40.80	40.36	–	–

[a] These radio power were collected from De Breuck et al. (2000).

parameter and gas density of the ISM are systematically different between low-z and high-z star-forming galaxies. For the ionization parameter, Nakajima & Ouchi (2014) showed that star-forming galaxies at $z \sim 2-3$ show systematically higher ionization parameter than typical low-z SDSS star-forming galaxies (see also Nakajima et al., 2016). For the gas density, Sanders et al. (2016) reported a systematically higher gas density of the ionized gas in star-forming galaxies at $z \sim 2.3$ than low-z SDSS star-forming galaxies. Therefore it is worth studying possible redshift dependencies of the ionization parameter and gas density also for NLR clouds in AGNs. We compare the ionization parameter and gas density of NLRs in HzRGs and those in low-z type 2 AGNs in Figure 3.14. These properties of low-z samples were estimated using the line ratio of [S II]$\lambda\lambda$6716,6731 and [Ar IV]$\lambda\lambda$4711,4740 doublets for the gas density and [O II]λ3727/[O III]λ5007 for the ionization parameter (Vaona et al., 2012). It is clearly shown in this figure that the ionization parameter of NLR gas clouds is systematically higher in HzRGs ($U \sim 10^{-2}-10^{-1}$) than that in low-z type 2 AGNs ($U \lesssim 10^{-2}$). Such a low ionization parameter has been inferred for NLR clouds in low-z type 2 AGNs in some other earlier works (Ferland & Netzer, 1983; Nagao et al., 2001b). As for the gas density, some HzRGs show a comparable NLR density to low-z type 2 AGNs ($n \lesssim 10^4$ cm^{-3}) while other HzRGs show a considerably higher NLR density ($n \gtrsim 10^4$ cm^{-3}). However, we cannot conclude only from this figure that the gas density and ionization parameter of NLR clouds in AGNs show the redshift evolution,

because those parameters are inferred by different emission lines between the HzRG sample and low-z sample. Systematic UV spectroscopic observations for low-z AGNs are needed to interpret high-z observations correctly.

3.6 Conclusion

In this chapter, we focused on high-sensitivity rest-UV spectra of 15 radio galaxies at redshift ~ 3 to measure the flux of several emission lines including relatively faint ones. We diagnose the physical and chemical properties of the ISM in NLR for each object through the comparison between the measured emission-line fluxes and detailed photoionization models. Main results of this work are as follows.

1. Most HzRGs show moderately high gas metallicity, that is close to or higher than the solar metallicities (i.e., $Z \gtrsim Z_{\odot}$). This result is consistent with some previous studies (e.g., Nagao et al., 2006b; Matsuoka et al., 2009), but obtained with less assumptions in the photoionization model with respect to those previous works. The obtained result strongly suggests that HzRGs at $z \sim 3$ are already matured chemically, even in the early Universe where the cosmic age was only ~ 2 Gyr.

2. The inferred physical parameters (gas density, ionization parameter, and gas metallicity) of NLRs in HzRGs show no correlation with the radio power. This suggests that the physical properties of NLRs in our sample are not significantly affected by the radio jet.

3. Compared to low-z type 2 AGNs, gas clouds in NLRs of HzRGs tend to show higher ionization parameter and gas density. This result implies that ISM properties of AGN host galaxies show the redshift evolution that is seen also in star-forming galaxies.

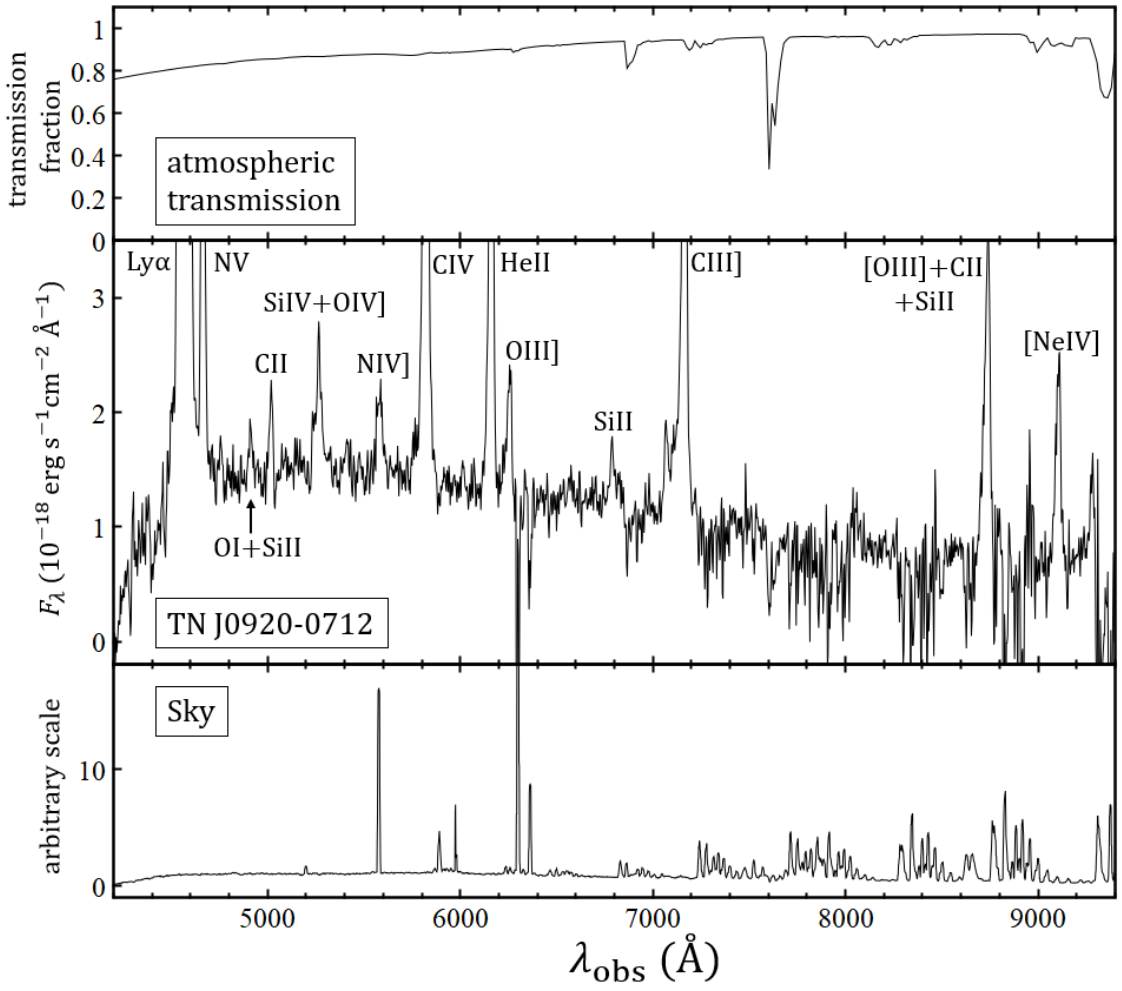

Fig. 3.1: Rest-frame ultraviolet spectrum of TN J0920−0712 (middle panel). The detected emission lines are labeled. Top panel shows a typical atmospheric transmission at the VLT site (Noll et al., 2012; Jones et al., 2013). Bottom panel shows a typical sky spectrum obtained during our runs.

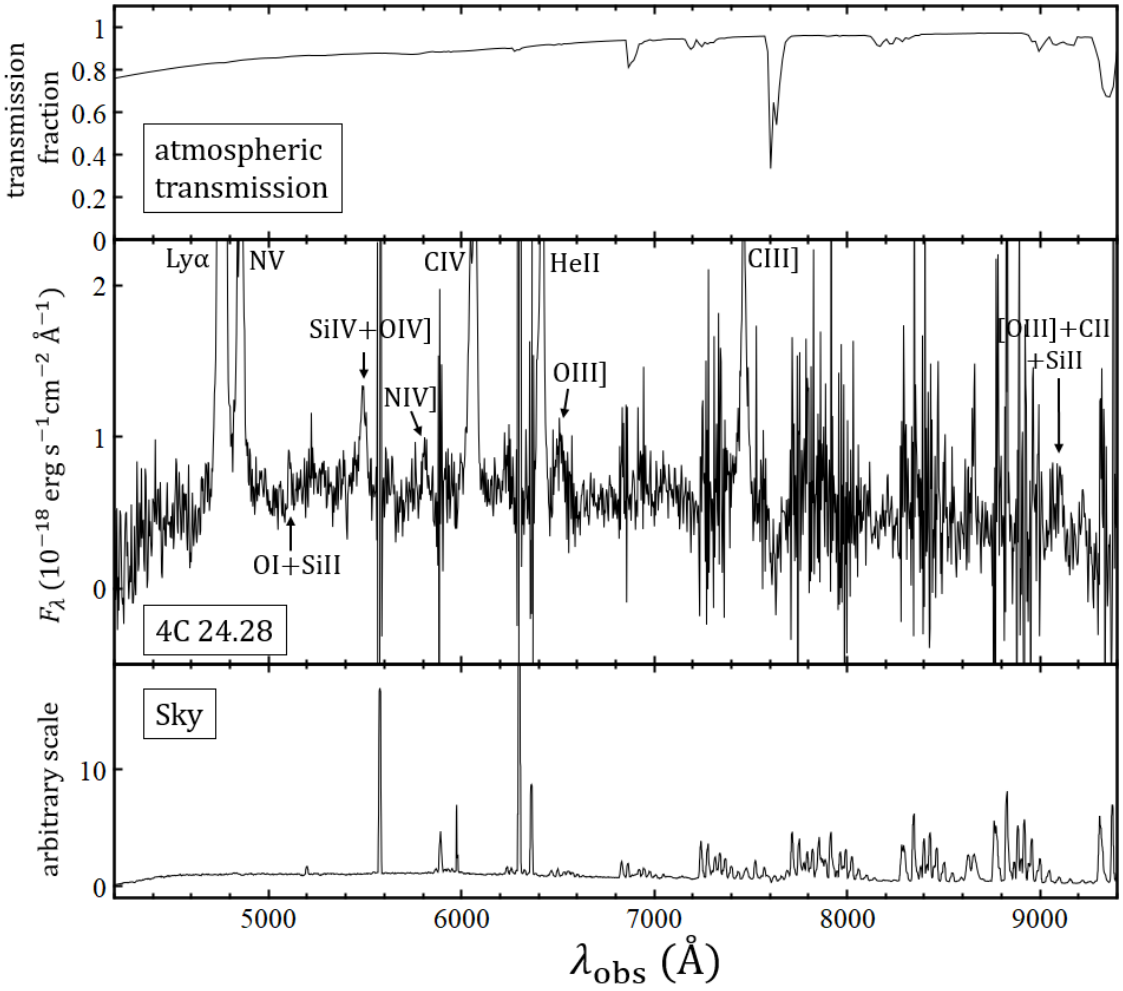

Fig. 3.2: Same as Figure 3.1 but for 4C 24.28.

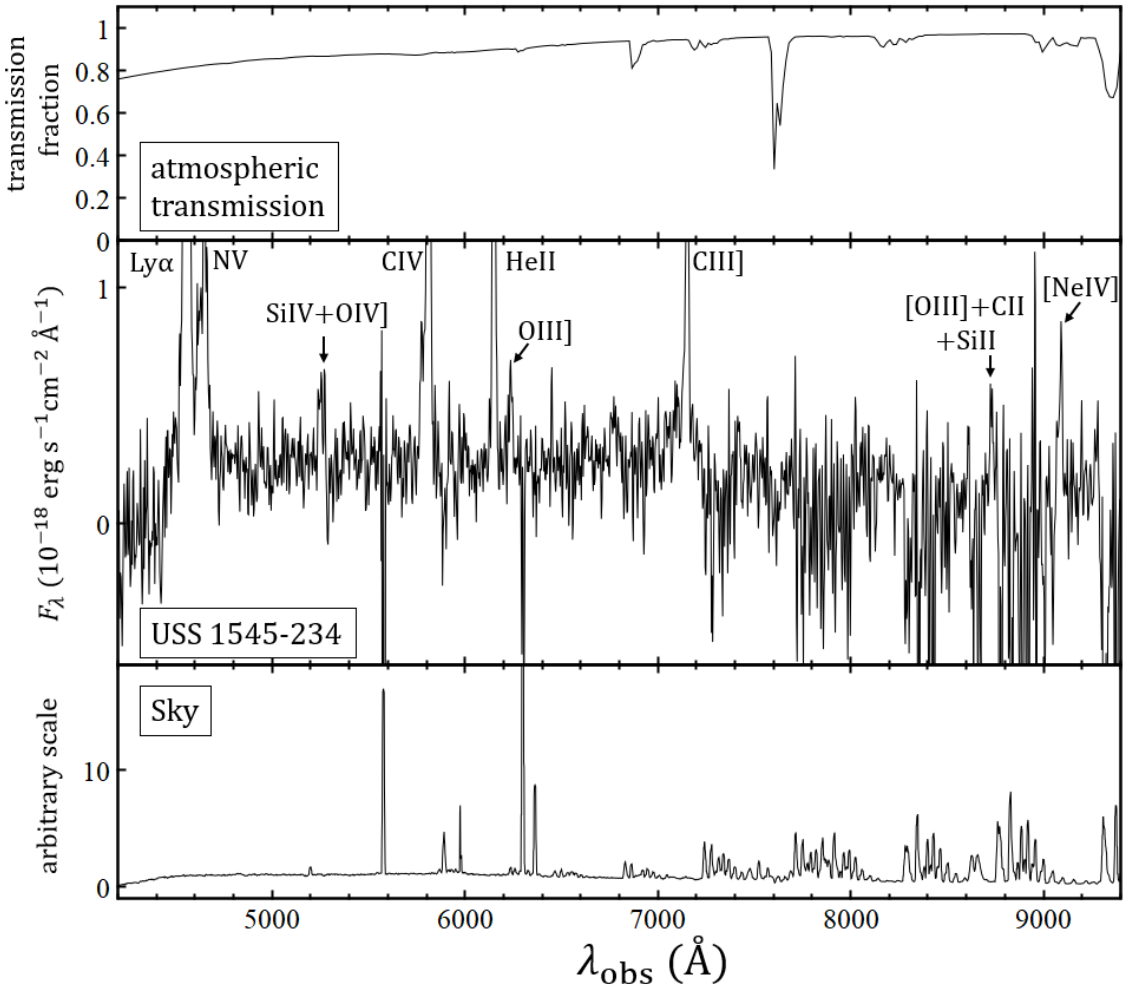

Fig. 3.3: Same as Figure 3.1 but for USS 1545−234.

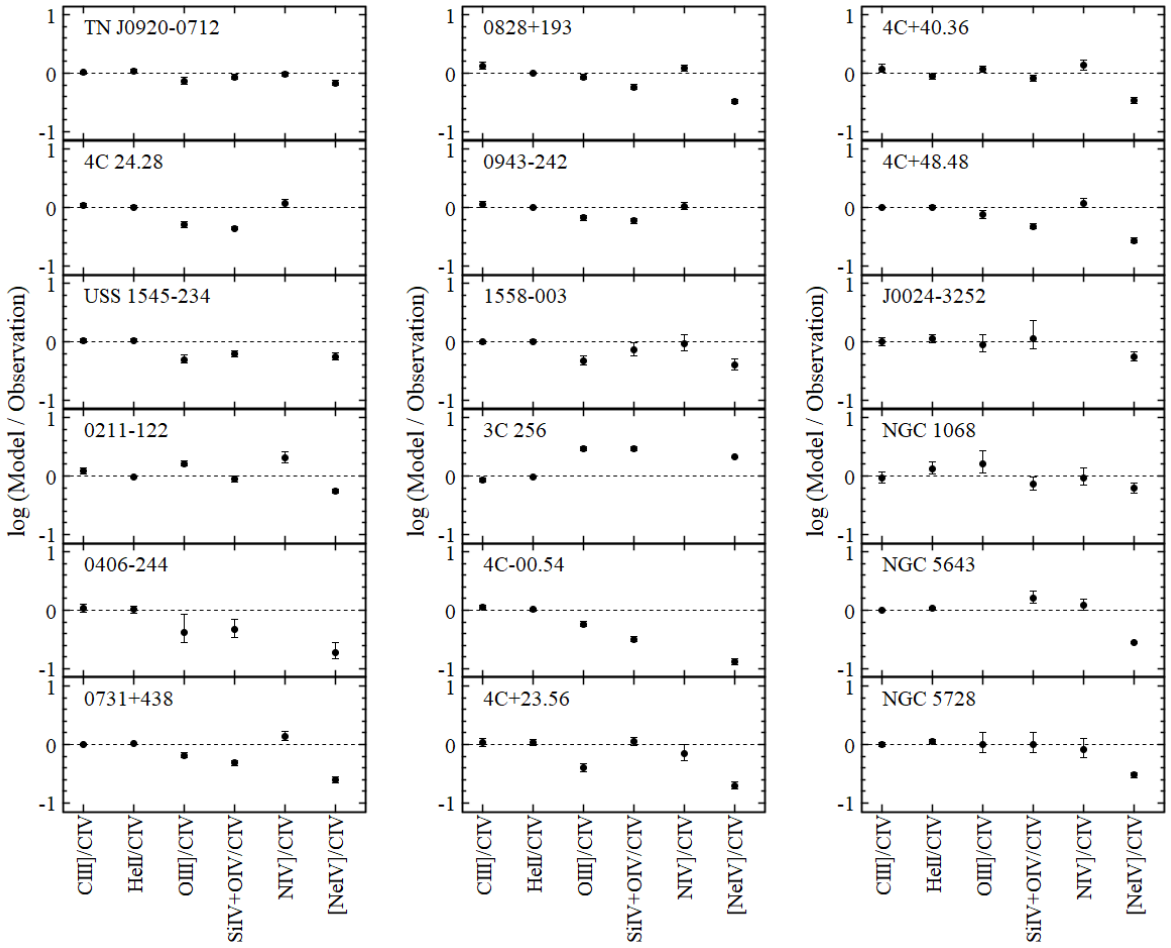

Fig. 3.4: Comparison of each emission-line flux ratio between photoionization models and observations at the minimum $\tilde{\chi}^2$. In x-axis, the flux ratios are shown in order of increasing the ionization potential of the corresponding ion (of the numerator), from left to right. The dashed line indicates the unity, i.e., the observed flux ratios are reproduced by best-fit models.

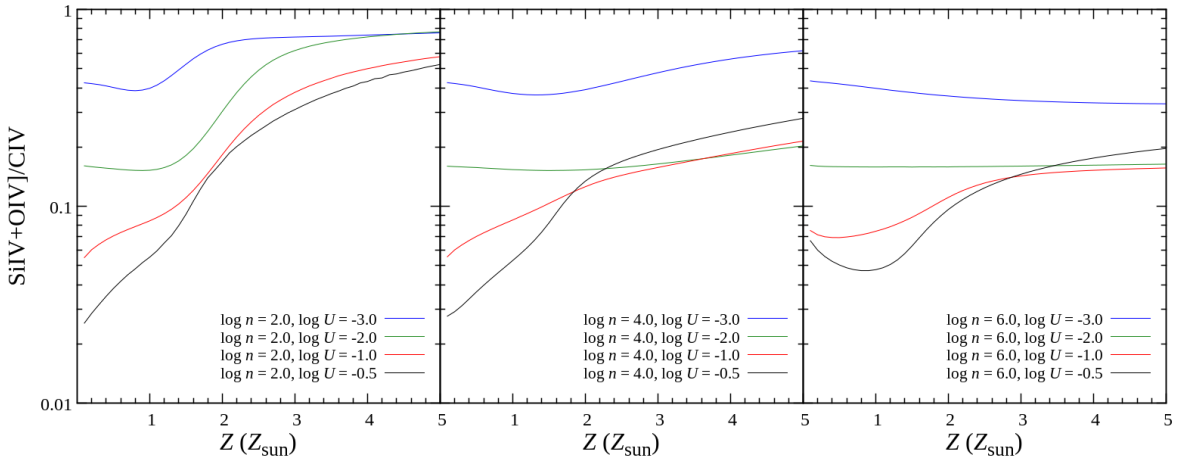

Fig. 3.5: The relationship between the predicted Si IV+O IV]/C IV flux ratio and metallicity. From left to right, models with log n = 2, 4, and 6 are shown. The blue, green, red, and black lines denote the results with log $U = -3, -2, -1$, and -0.5, respectively.

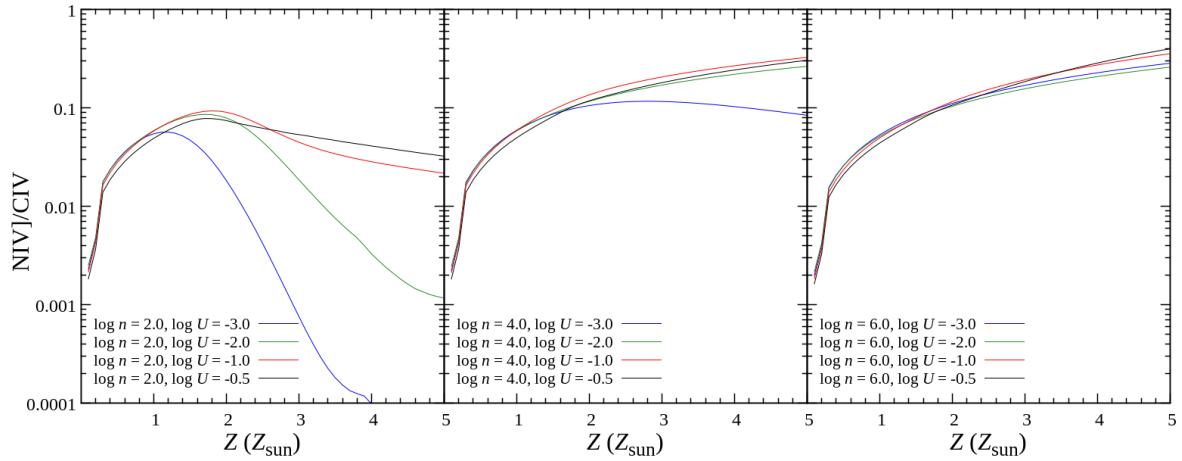

Fig. 3.6: Same as Figure 3.5 but for the N IV]/C IV flux ratio.

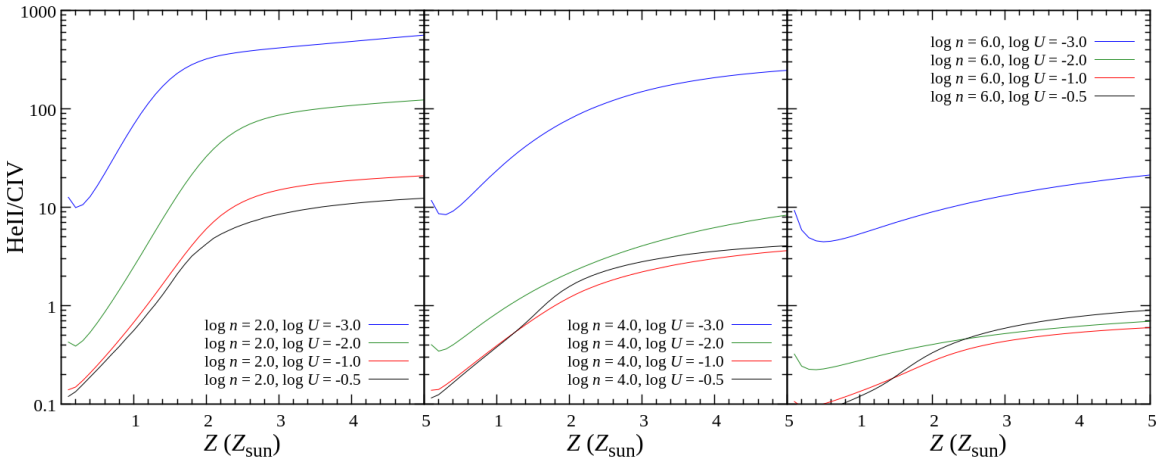

Fig. 3.7: Same as Figure 3.5 but for the He II/C IV flux ratio.

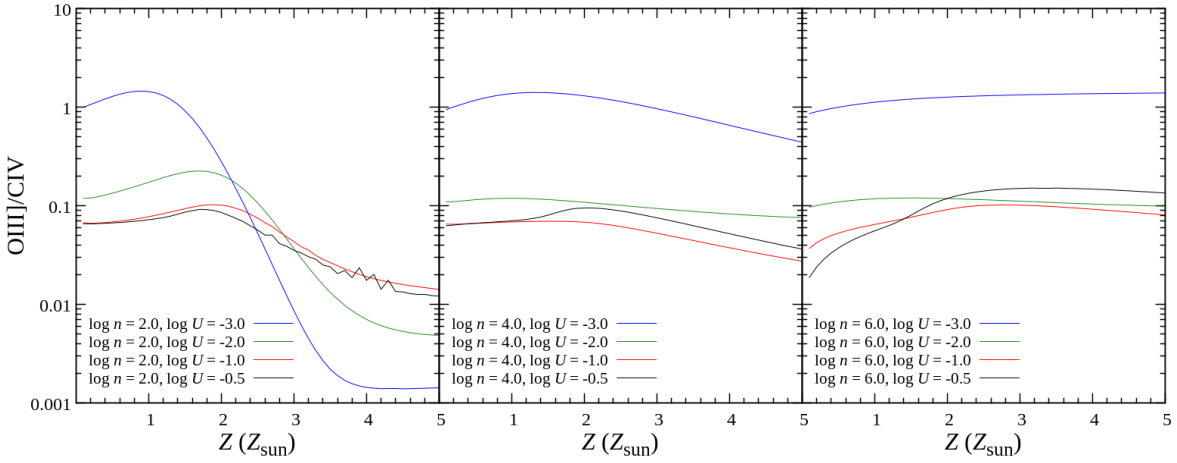

Fig. 3.8: Same as Figure 3.5 but for the O III]/C IV flux ratio.

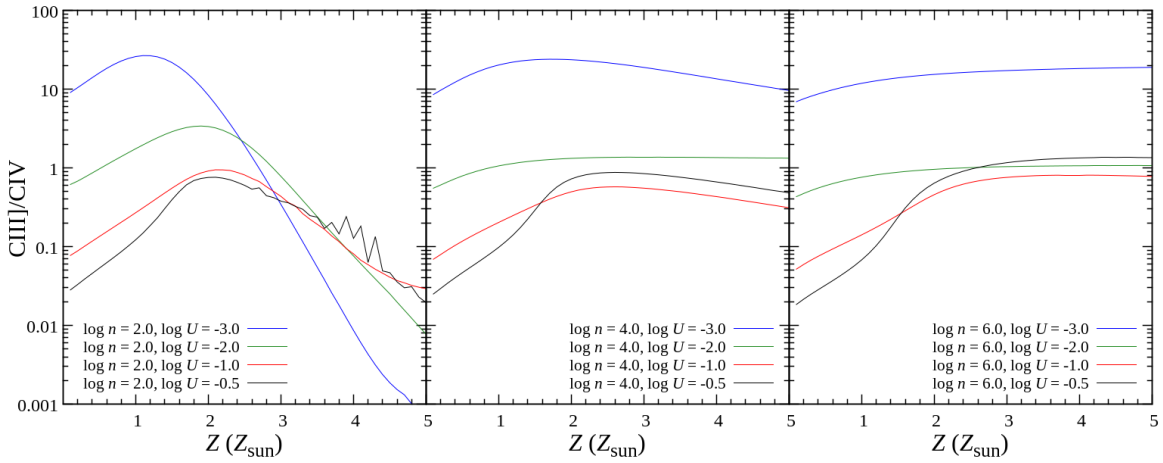

Fig. 3.9: Same as Figure 3.5 but for the C III]/C IV flux ratio.

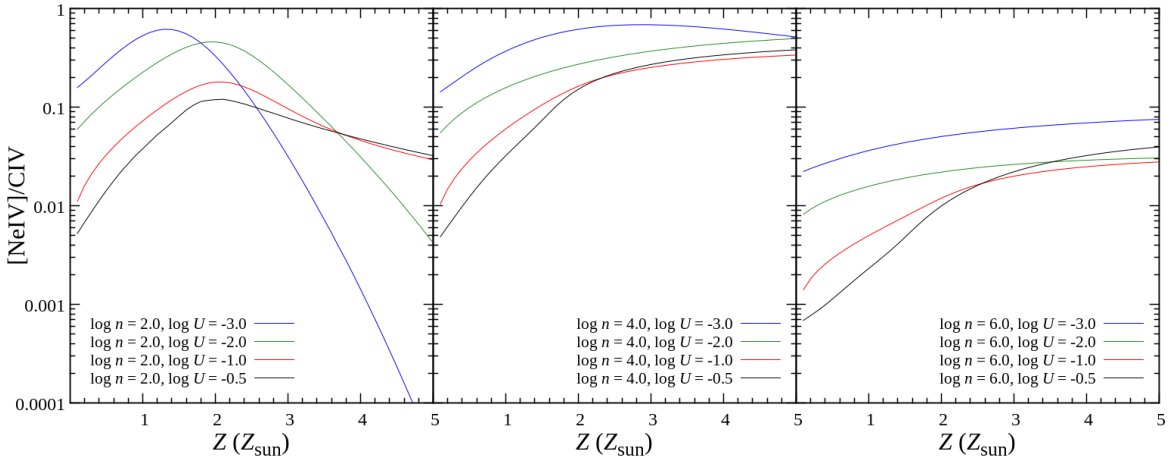

Fig. 3.10: Same as Figure 3.5 but for the [Ne IV]/C IV flux ratio.

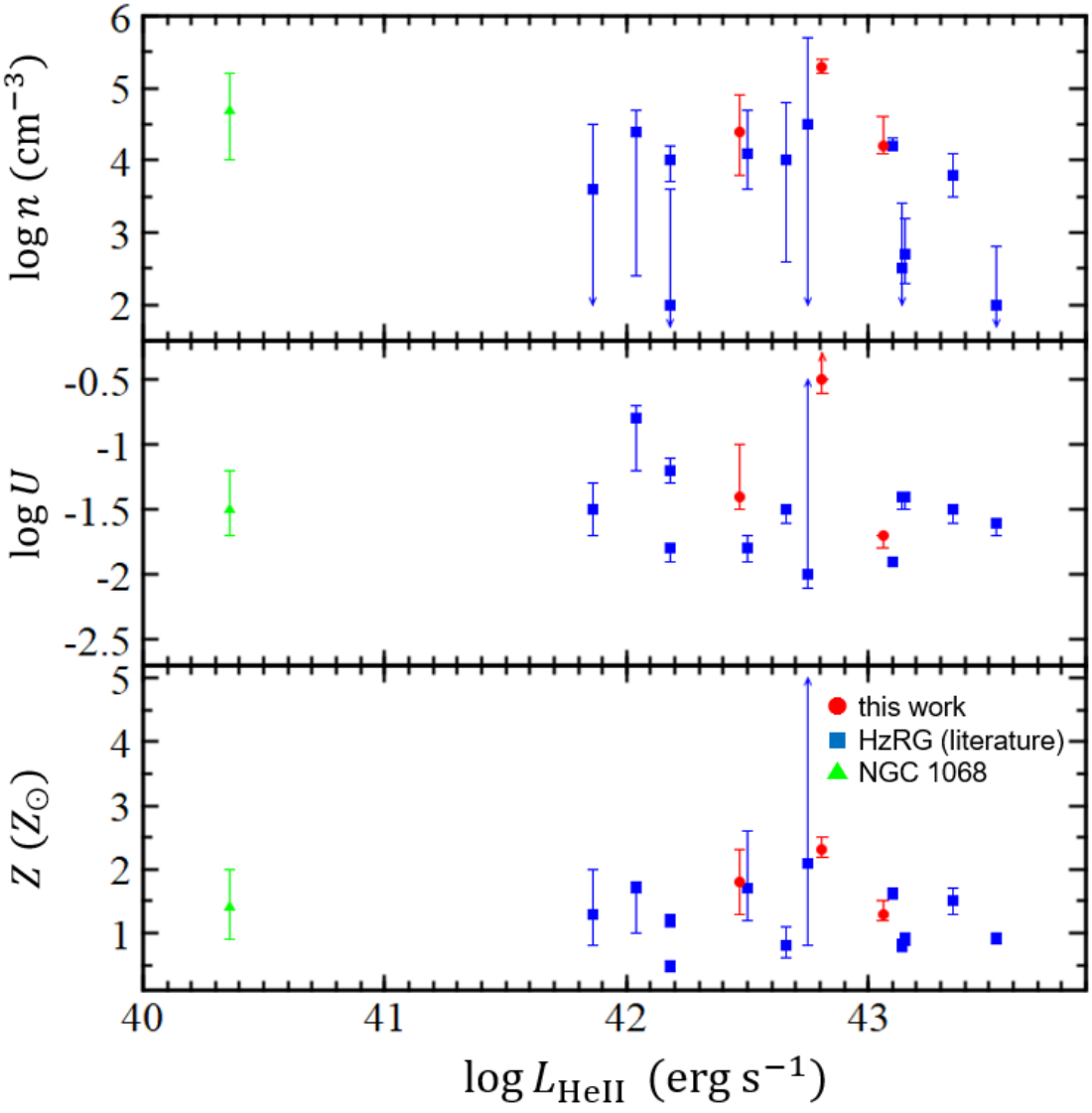

Fig. 3.11: Inferred parameters (gas density, ionization parameter, and gas metallicity, in the upper, middle, and lower panels, respectively) as a function of the He II luminosity. Red circles are our targets, while blue squares are HzRGs taken from the literature. Green triangle shows NGC 1068. Arrows denote the cases where the inferred error reaches the limit of calculations.

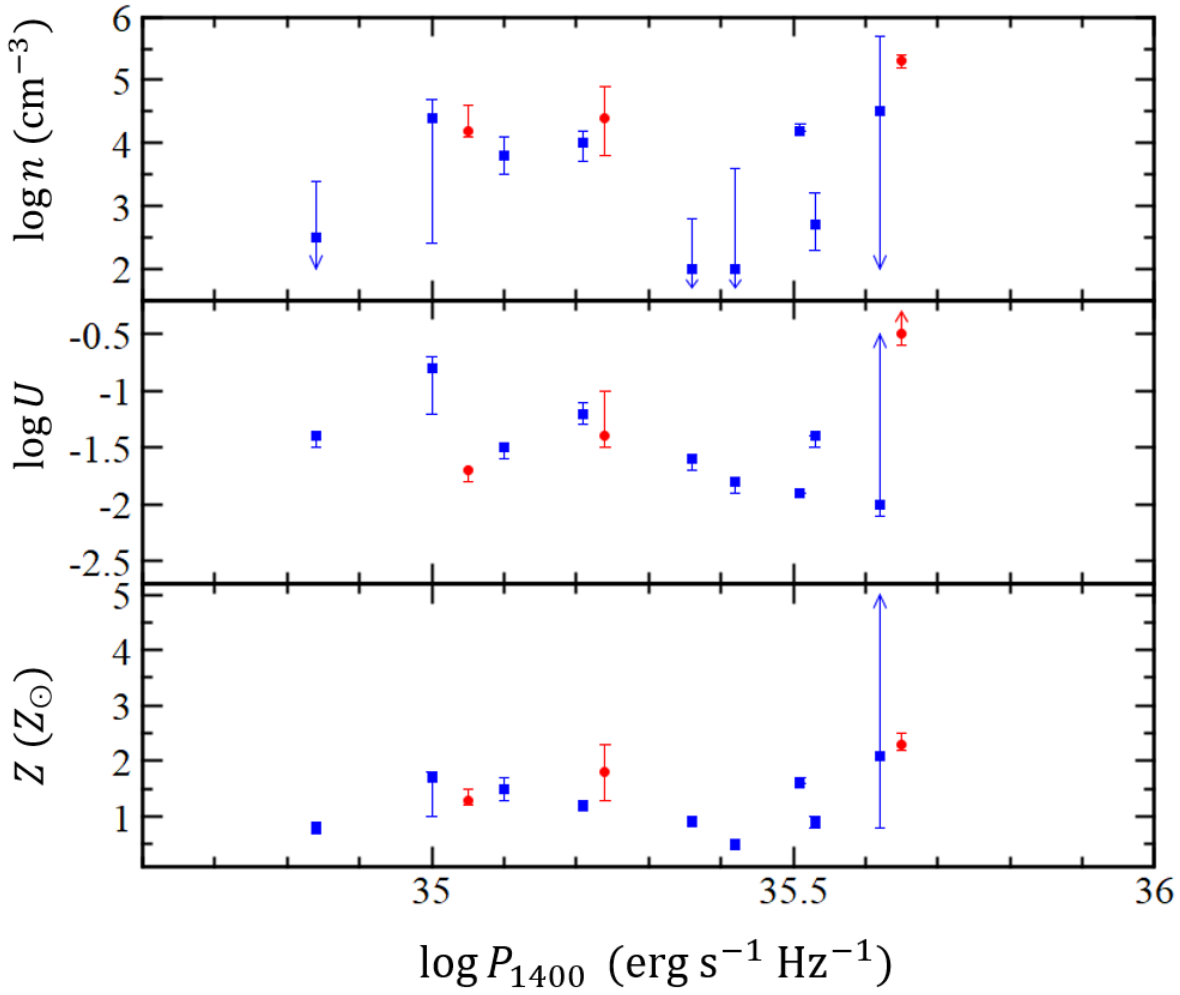

Fig. 3.12: Relation between the radio power at 1400 MHz (P_{1400}) and the derived NLR parameters, i.e., the gas density (upper), ionization parameter (middle), and metallicity (lower). Red circles denote our targets. Blue squares denote additional HzRG samples from the literature. Arrows denote the cases where the inferred error reaches the limit of calculations.

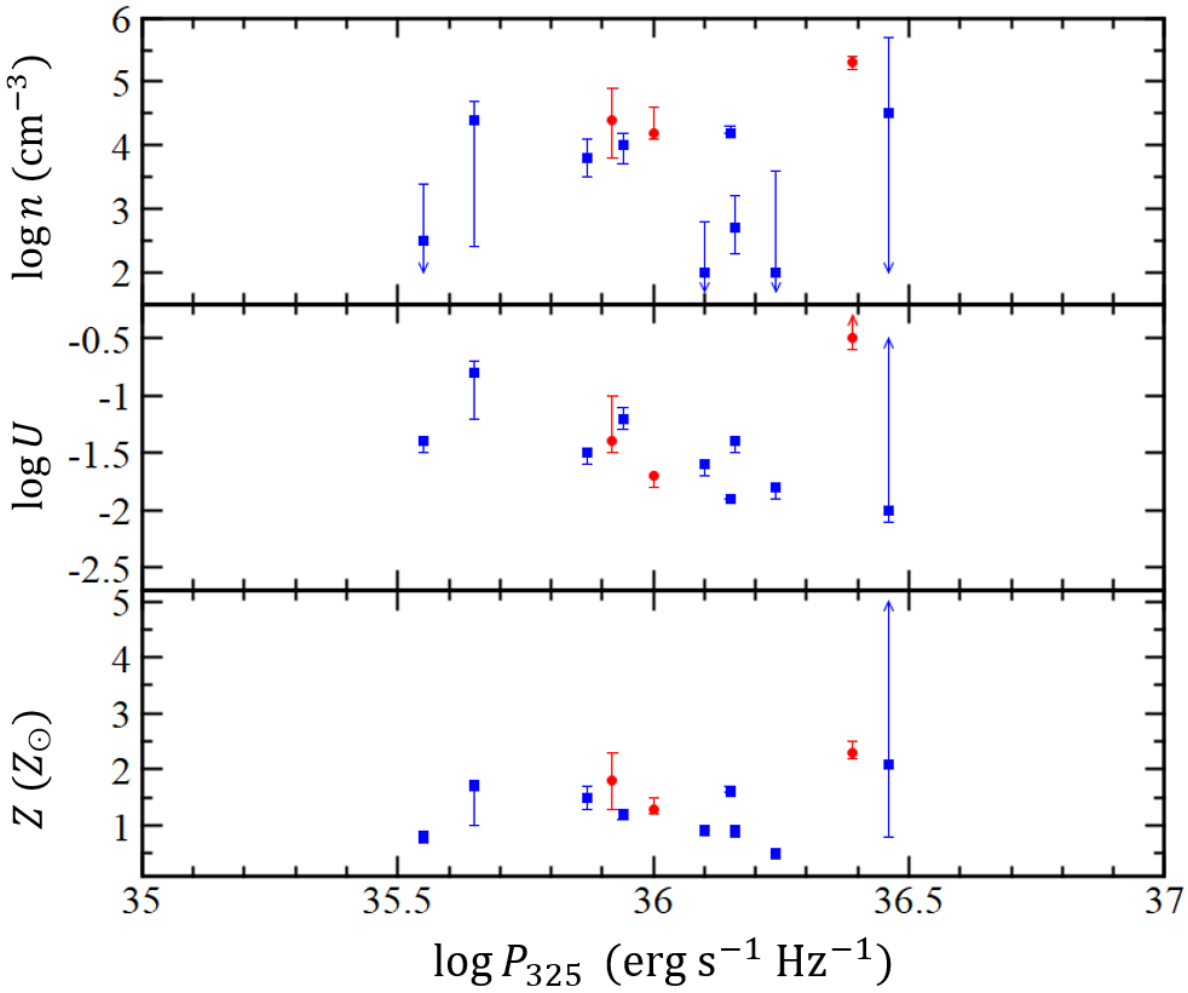

Fig. 3.13: Same as Figure 3.12 but for the radio power at 325 MHz ($P_{325\mathrm{MHz}}$).

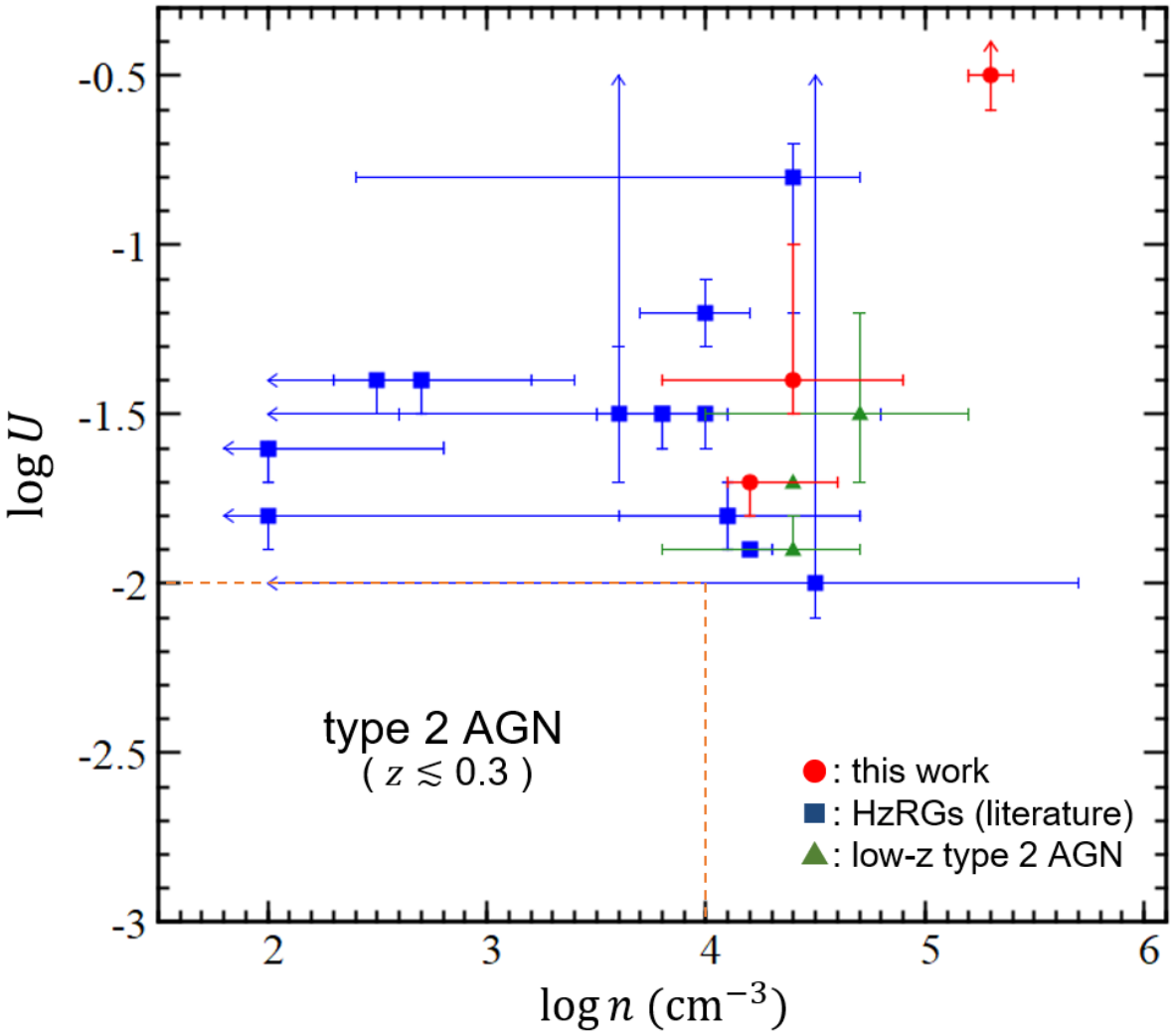

Fig. 3.14: Inferred gas densities and ionization parameters of HzRGs compared to the low-z type 2 AGN (Vaona et al., 2012). Red circles represent our targets, while blue squares are HzRGs taken from the literature. Green triangles denote low-z type 2 AGN with rest-UV data. Arrows denote the cases where the inferred error reaches the limit of calculations.

CHAPTER 4

GENERAL CONCLUSION

In this doctoral dissertation, we focused on the NLRs in AGNs to investigate physical and chemical properties of ISM in galaxies, and to distinguish the ionization mechanisms.

In Chapter 2, in order to investigate how the fast shock contributes to the NLR ionization, we have carried out near-infrared J-band spectroscopic observations of 26 nearby Seyfert galaxies. In our analysis, we use the [Fe II]/[P II] flux ratio as a powerful diagnostics of the fast shock in the NLR. Among the 26 observed Seyferts, the [P II] emission is significantly detected in 6 objects, while the [Fe II] emission is significantly detected in 19 objects. By adding the data from the literature, we gather the [Fe II]/[P II] flux ratio or its lower limit for 23 nearby AGNs. Based on this combined large sample of Seyfert galaxies, we obtain the following results and conclusions.

1. We find that more than half of our Seyfert sample show consistent [Fe II]/[P II] flux ratios to the prediction by the photoionization model. Three Seyfert galaxies, NGC 2782, NGC 5005, and Mrk 463, however, show very large [Fe II]/[P II] flux ratios ($\gtrsim 10$), suggesting a significant contribution of the fast shock in the NLR excitation.

2. The positive correlation between the [Fe II]/[P II] flux ratio and the [Fe II]/Paβ reported in the literature is confirmed in our large sample of Seyfert galaxies. This also supports the interpretation that the NLR in AGNs with a large [Fe II]/[P II] flux ratio is affected by fast shocks.

3. The positive correlation between the [Fe II]/[P II] flux ratio and the FWHM ratio of [Fe II] and [P II] is found in our sample. This is consistent with the interpretation that the observed [Fe II] flux in AGNs with a large [Fe II]/[P II] flux ratio is significantly attributed to shock-excited clouds.

4. The [Fe II]/[P II] flux ratio in our sample shows no clear correlation with the radio loudness or the strength of the starburst, suggesting that the radio jet and starburst are not the primary origins of the fast shocks in the NLR.

In Chapter 3, we focused on the high-sensitivity rest-UV spectra of 15 radio galaxies at redshift $\sim 2-3$ to measure the flux of several emission lines including relatively faint ones. We diagnose the physical and chemical properties of the ISM in NLR for each object through the comparison between the measured emission-line fluxes and detailed photoionization models. Main results of this work are as follows.

1. Most HzRGs show moderately high gas metallicity, that is close to or higher than the solar metallicities (i.e., $Z \gtrsim Z_{\odot}$). This result is consistent with some previous studies (e.g., Nagao et al., 2006b; Matsuoka et al., 2009), but obtained with less assumptions in the photoionization model with respect to those previous works. The obtained result strongly suggests that HzRGs at $z \sim 3$ are already matured chemically, even in the early Universe where the cosmic age was only ~ 2 Gyr.

2. The inferred physical parameters (gas density, ionization parameter, and gas metallicity) of NLRs in HzRGs show no correlation with the radio power. This suggests that the physical properties of NLRs in our sample are not significantly affected by the radio jet.

3. Compared to low-z type 2 AGNs, gas clouds in NLRs of HzRGs tend to show higher ionization parameter and gas density. This result implies that ISM properties of AGN host galaxies show the redshift evolution that is seen also in star-forming galaxies.

BIBLIOGRAPHY

Adhikari, T. P., Różańska, A., Czerny, B., Hryniewicz, K., & Ferland, G. J. 2016, ApJ, 831, 68

Akritas, M. G., & Bershady, M. A. 1996, ApJ, 470, 706

Alatalo, K., Lacy, M., Lanz, L., et al. 2015, ApJ, 798, 31

Allen, M. G., Groves, B. A., Dopita, M. A., Sutherland, R. S., & Kewley, L. J. 2008, ApJS, 178, 20

Alloin, D., Collin-Souffrin, S., Joly, M., & Vigroux, L. 1979, A&A, 78, 200

Antonucci, R. R. J., & Miller, J. S. 1985, ApJ, 297, 621

Appenzeller, I., Fricke, K., Fürtig, W., et al. 1998, The Messenger, 94, 1

Araki, N., Nagao, T., Matsuoka, K., et al. 2012, A&A, 543, A143

Bañados, E., Venemans, B. P., Mazzucchelli, C., et al. 2018, Nature, 553, 473

Baldwin, J. A., Phillips, M. M., & Terlevich, R. 1981, PASP, 93, 5

Begelman, M. C., McKee, C. F., & Shields, G. A. 1983, ApJ, 271, 70

Belfiore, F., Maiolino, R., & Bothwell, M. 2016, MNRAS, 455, 1218

Bennert, N., Jungwiert, B., Komossa, S., Haas, M., & Chini, R. 2006a, A&A, 459, 55

—. 2006b, A&A, 456, 953

Bicay, M. D., Kojoian, G., Seal, J., Dickinson, D. F., & Malkan, M. A. 1995, ApJS, 98, 369

Bicknell, G. V., Dopita, M. A., Tsvetanov, Z. I., & Sutherland, R. S. 1998, ApJ, 495, 680

Bicknell, G. V., Sutherland, R. S., van Breugel, W. J. M., et al. 2000, ApJ, 540, 678

Bieri, R., Dubois, Y., Silk, J., Mamon, G. A., & Gaibler, V. 2016, MNRAS, 455, 4166

Binette, L., Wilson, A. S., Raga, A., & Storchi-Bergmann, T. 1997, A&A, 327, 909

Binette, L., Wilson, A. S., & Storchi-Bergmann, T. 1996, A&A, 312, 365

Bing, L., Shi, Y., Chen, Y., et al. 2019, MNRAS, 482, 194

Blandford, R. D., & Payne, D. G. 1982, MNRAS, 199, 883

Blecha, L., Snyder, G. F., Satyapal, S., & Ellison, S. L. 2018, MNRAS, 478, 3056

Boller, T., Brandt, W. N., & Fink, H. 1996, A&A, 305, 53

Boselli, A., Cortese, L., Boquien, M., et al. 2014, A&A, 564, A67

Bouwens, R. J., Bradley, L., Zitrin, A., et al. 2014, ApJ, 795, 126

Bouwens, R. J., Illingworth, G. D., Oesch, P. A., et al. 2015, ApJ, 803, 34

Bower, R. G., Benson, A. J., Malbon, R., et al. 2006, MNRAS, 370, 645

Brinchmann, J., Charlot, S., White, S. D. M., et al. 2004, MNRAS, 351, 1151

Bryant, J. J., Johnston, H. M., Broderick, J. W., et al. 2009, MNRAS, 395, 1099

Cappi, M. 2006, Astronomische Nachrichten, 327, 1012

Cardelli, J. A., Clayton, G. C., & Mathis, J. S. 1989, ApJ, 345, 245

Cardelli, J. A., Savage, B. D., Bruhweiler, F. C., et al. 1991, ApJ, 377, L57

Carniani, S., Marconi, A., Maiolino, R., et al. 2015, A&A, 580, A102

Castro, A., Miyaji, T., Shirahata, M., et al. 2014, PASJ, 66, 110

Cicone, C., Maiolino, R., Sturm, E., et al. 2014, A&A, 562, A21

Coe, D., Zitrin, A., Carrasco, M., et al. 2013, ApJ, 762, 32

Condon, J. J., Cotton, W. D., Greisen, E. W., et al. 1998, AJ, 115, 1693

Crenshaw, D. M., Kraemer, S. B., & George, I. M. 2003, ARA&A, 41, 117

Cresci, G., Marconi, A., Zibetti, S., et al. 2015, A&A, 582, A63

Croton, D. J., Springel, V., White, S. D. M., et al. 2006, MNRAS, 365, 11

Curti, M., Cresci, G., Mannucci, F., et al. 2017, MNRAS, 465, 1384

Cutri, R. M., Skrutskie, M. F., van Dyk, S., et al. 2003, VizieR Online Data Catalog, 2246

Daddi, E., Dickinson, M., Morrison, G., et al. 2007, ApJ, 670, 156

Daddi, E., Dannerbauer, H., Stern, D., et al. 2009, ApJ, 694, 1517

Dasyra, K. M., Ho, L. C., Netzer, H., et al. 2011, ApJ, 740, 94

De Breuck, C., Hunstead, R. W., Sadler, E. M., Rocca-Volmerange, B., & Klamer, I. 2004, MNRAS, 347, 837

De Breuck, C., Klamer, I., Johnston, H., et al. 2006, MNRAS, 366, 58

De Breuck, C., Röttgering, H., Miley, G., van Breugel, W., & Best, P. 2000, A&A, 362, 519

De Robertis, M. M., & Osterbrock, D. E. 1984, ApJ, 286, 171

de Vaucouleurs, G., de Vaucouleurs, A., Corwin, Jr., H. G., et al. 1991, Third Reference Catalogue of Bright Galaxies. Volume I: Explanations and references. Volume II: Data for galaxies between 0^h and 12^h. Volume III: Data for galaxies between 12^h and 24^h.

Di Matteo, T., Springel, V., & Hernquist, L. 2005, Nature, 433, 604

Dopita, M. A., Kewley, L. J., Heisler, C. A., & Sutherland, R. S. 2000, ApJ, 542, 224

Dopita, M. A., & Sutherland, R. S. 1995, ApJ, 455, 468

—. 1996, ApJS, 102, 161

Dors, O. L., Cardaci, M. V., Hägele, G. F., & Krabbe, Â. C. 2014, MNRAS, 443, 1291

Dubois, Y., Peirani, S., Pichon, C., et al. 2016, MNRAS, 463, 3948

Dugan, Z., Bryan, S., Gaibler, V., Silk, J., & Haas, M. 2014, ApJ, 796, 113

Dunn, J. P., Bautista, M., Arav, N., et al. 2010, ApJ, 709, 611

Elbaz, D., Daddi, E., Le Borgne, D., et al. 2007, A&A, 468, 33

Ellis, R. S., McLure, R. J., Dunlop, J. S., et al. 2013, ApJ, 763, L7

Erb, D. K. 2008, ApJ, 674, 151

ESA, ed. 1997, ESA Special Publication, Vol. 1200, The HIPPARCOS and TYCHO catalogues. Astrometric and photometric star catalogues derived from the ESA HIPPARCOS Space Astrometry Mission

Evans, I., Koratkar, A., Allen, M., Dopita, M., & Tsvetanov, Z. 1999, ApJ, 521, 531

Fabian, A. C. 2012, ARA&A, 50, 455

Fardal, M. A., Katz, N., Weinberg, D. H., & Davé, R. 2007, MNRAS, 379, 985

Feltre, A., Charlot, S., & Gutkin, J. 2016, MNRAS, 456, 3354

Ferguson, J. W., Korista, K. T., Baldwin, J. A., & Ferland, G. J. 1997, ApJ, 487, 122

Ferland, G. J., & Netzer, H. 1983, ApJ, 264, 105

Ferland, G. J., Porter, R. L., van Hoof, P. A. M., et al. 2013, Rev. Mexicana Astron. Astrofis., 49, 137

Ferrarese, L., & Merritt, D. 2000, ApJ, 539, L9

Feruglio, C., Fiore, F., Carniani, S., et al. 2015, A&A, 583, A99

Fischer, T. C., Crenshaw, D. M., Kraemer, S. B., & Schmitt, H. R. 2013, ApJS, 209, 1

Flohic, H. M. L. G., Eracleous, M., Chartas, G., Shields, J. C., & Moran, E. C. 2006, ApJ, 647, 140

Förster Schreiber, N. M., Genzel, R., Bouché, N., et al. 2009, ApJ, 706, 1364

Fu, H., & Stockton, A. 2007, ApJ, 666, 794

Fullmer, L., & Londsdale, C. J. 1989, Cataloged galaxies and quasars observed in the IRAS survey

Gallimore, J. F., Axon, D. J., O'Dea, C. P., Baum, S. A., & Pedlar, A. 2006, AJ, 132, 546

García-Burillo, S., Combes, F., Usero, A., et al. 2014, A&A, 567, A125

Gibson, R. R., Jiang, L., Brandt, W. N., et al. 2009, ApJ, 692, 758

Gofford, J., Reeves, J. N., Tombesi, F., et al. 2013, MNRAS, 430, 60

Goodrich, R. W., Cohen, M. H., & Putney, A. 1995, PASP, 107, 179

Greene, J. E., & Ho, L. C. 2005, ApJ, 627, 721

Gregory, P. C., Vavasour, J. D., Scott, W. K., & Condon, J. J. 1994, ApJS, 90, 173

Grevesse, N., Asplund, M., Sauval, A. J., & Scott, P. 2010, Ap&SS, 328, 179

Grevesse, N., Blackwell, D. E., & Petford, A. D. 1989, A&A, 208, 157

Grevesse, N., Noels, A., & Sauval, A. J. 1993, A&A, 271, 587

Groves, B. A., Dopita, M. A., & Sutherland, R. S. 2004, ApJS, 153, 75

Groves, B. A., Heckman, T. M., & Kauffmann, G. 2006, MNRAS, 371, 1559

Gültekin, K., Richstone, D. O., Gebhardt, K., et al. 2009, ApJ, 698, 198

Hamann, F., & Ferland, G. 1993, ApJ, 418, 11

—. 1999, ARA&A, 37, 487

Hardcastle, M. J., Worrall, D. M., Kraft, R. P., et al. 2003, ApJ, 593, 169

Harrison, C. M. 2017, Nature Astronomy, 1, 0165

Harrison, C. M., Costa, T., Tadhunter, C. N., et al. 2018, Nature Astronomy, 2, 198

Hashimoto, T., Nagao, T., Yanagisawa, K., Matsuoka, K., & Araki, N. 2011, PASJ, 63, L7

Heckman, T. M. 1980, A&A, 87, 152

Heckman, T. M., Armus, L., & Miley, G. K. 1990, ApJS, 74, 833

Heckman, T. M., & Best, P. N. 2014, ARA&A, 52, 589

Hickox, R. C., & Alexander, D. M. 2018, ARA&A, 56, 625

Ho, I.-T., Kewley, L. J., Dopita, M. A., et al. 2014, MNRAS, 444, 3894

Ho, I.-T., Medling, A. M., Bland-Hawthorn, J., et al. 2016, MNRAS, 457, 1257

Ho, L. C. 2008, ARA&A, 46, 475

Ho, L. C., Filippenko, A. V., & Sargent, W. L. W. 1996, ApJ, 462, 183

—. 1997a, ApJS, 112, 315

—. 1997b, ApJ, 487, 568

Hopkins, A. M., & Beacom, J. F. 2006, ApJ, 651, 142

Hopkins, P. F., Hernquist, L., Cox, T. J., & Kereš, D. 2008, ApJS, 175, 356

Humphrey, A., Villar-Martín, M., Vernet, J., et al. 2008, MNRAS, 383, 11

Imanishi, M., & Dudley, C. C. 2000, ApJ, 545, 701

Imanishi, M., & Wada, K. 2004, ApJ, 617, 214

Ishibashi, W., & Fabian, A. C. 2016, MNRAS, 463, 1291

Ishigaki, M., Kawamata, R., Ouchi, M., et al. 2018, ApJ, 854, 73

Iwamuro, F., Motohara, K., Maihara, T., et al. 2003, ApJ, 598, 178

Izotov, Y. I., Stasińska, G., Meynet, G., Guseva, N. G., & Thuan, T. X. 2006, A&A, 448, 955

Jackson, N., & Beswick, R. J. 2007, MNRAS, 376, 719

Jiang, L., Fan, X., Vestergaard, M., et al. 2007, AJ, 134, 1150

Jones, A., Noll, S., Kausch, W., Szyszka, C., & Kimeswenger, S. 2013, A&A, 560, A91

Juarez, Y., Maiolino, R., Mujica, R., et al. 2009, A&A, 494, L25

Karim, A., Schinnerer, E., Martínez-Sansigre, A., et al. 2011, ApJ, 730, 61

Kellermann, K. I., Sramek, R., Schmidt, M., Shaffer, D. B., & Green, R. 1989, AJ, 98, 1195

Kennicutt, Jr., R. C. 1998, ARA&A, 36, 189

Kewley, L. J., & Dopita, M. A. 2002, ApJS, 142, 35

Kewley, L. J., Dopita, M. A., Leitherer, C., et al. 2013, ApJ, 774, 100

Kewley, L. J., & Ellison, S. L. 2008, ApJ, 681, 1183

Kewley, L. J., Groves, B., Kauffmann, G., & Heckman, T. 2006, MNRAS, 372, 961

King, A., & Pounds, K. 2015, ARA&A, 53, 115

Knop, R. A., Armus, L., Larkin, J. E., et al. 1996, AJ, 112, 81

Komossa, S., & Schulz, H. 1997, A&A, 323, 31

Konigl, A., & Kartje, J. F. 1994, ApJ, 434, 446

Koo, B.-C., & Lee, Y.-H. 2015, Publication of Korean Astronomical Society, 30, 145

Koo, B.-C., Lee, Y.-H., Moon, D.-S., Yoon, S.-C., & Raymond, J. C. 2013, Science, 342, 1346

Koratkar, A., & Blaes, O. 1999, PASP, 111, 1

Kormendy, J., & Ho, L. C. 2013, ARA&A, 51, 511

Kormendy, J., & Richstone, D. 1995, ARA&A, 33, 581

Krajnović, D., Sharp, R., & Thatte, N. 2007, MNRAS, 374, 385

Krolik, J. H., & Kriss, G. A. 2001, ApJ, 561, 684

Kurk, J. D., Walter, F., Fan, X., et al. 2007, ApJ, 669, 32

Larkin, J. E., Armus, L., Knop, R. A., Soifer, B. T., & Matthews, K. 1998, ApJS, 114, 59

Laurent-Muehleisen, S. A., Kollgaard, R. I., Ryan, P. J., et al. 1997, A&AS, 122, 235

Leslie, S. K., Kewley, L. J., Sanders, D. B., & Lee, N. 2016, MNRAS, 455, L82

Lilly, S. J., Carollo, C. M., Pipino, A., Renzini, A., & Peng, Y. 2013, ApJ, 772, 119

Lu, Y., Blanc, G. A., & Benson, A. 2015, ApJ, 808, 129

Lynden-Bell, D. 1969, Nature, 223, 690

Madau, P., & Dickinson, M. 2014, ARA&A, 52, 415

Madau, P., Pozzetti, L., & Dickinson, M. 1998, ApJ, 498, 106

Magnelli, B., Elbaz, D., Chary, R. R., et al. 2009, A&A, 496, 57

—. 2011, A&A, 528, A35

Magorrian, J., Tremaine, S., Richstone, D., et al. 1998, AJ, 115, 2285

Mahoro, A., Pović, M., & Nkundabakura, P. 2017, MNRAS, 471, 3226

Maier, C., Lilly, S. J., Ziegler, B. L., et al. 2014, ApJ, 792, 3

Maiolino, R., Nagao, T., Grazian, A., et al. 2008, A&A, 488, 463

Maiolino, R., Gallerani, S., Neri, R., et al. 2012, MNRAS, 425, L66

Mannucci, F., Cresci, G., Maiolino, R., et al. 2009, MNRAS, 398, 1915

Maoz, D., Koratkar, A., Shields, J. C., et al. 1998, AJ, 116, 55

Marconi, A., & Hunt, L. K. 2003, ApJ, 589, L21

Marconi, A., Moorwood, A. F. M., Salvati, M., & Oliva, E. 1994, A&A, 291, 18

Mathews, W. G., & Ferland, G. J. 1987, ApJ, 323, 456

Matsuoka, K., Nagao, T., Maiolino, R., et al. 2017, A&A, 608, A90

Matsuoka, K., Nagao, T., Maiolino, R., Marconi, A., & Taniguchi, Y. 2009, A&A, 503, 721

—. 2011a, A&A, 532, L10

Matsuoka, K., Nagao, T., Marconi, A., et al. 2018a, A&A, 616, L4

Matsuoka, K., Nagao, T., Marconi, A., Maiolino, R., & Taniguchi, Y. 2011b, A&A, 527, A100

Matsuoka, Y., Iwasawa, K., Onoue, M., et al. 2018b, ApJS, 237, 5

McAlary, C. W., McLaren, R. A., McGonegal, R. J., & Maza, J. 1983, ApJS, 52, 341

McConnell, N. J., & Ma, C.-P. 2013, ApJ, 764, 184

McLure, R. J., Dunlop, J. S., Bowler, R. A. A., et al. 2013, MNRAS, 432, 2696

Miller, J. S., Goodrich, R. W., & Mathews, W. G. 1991, ApJ, 378, 47

Miller, P., Rawlings, S., & Saunders, R. 1993, MNRAS, 263, 425

Moe, M., Arav, N., Bautista, M. A., & Korista, K. T. 2009, ApJ, 706, 525

Molina, M., Eracleous, M., Barth, A. J., et al. 2018, ApJ, 864, 90

Morais, S. G., Humphrey, A., Villar-Martín, M., et al. 2017, MNRAS, 465, 2698

Mouri, H., Kawara, K., & Taniguchi, Y. 2000, ApJ, 528, 186

Mullaney, J. R., Alexander, D. M., Fine, S., et al. 2013, MNRAS, 433, 622

Murray, N., Chiang, J., Grossman, S. A., & Voit, G. M. 1995, ApJ, 451, 498

Naab, T., & Ostriker, J. P. 2017, ARA&A, 55, 59

Nagao, T., Maiolino, R., De Breuck, C., et al. 2012, A&A, 542, L34

Nagao, T., Maiolino, R., & Marconi, A. 2006a, A&A, 459, 85

—. 2006b, A&A, 447, 863

Nagao, T., Marconi, A., & Maiolino, R. 2006c, A&A, 447, 157

Nagao, T., Murayama, T., Shioya, Y., & Taniguchi, Y. 2002, ApJ, 575, 721

—. 2003, AJ, 125, 1729

Nagao, T., Murayama, T., & Taniguchi, Y. 2001a, PASJ, 53, 629

—. 2001b, ApJ, 546, 744

Nagao, T., Taniguchi, Y., & Murayama, T. 2000, AJ, 119, 2605

Nagar, N. M., Falcke, H., & Wilson, A. S. 2005, A&A, 435, 521

Nagar, N. M., Wilson, A. S., & Falcke, H. 2001, ApJ, 559, L87

Nakajima, K., Ellis, R. S., Iwata, I., et al. 2016, ApJ, 831, L9

Nakajima, K., Fletcher, T., Ellis, R. S., Robertson, B. E., & Iwata, I. 2018, MNRAS, 477, 2098

Nakajima, K., & Ouchi, M. 2014, MNRAS, 442, 900

Netzer, H. 1990, in Active Galactic Nuclei, ed. R. D. Blandford, H. Netzer, L. Woltjer, T. J.-L. Courvoisier, & M. Mayor, 57–160

Newman, S. F., Buschkamp, P., Genzel, R., et al. 2014, ApJ, 781, 21

Noeske, K. G., Weiner, B. J., Faber, S. M., et al. 2007, ApJ, 660, L43

Noll, S., Kausch, W., Barden, M., et al. 2012, A&A, 543, A92

Nomura, M., Ohsuga, K., Takahashi, H. R., Wada, K., & Yoshida, T. 2016, PASJ, 68, 16

Oesch, P. A., Bouwens, R. J., Illingworth, G. D., Labbé, I., & Stefanon, M. 2018, ApJ, 855, 105

Oesch, P. A., Bouwens, R. J., Illingworth, G. D., et al. 2013, ApJ, 773, 75

—. 2014, ApJ, 786, 108

Oesch, P. A., Brammer, G., van Dokkum, P. G., et al. 2016, ApJ, 819, 129

Oi, N., Imanishi, M., & Imase, K. 2010, PASJ, 62, 1509

Oke, J. B., & Gunn, J. E. 1982, PASP, 94, 586

Oke, J. B., Cohen, J. G., Carr, M., et al. 1995, PASP, 107, 375

Oliva, E., Marconi, A., Maiolino, R., et al. 2001, A&A, 369, L5

Osterbrock, D. E., & Ferland, G. J. 2006, Astrophysics of gaseous nebulae and active galactic nuclei

Osterbrock, D. E., & Pogge, R. W. 1985, ApJ, 297, 166

Padovani, P., Alexander, D. M., Assef, R. J., et al. 2017, A&A Rev., 25, 2

Pagel, B. E. J., Edmunds, M. G., Blackwell, D. E., Chun, M. S., & Smith, G. 1979, MNRAS, 189, 95

Pannella, M., Carilli, C. L., Daddi, E., et al. 2009, ApJ, 698, L116

Pereira-Santaella, M., Diamond-Stanic, A. M., Alonso-Herrero, A., & Rieke, G. H. 2010, ApJ, 725, 2270

Petric, A. O., Armus, L., Howell, J., et al. 2011, ApJ, 730, 28

Petrosian, A., McLean, B., Allen, R. J., & MacKenty, J. W. 2007, ApJS, 170, 33

Proga, D., Ostriker, J. P., & Kurosawa, R. 2008, ApJ, 676, 101

Ramos Almeida, C., Pérez García, A. M., & Acosta-Pulido, J. A. 2009, ApJ, 694, 1379

Ramos Almeida, C., Pérez García, A. M., Acosta-Pulido, J. A., et al. 2006, ApJ, 645, 148

Reddy, N. A., & Steidel, C. C. 2009, ApJ, 692, 778

Rees, M. J. 1984, ARA&A, 22, 471

Rich, J. A., Dopita, M. A., Kewley, L. J., & Rupke, D. S. N. 2010, ApJ, 721, 505

Richards, G. T., Lacy, M., Storrie-Lombardi, L. J., et al. 2006, ApJS, 166, 470

Riffel, R., Rodríguez-Ardila, A., & Pastoriza, M. G. 2006, A&A, 457, 61

Riffel, R. A., & Storchi-Bergmann, T. 2011, MNRAS, 417, 2752

Riffel, R. A., Storchi-Bergmann, T., & Nagar, N. M. 2010, MNRAS, 404, 166

Riffel, R. A., Storchi-Bergmann, T., & Riffel, R. 2015, MNRAS, 451, 3587

Riffel, R. A., Storchi-Bergmann, T., & Winge, C. 2013, MNRAS, 430, 2249

Riffel, R. A., Vale, T. B., Storchi-Bergmann, T., & McGregor, P. J. 2014, MNRAS, 442, 656

Risaliti, G., Maiolino, R., & Salvati, M. 1999, ApJ, 522, 157

Robertson, B. E., Ellis, R. S., Furlanetto, S. R., & Dunlop, J. S. 2015, ApJ, 802, L19

Robinson, A., Binette, L., Fosbury, R. A. E., & Tadhunter, C. N. 1987, MNRAS, 227, 97

Rodríguez-Ardila, A., & Viegas, S. M. 2003, MNRAS, 340, L33

Rose, M., Elvis, M., & Tadhunter, C. N. 2015, MNRAS, 448, 2900

Rottgering, H. J. A., Miley, G. K., Chambers, K. C., & Macchetto, F. 1995, A&AS, 114, 51

Rupke, D. S. N., & Veilleux, S. 2011, ApJ, 729, L27

Salpeter, E. E. 1964, ApJ, 140, 796

Sanders, D. B., & Mirabel, I. F. 1996, ARA&A, 34, 749

Sanders, D. B., Soifer, B. T., Elias, J. H., et al. 1988, ApJ, 325, 74

Sanders, R. L., Shapley, A. E., Kriek, M., et al. 2016, ApJ, 816, 23

Schiminovich, D., Ilbert, O., Arnouts, S., et al. 2005, ApJ, 619, L47

Schlegel, D. J., Finkbeiner, D. P., & Davis, M. 1998, ApJ, 500, 525

Schlesinger, K., Pogge, R. W., Martini, P., Shields, J. C., & Fields, D. 2009, ApJ, 699, 857

Schmidt, M. 1963, Nature, 197, 1040

Schönell, A. J., Riffel, R. A., Storchi-Bergmann, T., & Winge, C. 2014, MNRAS, 445, 414

Schweizer, F., & Seitzer, P. 2007, AJ, 133, 2132

Seyfert, C. K. 1943, ApJ, 97, 28

Shangguan, J., Ho, L. C., & Xie, Y. 2018, ApJ, 854, 158

Shankar, F., Weinberg, D. H., & Miralda-Escudé, J. 2009, ApJ, 690, 20

Shih, H.-Y., Stockton, A., & Kewley, L. 2013, ApJ, 772, 138

Silk, J., & Nusser, A. 2010, ApJ, 725, 556

Silk, J., & Rees, M. J. 1998, A&A, 331, L1

Silva, M., Humphrey, A., Lagos, P., et al. 2018, MNRAS, 474, 3649

Simpson, C., Eisenhardt, P., Armus, L., et al. 1999, ApJ, 525, 659

Singh, V., Ishwara-Chandra, C. H., Wadadekar, Y., Beelen, A., & Kharb, P. 2015, MNRAS, 446, 599

Skrutskie, M. F., Cutri, R. M., Stiening, R., et al. 2006, AJ, 131, 1163

Snijders, M. A. J., Netzer, H., & Boksenberg, A. 1986, MNRAS, 222, 549

Solórzano-Iñarrea, C., Best, P. N., Röttgering, H. J. A., & Cimatti, A. 2004, MNRAS, 351, 997

Somerville, R. S., & Davé, R. 2015, ARA&A, 53, 51

Spacek, A., Scannapieco, E., Cohen, S., Joshi, B., & Mauskopf, P. 2017, ApJ, 834, 102

Sparke, L. S., & Gallagher, III, J. S. 2006, Galaxies in the Universe - 2nd Edition, 406, doi:10.2277/0521855934

Speagle, J. S., Steinhardt, C. L., Capak, P. L., & Silverman, J. D. 2014, ApJS, 214, 15

Sramek, R. 1975, AJ, 80, 771

Steinhardt, C. L., Speagle, J. S., Capak, P., et al. 2014, ApJ, 791, L25

Storchi-Bergmann, T., Lopes, R. D. S., McGregor, P. J., et al. 2010, MNRAS, 402, 819

Storchi-Bergmann, T., McGregor, P. J., Riffel, R. A., et al. 2009, MNRAS, 394, 1148

Tadhunter, C. 2016, A&A Rev., 24, 10

Taylor, G. B., Gugliucci, N. E., Fabian, A. C., et al. 2006, MNRAS, 368, 1500

Terao, K., Nagao, T., Hashimoto, T., et al. 2016, ApJ, 833, 190

Thomas, A. D., Groves, B. A., Sutherland, R. S., et al. 2016, ApJ, 833, 266

Tody, D. 1986, in Society of Photo-Optical Instrumentation Engineers (SPIE) Conference Series, Vol. 627, Instrumentation in astronomy VI, ed. D. L. Crawford, 733

Tody, D. 1993, in Astronomical Society of the Pacific Conference Series, Vol. 52, Astronomical Data Analysis Software and Systems II, ed. R. J. Hanisch, R. J. V. Brissenden, & J. Barnes, 173

Tombesi, F., Cappi, M., Reeves, J. N., et al. 2010, A&A, 521, A57

Tomczak, A. R., Quadri, R. F., Tran, K.-V. H., et al. 2016, ApJ, 817, 118

Tremonti, C. A., Heckman, T. M., Kauffmann, G., et al. 2004, ApJ, 613, 898

Troncoso, P., Maiolino, R., Sommariva, V., et al. 2014, A&A, 563, A58

Ulvestad, J. S., & Wilson, A. S. 1984, ApJ, 285, 439

Ulvestad, J. S., Wrobel, J. M., Roy, A. L., et al. 1999, ApJ, 517, L81

Urry, C. M., & Padovani, P. 1995, PASP, 107, 803

van Dokkum, P. G. 2001, PASP, 113, 1420

Vangioni, E., Dvorkin, I., Olive, K. A., et al. 2018, MNRAS, 477, 56

Vaona, L., Ciroi, S., Di Mille, F., et al. 2012, MNRAS, 427, 1266

Veilleux, S. 1991, ApJ, 369, 331

Veilleux, S., Bolatto, A., Tombesi, F., et al. 2017, ApJ, 843, 18

Veilleux, S., Cecil, G., & Bland-Hawthorn, J. 2005, ARA&A, 43, 769

Vernet, J., Fosbury, R. A. E., Villar-Martín, M., et al. 2001, A&A, 366, 7

Véron-Cetty, M.-P., & Véron, P. 2010, A&A, 518, A10

Villar-Martín, M., Arribas, S., Emonts, B., et al. 2016, MNRAS, 460, 130

Villar-Martin, M., Binette, L., & Fosbury, R. A. E. 1996, A&A, 312, 751

Villar-Martín, M., Fosbury, R. A. E., Binette, L., Tadhunter, C. N., & Rocca-Volmerange, B. 1999, A&A, 351, 47

Villar-Martín, M., Humphrey, A., De Breuck, C., et al. 2007, MNRAS, 375, 1299

Wagner, A. Y., Bicknell, G. V., & Umemura, M. 2012, ApJ, 757, 136

Wagner, A. Y., Umemura, M., & Bicknell, G. V. 2013, ApJ, 763, L18

Watabe, Y., Kawakatu, N., & Imanishi, M. 2008, ApJ, 677, 895

Weaver, K. A., Meléndez, M., Mushotzky, R. F., et al. 2010, ApJ, 716, 1151

Weymann, R. J., Morris, S. L., Foltz, C. B., & Hewett, P. C. 1991, ApJ, 373, 23

Whittle, M. 1992, ApJS, 79, 49

Wilson, A. S., & Raymond, J. C. 1999, ApJ, 513, L115

Wilson, A. S., & Willis, A. G. 1980, ApJ, 240, 429

Woo, J.-H., Schulze, A., Park, D., et al. 2013, ApJ, 772, 49

Wu, Y.-Z., Zhao, Y.-H., & Meng, X.-M. 2011, ApJS, 195, 17

Xu, F., Bian, F., Shen, Y., et al. 2018, MNRAS, 480, 345

Yabe, K., Ohta, K., Iwamuro, F., et al. 2012, PASJ, 64, 60

Yanagisawa, K., Shimizu, Y., Okita, K., et al. 2006, in Society of Photo-Optical Instrumentation Engineers (SPIE) Conference Series, Vol. 6269, Society of Photo-Optical Instrumentation Engineers (SPIE) Conference Series, 3

Yanagisawa, K., Okita, K., Shimizu, Y., et al. 2008, in Society of Photo-Optical Instrumentation Engineers (SPIE) Conference Series, Vol. 7014, Society of Photo-Optical Instrumentation Engineers (SPIE) Conference Series, 37

Yuan, T.-T., Kewley, L. J., & Richard, J. 2013, ApJ, 763, 9

Zheng, W. 1988, Astrophysical Letters and Communications, 27, 275

Zheng, W., Kriss, G. A., Telfer, R. C., Grimes, J. P., & Davidsen, A. F. 1997, ApJ, 475, 469

Zheng, W., Postman, M., Zitrin, A., et al. 2012, Nature, 489, 406

Zubovas, K., & King, A. 2012, ApJ, 745, L34

Zwicky, F., & Kowal, C. T. 1968, "Catalogue of Galaxies and of Clusters of Galaxies", Volume VI

ACKNOWLEDGMENTS

I am really grateful to my supervisor, Professor Tohru Nagao, for continuous supports, a lot of useful advice, and kind encouragements. Dr. Kyoko Onishi instructed me to write this thesis many times. Thanks to their supports, I could accomplish this doctoral dissertation. I would like to appreciate them deeply. I would like to thank Professor Hisamitu Awaki and Dr. Masaru Kajisawa for taking on the referee and useful comments. This doctoral dissertation improved by their kindly supports. I would like to thank Professor Yoshiaki Taniguchi, Dr. Yoshiki Matsuoka, Dr. Kenshi Yanagisawa, Dr. Tetsuya Hashimoto, Dr. Kenta Matsuoka, Dr. Yoshiki Toba, Dr. Hiroyuki Ikeda, and Dr. Takuji Yamashita. They supported and helped my research and discussion and advice. I also thank Dr. Kazuyuki Ogura, Dr. Shuhei Koyama, Mana Niida, Madoka Oshiro, Kota Kawasaki, Kodai Nobuhara, Mizuki Kuno, Takuya Bando, Yusuke Nitta, Akatoki Noboriguchi, Yuki Sato, Kazuharu Himoto, Toru Ishino, Kohei Iwashita, Nanako Kato, Yuya Saeda, Yuka Nagashima, Ayumi Ishida, Ryo Ihara, Kazuma Joh, Nozomu Tamada, Suzuka Nakano, and Naoki Yonekura. Finally, I am grateful to my parents and family for understanding and support to get a Ph.D program.

We would like to thank Dr. Gary J. Ferland for providing the photoionization code Cloudy to the public. Photoionization model calculations were in part carried out on the Multi-wavelength Data Analysis System operated by the Astronomy Data Center (ADC), National Astronomical Observatory of Japan.

This thesis is based on observations with the 188 cm telescope at the Okayama Astrophysical Observatory (OAO) operated by National Astronomical Observatory of Japan (NAOJ). We thank K. Matsubayashi, T. Hori, N. Araki, and the OAO staffs for their support during the observations.

This research has made use of the NASA/IPAC Extragalactic Database (NED), which is operated by the Jet Propulsion Laboratory, California Institute of Technology, under contract with the National Aeronautics and Space Administration. This publication makes use of data products from the Two Micron All Sky Survey, which is a joint project of the University of Massachusetts and the Infrared Processing and Analysis Center/California Institute of Technology, funded by the National Aeronautics and Space Administration and the National Science Foundation. IRAF is distributed by the National Optical Astronomy Observatory, which is operated by the Association of Universities for Research in Astronomy (AURA) under a cooperative agreement with the National Science Foundation.